Controlled stress – thermally inducing strain in graphene

Submitted by Gregor Arran McQuade to the University of Exeter as a thesis for the degree of Doctor of Philosophy in Physics

September 2019

I certify that all material in this thesis which is not my own work has been identified and that no material has previously been submitted and approved for the award of a degree by this or any other University.

Gregor Arran McQuade

September 2019

Abstract

This thesis investigates the effects of thermal strain on single to few layer graphene on silicon substrates below room temperature. Three graphene device designs and two directions of temperature change were explored to determine the differences these cause in graphene undergoing strain. Biaxial strain dependences with temperature were found in all graphene thicknesses and designs, with a magnitude consistent with the difference in thermal expansion coefficient (TEC) predicted between graphene and the substrate. The samples did not show significant variance in strain or dopant concentration dependences that correlated with the manufacturing or measurement methods. The thermal expansion coefficients of single to three layer graphene was measured in the range from 6 K to 296 K and were found to be in good agreement with the predicted theory of single layer graphene. A preliminary study into the effects of ultra-flat, h-BN substrates to observe differences in the graphene strain and TEC was undertaken. It was inconclusive at this stage if any significant differences are caused.

Acknowledgements

There are many who I wish to express my gratitude towards for their role in making my PhD journey possible.

Primarily, I wish to thank my supervisors, Dr. Annette Plaut and Dr. Alan Usher. I appreciate the efforts of Annette to lend expertise, observations, and support to help me solve any problems I could not handle alone. Your keen eye for detail has been invaluable throughout the course of my studies. Alan was always willing to make time to offer insight and offer a wider context to the work I was doing. I would also like to give thanks to our collaborator, Dr. Jens Martin, whose regular meetings gave a valuable, external perspective and also helped to inform us on specialised sample manufacturing techniques.

I have greatly appreciated the friendship and assistance from the other members of the quantum systems and nanostructures (QSN) group within the department. In particular Janire Ulibarri, Dr. Christopher Downs, Thomas Collier, Dr. Freddie Withers, Dr. Adolfo De Sanctis, and Darren Nutting. Chris passed down his expertise, the similarities between our research areas feeling like a continuation of ongoing study. Fred contributed much technical expertise on microscopic sample manufacture and often helped make complex tasks simple. Finally a thanks to Tom for an excellent chilli chutney.

I would like to give thanks to the technical staff of the department. Mark Heath provided excellent training in electron beam lithography, etching techniques, and scanning electron analysis. Paul Wilkins helped engineer the experimental

mounting stage, built once in cardboard and then metal, to a high quality. Adam Woodgate assisted greatly in maintaining the steady flow of cryogenic helium.

I would like to thank those closest to me for their patience and understanding when getting caught up in the project. My father, Gordon and mother, Anne were always ready to assist, and were always supportive throughout my academic career. Finally, my thanks to my partner Jess, for your continuous support throughout our time here.

Contents

List of figures

1 Introduction

1.1 Introduction

Graphene is a two dimensional (2D) layer of carbon atoms with a honeycomb structure. It has been of theoretical interest since the 1940s and of experimental interest since it was successfully isolated in 2007.[1,2] Since this proof of successful fabrication, a great amount of interest has been ignited in graphene and other 2D materials due to the unusual electronic properties predicted at this dimensionality.[3-6] The 2D materials also allowed for the direct probing of these phenomena, unlike previous studies into 2D systems, which revolved around interfaces between two three dimensional (3D) systems.[7]

In addition to the electronic properties, graphene also has useful structural properties. The covalent bonding between the carbon atoms in graphene results in graphene being sturdy in its 2D plane and graphene has shown the ability to maintain its structure under large elastic deformations.[8] This combination of interesting electronic properties and elasticity has opened the possibility of influencing the electronics of graphene by inducing strains. This would enable the use of strain to create “valleytronic” devices, which affect electron behaviour depending on which energy “valley” they occupy in momentum space.[9-11] Therefore, there is a desire for methods of easily controlling strain in microscopic graphene systems to create the next generation of complex electronic devices.

Strains can be induced in graphene in several ways, such as bending the material it is placed on or forming pressurised bubbles under it.[12-15] A strain in graphene

will also be induced through the difference in thermal expansion between the graphene and a material it is in contact with, with the same principle as a bimetallic strip. This would cause a strain in graphene device whenever its temperature is changed from that which it was manufactured at. Since there are many experiments on graphene and 2D materials that use low temperatures for noise reduction, the categorisation of these strains is useful for designing electronic devices in which strain induced effects would be undesirable.

Given that thermal strains are caused by a difference in thermal expansion, if the thermal expansion coefficient (TEC) of the supporting material used for graphene is known, the TEC dependence of the graphene can be calculated.[1] While measures of graphene have been made using this and other methods, there is not currently a consensus on the dependence of TEC on temperature between these studies and also the theoretical predictions.[1,16-24] Therefore additional measures of this value for graphene and multi-layered graphene are useful for more accurately determining their TECs.

1.2 Thesis overview

This chapter, chapter 1 provides a broad introduction of the subject matter, as well as an overview of the contents of the other sections in this work. Chapter 2 discusses the electron theory of graphene and few layer graphene, and elaborates on how induced strains modify this to create pseudo-electromagnetic effects. The chapter also describes Raman spectroscopy and how this can be used as a measure of strain and doping concentration in graphene. Other studies using Raman spectroscopy of graphene that have informed the calculations and analysis of this thesis are discussed here. The chapter continues by introducing

hexagonal boron nitride (h-BN), another 2D material akin to graphene, and makes points of comparison between the two materials. Chapter 2 concludes by outlining atomic force microscopy (AFM) and scanning electron microscopy (SEM) which were also used during the course of this study. Chapter 3 covers the specific predictions of the experiments carried out in this thesis. This consists of the interaction between graphene and the SiO_2 substrate surface and the changes that metal contacts would have on this system. A prediction of the expected strain is then made from a theoretical prediction of graphene TEC, followed by the expected differences with few layer and h-BN substrate graphene. Chapter 4 describes the manufacturing and design processes employed to create the graphene devices used in this study. This is followed by a description of the experimental setup used to control temperature and perform Raman microscopy as well as the means by which this was calibrated. Chapter 5 contains the results and discussion of the Raman measurements and the strain and TEC calculation of the graphene samples. Multilayer graphene is also analysed with respect to the single layer results, and an analysis of the doping concentration dependence with temperature is also performed. A preliminary examination of the results from graphene with h-BN substrates ends this chapter. Chapter 6 summarises the conclusions of the thesis as a whole as well as the potential implications of the results. The chapter ends with the means by which this work can be advanced to cover further areas of study related to the experiments performed.

2 Background

This chapter covers the background theory and practice of graphene physics and pertinent research preceding this work. The properties of graphene are explored along with the effects that strain has on these properties. The methods of inducing these strains are then elaborated upon, as well as how to use Raman spectroscopy to measure this strain and separate the signal it produces from doping and temperature effects. This chapter then introduces hexagonal boron nitride (h-BN) by its structural similarities to graphene and how this was exploited in this study. This chapter concludes with the additional measurement techniques used in the implementation of this study: atomic force microscopy (AFM) and scanning electron microscopy (SEM).

2.1 Graphene

Graphite is a three-dimensional (3D) carbon structure made of stacked two-dimensional (2D) carbon layers, each one atom in thickness. A single isolated layer of graphite is known as graphene.[3,25,26] The sp^2 hybridisation of the carbon atoms of graphene allow them to bond with three neighbouring carbon atoms in a 2D honeycomb formation. This 2D structure can be considered as the basis of all other graphitic solids of other dimensionalities. Rolling up a 2D graphene sheet creates carbon nanotubes with a one-dimensional (1D) structure; folding in two dimensions creates fullerenes of zero dimensionality; and stacking graphene creates 3D graphite.[26] While the theoretical study of graphene has been ongoing since the 1940s,[1] the isolation and analysis of graphene was only achieved in 2007.[2]

Originally, graphene and other 2D films were considered to be thermodynamically unstable: first at any temperature above zero Kelvin,[27,28] then at much lower temperatures than for viable working devices.[4] The out of plane displacements were considered energetically favourable for spontaneous folding. However, the introduction of a supporting medium and graphene elasticity allows for a metastable state of the material at room temperature.[26,29] This stability additionally allows graphene to be fabricated on substrates without a matching crystal lattice, unlike metallic thin films.[30]

Graphene has since been successfully extracted from graphite using exfoliation techniques, and has been grown by deposition directly onto a substrate.[5,31,32,33] For the majority of device applications, graphene is manufactured either by mechanical exfoliation (ME) or chemical vapour deposition (CVD). ME is the isolation of graphene, starting from a bulk graphite crystal.[5,31] A bulk graphite crystal is repeatedly cleaved and separated out across a surface which is then pressed on to a final substrate. Both graphite and graphene are transferred at random onto the substrate surface. The graphene is then manually identified for processing. While this results in relatively large (up to 1 mm) single-crystal graphene flakes, positioning and consistency are not possible due to the random distribution of the flakes.[25] This makes ME graphene a good candidate for experimental research: it is compatible with low numbers of bespoke devices and high crystal quality, suited for high sensitivity measurements with low-tech fabrication costs.

CVD graphene allows, in principle, an arbitrarily large area of graphene to be grown through a catalysed chemical reaction.[33] While there are a wide range of specific processes to achieve this, the general requirement is the cracking of a hydrocarbon gas in a non-reactive environment. The other requirement is a

catalysing surface for the resulting carbon atoms to form a graphene crystal. While CVD can produce graphene of a surface area only limited by the substrate and reaction chamber dimensions, the nature of the reaction nucleation causes grain boundaries in the graphene lattices to form. The graphene crystal growth starts from multiple nucleation points, causing misalignments in the crystal domains when they meet up. These discontinuities cause CVD graphene to have lower electrical and thermal conductivities than ME graphene.

Other feasible fabrication techniques for graphene exist: wet or dry exfoliation and molecular growth. These are not covered here because for the strain and spectroscopy applications of this study, only ME and CVD graphene are used.

2.1.1 Structure

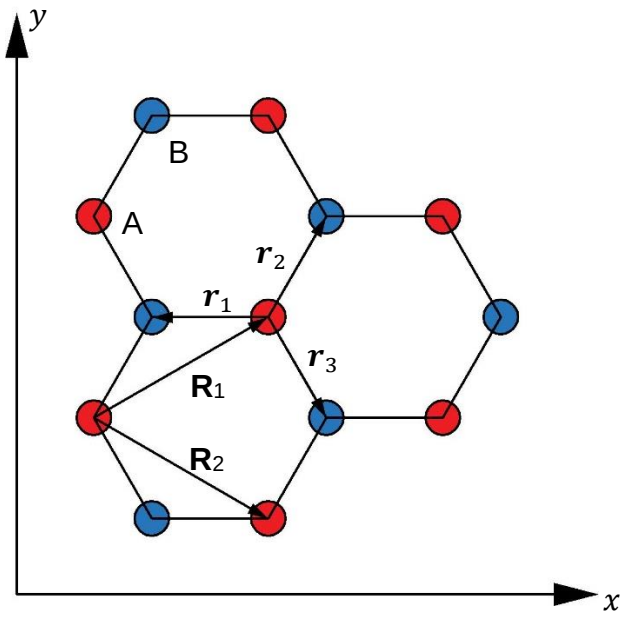

Figure 2-1: Graphene atomic lattice with the A (red) and B (blue) sub-lattices. Nearest neighbour vectors r_1, r_2, r_3, and primitive lattice vectors R_1, R_2 are shown.

The carbon atoms of graphene form a two-dimensional lattice. Each atom forms three direct chemical bonds resulting in the 2D hexagonal structure.[26] This

bonding pattern results in graphite being physically strong in the plane of the lattice. In graphite there is a weaker, Van der Waals bonding between graphene layers.[3,5,32] This explains the difference in Young's modulus of graphite, 100 GPa, with the in-plane modulus of an isolated monolayer, 1000 GPa.[34-36] Graphene is also chemically unreactive, due to the difficulty of replicating and substituting the sp^2 bond pattern required to replace a carbon atom in the lattice.[3]

The honeycomb structure of graphene can be seen as two repeating triangular lattices with an offset between each. This results in a primitive cell consisting of two atoms, one from each of the two triangular sub-lattices, conventionally named A and B. The primitive lattice vectors between the atoms on each sub-lattice, are therefore $\mathbf{R}_1 = \frac{a}{2}(3, \sqrt{3})$ and $\mathbf{R}_2 = \frac{a}{2}(3, -\sqrt{3})$, where $a = 1.42$ Å, the carbon-carbon bond length ($|\boldsymbol{r}_{1-3}|$), as shown in figure 2-1.[3,37] The 2D reciprocal lattice of graphene is similarly hexagonal in nature (figure 2-2).

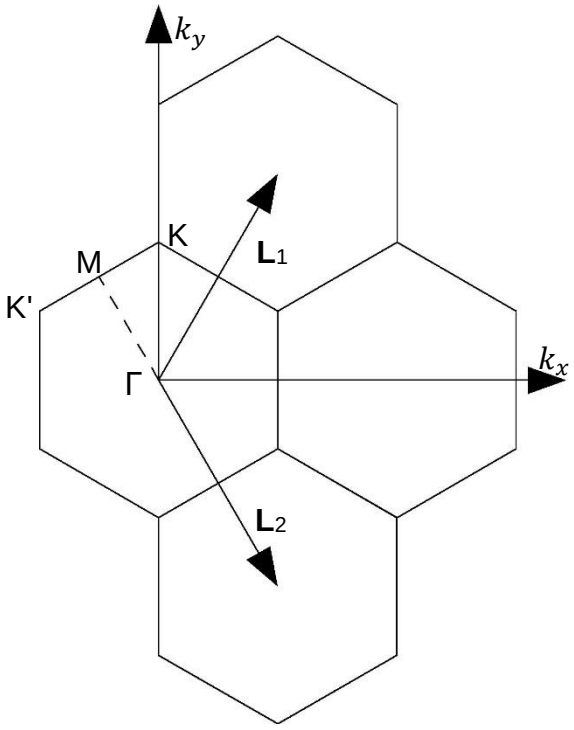

*Figure 2-2: Reciprocal space lattice of graphene with the reciprocal lattice vectors highlighted: **L**$_1$, **L**$_2$. Points of high symmetry are also marked: Γ, K and M.*

A few layers of graphene stacked together results in materials with properties which are still more comparable to comparable 2D graphene than graphite. Two layers of graphene (bilayer) stack with an offset, such that carbon atoms of the A sub-lattice of the top graphene sheet sit directly above the atoms of the B sub-lattice of the bottom graphene sheet, or *vice versa*. This is known as AB stacking (figure 2-3 (a)). Three layered graphene (tri-layer) has two stacking forms: ABA stacking, where the top and bottom graphene layers are aligned and the middle is offset as in two layered graphene; ABC stacking, where the third layer is offset from both of the other two (figure 2-3 (b)).

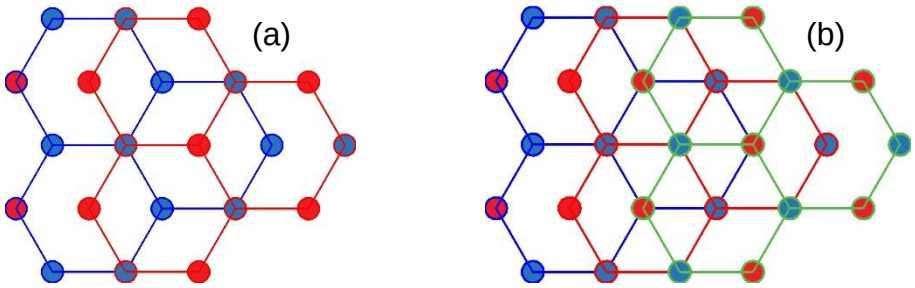

Figure 2-3: Two and three layer graphene stacking. (a) AB or ABA stacking, the separate graphene layers are colour coded with red and blue outlines and the A and B sub-lattices are shown with red and blue circles. (b) ABC stacking, the layers are colour coded with red, blue and green outlines with the same sub-lattice colouration.

2.1.2 Electronic Properties

Other noteworthy properties of graphene arise due to its unusual electron behaviour, caused by the unusual electron dispersion of graphene. This dispersion can be predicted using the tight binding approximation of solids.

Tight binding approximation

To fully solve the Hamiltonian for this material, the electron interactions within and between each sub-lattice, $\boldsymbol{A}$ and $\boldsymbol{B}$, must be considered:

$$\begin{pmatrix} \varphi_A^* H \varphi_A & \varphi_A^* H \varphi_B \\ \varphi_B^* H \varphi_A & \varphi_B^* H \varphi_B \end{pmatrix} = \epsilon \begin{pmatrix} \varphi_A^* \varphi_A & \varphi_A^* \varphi_B \\ \varphi_B^* \varphi_A & \varphi_B^* \varphi_B \end{pmatrix}. \quad (2.1)$$

However, taking only the first order interactions of the electrons is a sufficient approximation to demonstrate the properties of electrons in graphene. Including only the $\boldsymbol{r}_1$, $\boldsymbol{r}_2$, $\boldsymbol{r}_3$ vectors excludes A → A or B → B lattice transitions and simplifies the diagonal terms in equation (2.1), which are the difference in on-site energy between the A and B lattice locations. In graphene, this is zero as the A and B sites are identical, thus expanding the potential as a Bloch wave leads to:

$$\begin{pmatrix} 0 & \varphi_A^* H \varphi_B \\ \varphi_B^* H \varphi_A & 0 \end{pmatrix} = \begin{pmatrix} 0 & -t \sum_i e^{i\boldsymbol{k}.\boldsymbol{R_i}} \\ t^* \sum_i e^{-i\boldsymbol{k}.\boldsymbol{R_i}} & 0 \end{pmatrix}, \quad (2.2)$$

where t is the parameter for nearest-neighbour hopping energy:

$$t = N \sum_i \int \varphi_B^*(\boldsymbol{r}) H \varphi_A(\boldsymbol{r} - \boldsymbol{R_i}) d\boldsymbol{r}, \quad (2.3)$$

and

$$t^* = N \sum_i \int \varphi_A^*(\boldsymbol{r}) H \varphi_B(\boldsymbol{r} - \boldsymbol{R_i}) d\boldsymbol{r}. \quad (2.4)$$

These off-diagonal terms represent the probability amplitude for an electron to travel between nearest neighbour atomic sites, and have equal modulus squared values. By defining $\boldsymbol{r}$ as the real space vector, as given in figure 1-1: $\boldsymbol{r}_1 =$

$\left(-\frac{1}{\sqrt{3}}a, 0\right)$, $\boldsymbol{r}_2 = \left(\frac{1}{2\sqrt{3}}a, \frac{1}{2}a\right)$, $\boldsymbol{r}_3 = \left(\frac{1}{2\sqrt{3}}a, -\frac{1}{2}a\right)$ and $\boldsymbol{k}$ as the 2D reciprocal space vector: $\boldsymbol{k} = \left(\frac{k_x}{a}, \frac{k_y}{a}\right)$. This gives the first order approximation of the energy to be

$$\epsilon^2 = t^* t \left[1 + 4\cos\frac{k_y}{2}\left(\cos\frac{k_y}{2} + \cos\frac{k_x\sqrt{3}}{2}\right)\right]. \quad (2.5)$$

An approximate value of t has been calculated as $t \approx 2.7$ eV, yielding the dispersion shown in figure 2-4.[1,3]

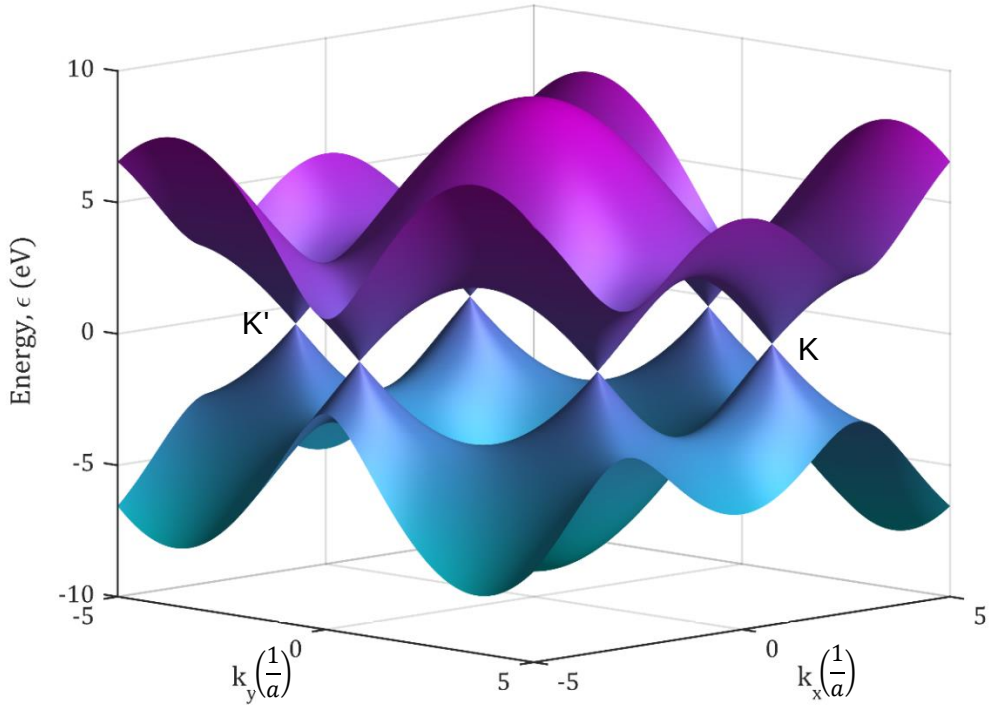

Figure 2-4: First order approximation of the electronic dispersion of a honeycomb lattice made from two identical sub-lattice elements. The opposing corners of the first Brillouin zone K and K' are labelled.

Results

This dispersion reveals that graphene has no electronic band gap, classifying graphene as a semi-metal. The points that the conduction and valence bands meet are at the K and K' points, at the corners of the first Brillouin zone in figure 2-2.

In the low energy regime around the K points, <1 eV, the energy of electrons has an unusual, linear dependence on momentum. This can be shown by taking the dispersion at one of the K-points: from figure 2-2 or 2-4, $\left(0,\frac{4\pi}{3a}\right)$ and expanding a small distance in k-space around this position: $\left(\delta k_x,\ \frac{4\pi}{3a}+\ \delta k_y\right)$. This is substituted into equation (2.5), making the diagonal terms:

$$t\sum_{R} e^{i\boldsymbol{k}.\boldsymbol{R}} = t\left[2e^{-i\frac{a\delta k_x}{2\sqrt{3}}}\cos\left(\frac{2\pi}{3}+\frac{a\delta k_y}{2}\right)+e^{i\frac{a\delta k_x}{\sqrt{3}}}\right], \quad (2.6)$$

and

$$t^{*}\sum_{R} e^{-i\boldsymbol{k}.\boldsymbol{R}} = t\left[2e^{i\frac{a\delta k_x}{2\sqrt{3}}}\cos\left(\frac{2\pi}{3}+\frac{a\delta k_y}{2}\right)+e^{-i\frac{a\delta k_x}{\sqrt{3}}}\right], \quad (2.7)$$

respectively. By defining $\delta k \ll 1$, and $\delta k^2 \approx 0$, equations 2.6 and 2.7 can be simplified using first order Taylor expansions of the exponential terms, giving a modified equation (2.2):[6]

$$\boldsymbol{H} = \frac{\sqrt{3}}{2}at\begin{pmatrix} 0 & i\delta k_x - \delta k_y \\ i\delta k_x + \delta k_y & 0 \end{pmatrix}. \quad (2.8)$$

This Hamiltonian can also be described as a combination of Pauli spin matrices:[3]

$$\boldsymbol{H} = v_F\boldsymbol{\sigma}.\boldsymbol{p}, \quad (2.9)$$

where the wavenumber $\delta k\hbar$ has been substituted for momentum $\boldsymbol{p} = (p_x, p_y, p_z)$, $\boldsymbol{\sigma}$ is the vector of the Pauli matrices $(\sigma_x, \sigma_y, \sigma_z)$, and $v_F = \frac{\sqrt{3}at}{2\hbar} \approx 1\times10^{6}$ ms^{-1}.[3,6] In the case of the 2D graphene system, $p_z = 0$. This results in an electron Hamiltonian resembling the massless Dirac Hamiltonian, thus a linear dispersion of momentum in the low energy regime of graphene:

$$\frac{\partial E}{\partial p} = v_f. \quad (2.10)$$

This behaviour is usually only observable in free space with massless particles, such as a photons energy having a dispersion of $\frac{\partial E}{\partial p} = c$ while typical massive particles have a $\frac{\partial E}{\partial p} = 2pc^2$ dispersion, where c is the speed of light in vacuum. This creates the potential to simulate the realm of ultra-relativistic Dirac particles, using electrons, at greatly reduced experiment speed and size requirements.[3,25,26]

Chirality

So far, the approximation has only been solved around the K point. Equation (2.9) has two different solutions for the wave function corresponding to the K and K' points:

$$\varphi_{\boldsymbol{k}}^{K} = e^{i\boldsymbol{k}.\boldsymbol{r}}\begin{pmatrix}\pm 1\\ e^{i\theta_{\boldsymbol{k}}}\end{pmatrix}, \qquad \varphi_{\boldsymbol{k}}^{K'} = e^{i\boldsymbol{k}.\boldsymbol{r}}\begin{pmatrix}e^{i\theta_{\boldsymbol{k}}}\\ \pm 1\end{pmatrix}, \quad (2.11)$$

where the ± 1 term defines the dispersion band: $+1$ for conduction band (electrons) and -1 for valence band (holes) and $\theta_{\boldsymbol{k}}$ is the angle of the momentum space vector. These two solutions can be seen as either in the direction of $(\varphi_{\boldsymbol{k}}^{K})$, or against the direction of $\left(\varphi_{\boldsymbol{k}}^{K'}\right)$ the particle motion, which makes it analogous to quantum spin. This chirality is called pseudo-spin, where spin up and down are replaced with the electron existing at either the K or K' points. The pseudo-spin causes resistance to the backscattering of electrons: scattering from wave vector $\boldsymbol{k}$ to $-\boldsymbol{k}$ is suppressed as the respective chirality around the K and K' are opposite.[38] This allows for ballistic transport effects in the order of microns in length to be created at low temperatures, and in the hundreds of nanometres at room temperature.[3,25,26]

The combination of massless particle behaviour with low scattering/interaction effects also allows the observation of quantum effects at room temperature in graphene, such as the quantum Hall effect. This means that graphene may allow for the design of practical devices based on quantum or relativistic effects.

2.1.3 Multi-layer graphene

The addition of a second graphene layer creates inter-layer electron hopping paths into the Hamiltonian. These inter-layer hopping potentials are relevant around the K and K' points in the two-layer graphene Brillouin zone, resulting in a 4x4 matrix version of equation (2.8).[3] The additional off-diagonal terms from the inter-layer effects cause the K/ K' dispersion to have a quadratic relation. Therefore only single layer graphene exhibits massless electron dispersion as this quadratic dispersion is present in all graphene stacks up to graphite.

Additionally, a band gap can now be introduced in layered graphene by creating diagonal terms in its Hamiltonian matrix. These diagonal terms are caused by effects that break the inversion symmetry of the lattice, such as a potential difference between the top and bottom graphene layers. Therefore, this effect is difficult to induce outside of multilayer graphene.

Multilayer graphene maintains the chirality properties of single layer graphene, resisting backscattering based in its momentum position on the K or K' point in the Brillouin zone.[25,38,39]

2.2 Strain

When a force is applied to a solid, a certain amount of deformation is induced – a change of shape or volume. This displacement is described by a vector $\boldsymbol{u}$:[40]

$$\boldsymbol{u}_i = x'_i - x_i, \quad (2.11)$$

where $i = 1 - 3$ being the three spatial dimensions, x_i is a co-ordinate before the deformation, and x'_i after the deformation, given as a function of the x_i co-ordinate. Likewise, if two points in the material are separated by a small distance defined by a vector, $d\boldsymbol{x}_i$, the distance after deformation is

$$\Delta\boldsymbol{x}'_i = \Delta\boldsymbol{x}_i - \Delta\boldsymbol{u}_i. \quad (2.12)$$

By defining the scalar distance before and after the deformation as dl and dl' respectively, all these terms can be related by

$$\Delta l'^2 = \Delta l^2 + 2\boldsymbol{u}_{ik}\Delta\boldsymbol{x}_i\Delta\boldsymbol{x}_k, \quad (2.13)$$

and

$$\boldsymbol{u}_{ik} = \frac{1}{2}\left(\frac{\partial u_i}{\partial x_k} + \frac{\partial u_k}{\partial x_i} + \frac{\partial u_h}{\partial x_i}\frac{\partial u_h}{\partial x_k}\right). \quad (2.14)$$

$\boldsymbol{u}_{ik}$ is the strain tensor where i, k and h refer to the three perpendicular spatial axes, meaning any strain can be separated out into contributions from three spatial dimensions. In the case of a supported graphene membrane, the out of plane component is ignored and only strains in the $x - y$ plane are considered:

$$\boldsymbol{u}_{xx} = \frac{\partial u_x}{\partial x} \quad (2.15)$$

for a linear strain, and

$$\boldsymbol{u}_{xy} = \frac{1}{2}\left(\frac{\partial u_x}{\partial y} + \frac{\partial u_y}{\partial x}\right) \quad (2.16)$$

for a shear strain.

Strain will affect the chemical potential of a graphene lattice: changing the area of the lattice will change the electron density. Additionally, atomic bond lengths

will change depending on their orientation to the strain. In the tight binding model, changes in the bond length will change the lattice vectors, $\boldsymbol{r}_n$, and the hopping energy parameter. The change in bond length can be expressed as

$$\Delta u_i = \frac{\Delta_{ab}}{a}.(\boldsymbol{u}_a - \boldsymbol{u}_b), \quad (2.17)$$

where subscripts a and b denote the different sub-lattices, connected by the atomic bond. This modifies the hopping potential, t, from the graphene Hamiltonian, equation (2.2) to t', where

$$t' = t + \frac{\partial t}{\partial a}\Delta u_i. \quad (2.18)$$

This modifies the Hamiltonian with an effective potential, dictated by the strain tensor u_{ij}, where i and j are now the x-y axes instead of the sub-lattice hopping vector:

$$\boldsymbol{A} = \gamma \begin{pmatrix} u_{ii} - u_{jj} \\ -2u_{ij} \end{pmatrix}, \quad (2.19)$$

where $\gamma = -\frac{3}{4}\frac{\partial t}{\partial(\ln(a))}$. This allows for the construction of an arbitrarily complex potential field, $\boldsymbol{A}$, using a combination of linear and shear components of the strain tensor to satisfy equation (2.19). This potential field can therefore be used to imitate other fields, such as electric or magnetic fields, through the manipulation of the strain tensors. For example, a magnetic field can be mimicked with a triangularly symmetric strain pattern.[42-44] However, unlike a true magnetic field, instead of causing opposite forces on opposing charges, this pseudo-magnetic field has opposite forces at the K and K' points of the Brillouin zone. This type of field control opens up the exploration of valleytronics: the manipulation of electrons based on their position in reciprocal space.[9-11]

Applicable strain engineering would be an effective tool to add to the manipulation of electronics in graphene devices. Strains have been induced in graphene through various methods:

2.2.1 Flexible substrate

Flexible substrates are a simple and direct method of applying strain to graphene membranes.[12-15] Graphene is exfoliated or transferred onto a polymer substrate such as acrylic (PMMA) or polycarbonate (PC). The aim is to use the Van der Waals forces between the graphene and polymer to exert a straining force on the graphene as the polymer is physically bent (figure 2-5). This is effective at inducing uniaxial strains in the order of 1 %, with higher values of tensile than compressive strain achieved due to the graphene buckling under compression.[12] Biaxial strains are also possible with a five-point bending pattern.[15] This method is limited by the substrate thickness: a thinner substrate allowing for a larger strains; and the large difference in Young's modulus between graphene (1000 GPa) and the polymers (>5 GPa) used, limiting how much the substrate will deform the graphene and not the reverse.[12-15,34-36]

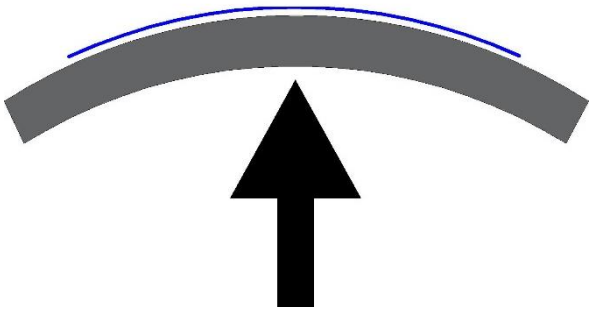

Figure 2-5: Flexible substrate (grey) straining of graphene (blue) from an applied force in the direction of the arrow.

2.2.2 Bubbles and blisters

Gas molecules are unable to permeate a graphene membrane. This has been used as another avenue to induce strain.[42,44,45] Either by trapping bubbles during the manufacture process or by creating pressurised cells below the graphene, a pressure difference is created above and below the graphene (figure 2-6). While this can create strains in the order of 1%, the positioning of bubbles is random, and both blisters and bubbles cannot strain the entire graphene flake or create a strain of arbitrary configuration.

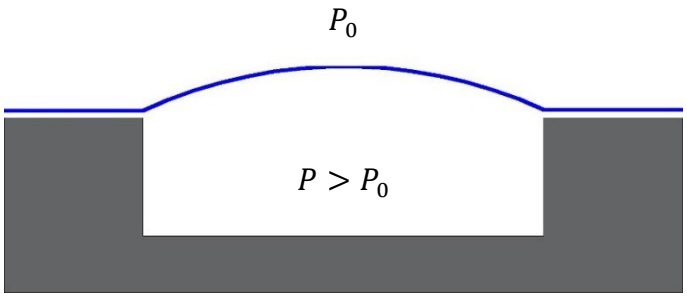

Figure 2-6: Graphene (blue) blister over a hole in the substrate (grey). Strain is induced when $P \neq P_0$.

2.2.3 Thermal expansion

As explored in this study, graphene is strained through heating when it is on a substrate with a different thermal expansion coefficient to it. Graphene has an unusual thermal expansion coefficient (TEC), as it is predicted to be negative over a large temperature range covering all standard device operating temperatures.[20,21,23,24] This causes graphene to even be significantly strained on silicon substrates, commonly used for electronic devices, when the temperature is varied (figure 2-7). This has been shown to produce consistent, isotropic biaxial strains. The strain magnitude is limited by the temperature difference that can be applied and has been measured in the order of 0.1% when decreasing

temperature from room temperature, and 0.2% when increasing.[46] As in the flexible substrates, there are also observations of slipping and crumpling when the strain force becomes greater than the Van der Waals interaction forces on the graphene.[46-48]

Figure 2-7: Strain induced by substrate (grey) and graphene (blue) in the case of decreasing temperature. The substrate shrinks (grey arrows) and the graphene tries to expand (blue arrows).

Contact effects

In order to perform electronic measurements on graphene, metal contacts are deposited on the top or side of a flake to create a circuit involving the desired graphene (figure 2-8). In the case of thermally strained graphene, these contacts can make a difference to the resultant effects.

Figure 2-8: Schematic of graphene flake (blue) with Cr/Au top contacts (yellow).

The slipping and buckling observed in both the flexible substrate and thermal expansion strain experiments may be supressed if metal contacts offer additional pinning of the graphene. This can be as an increase in the Van der Waals forces from both sides of the graphene flake, or additional pinning can be added by etching holes through the graphene first to make contacts that ‘nail’ through the

graphene, as used in suspended graphene structures. This extra pinning force could allow these straining techniques to exceed the strain limit observed when graphene buckles or slips on the substrates, and particularly so in the slipping case.[49]

Metal deposition itself has also been observed to induce strain in 2D materials. Metal deposition processes occur at high temperatures for the evaporated metals. The cooling and settling process the metals undergo once deposited causes local strains around these metal features such as contacts and nanoparticles.[50-52] It is worth considering the combined strain effects of metal deposited contacts in temperature-variable graphene systems, such as low temperature transport, as undesirable strains may be induced.

Motivation

Characterisation of these strain systems is important to ensure that unintended strain field effects are not induced when using graphene devices. While simple strain geometries are not expected to influence the electron properties of graphene, large strain magnitudes and complex strain tensors can be expected to change these properties.[42,43,53] Therefore, the magnitude of strain and their dependence with temperature is an important factor to consider, as well as contact type and geometry, when creating electronic devices which undergo temperature fluctuations, and is the main motivation of this work. This study seeks to be a direct measurement of thermal strain of graphene samples that are in the style of electronic transport devices.[17,19,46-48,54,55]

The thermal expansion strain is directly influenced by the thermal expansion coefficient (TEC) of graphene. So far, this TEC has not been measured below 100 K and previous measures show large disagreement between each other and

theoretical predictions.[16-21,23,48] therefore this study of thermal strains can be used as a measure of the TEC of graphene over an unexplored range, and as a comparison to previous results and theory.

2.3 Raman spectroscopy

Raman spectroscopy is an excellent method for measuring the structural and electronic properties of a material in a non-destructive manner. Raman spectroscopy is the measure of inelastically scattered laser light off a material. While the majority of laser light incident on a material undergoes Rayleigh scattering, a small fraction of photo-excited electrons can also couple to the material's lattice vibrations.[56]

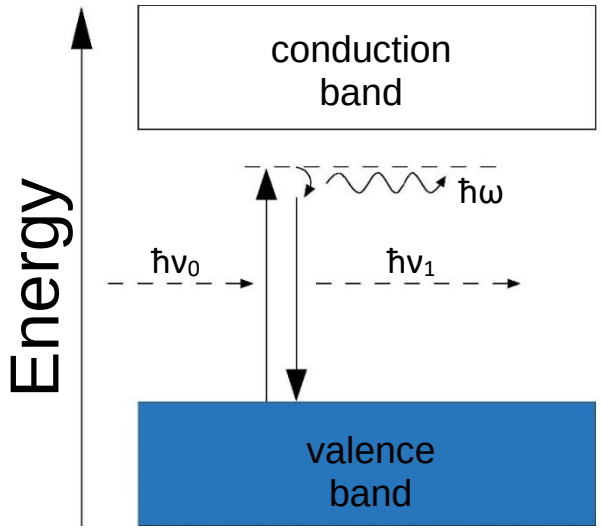

Figure 2-9: Stokes scattering process of a photon incident on some material, involving an incident photon ($\hbar\nu_0$), emitted photon ($\hbar\nu_0$) and generated phonon ($\hbar\omega$).

These lattice vibrations, of frequency ω, are quantised and are described as quasi-particles called phonons. When an excited electron creates, or absorbs a phonon, the light emitted by the electron returning to its ground state will have a

decreased energy (Stokes shift) or increased energy (anti-Stokes shift) respectively. Since the properties of phonons are sensitive to both the lattice structure and electronic properties, this information is carried into the Stokes (or anti-Stokes) spectral information.

Raman scattering does not require a resonant transition. As shown in figure 2-9, the valence electron can be excited to a virtual state at normally forbidden energy levels, removing the need to tune the laser excitation wavelength to the band gap of the material being probed. Non-resonant Raman spectroscopy takes advantage of these virtual state excitations to be able to measure materials with laser wavelengths lower than the material band gap, and to measure multiple materials with different band gaps simultaneously. Resonant Raman spectroscopy uses the increased probability of incident photon absorption that comes from a real electron transition to obtain a larger resultant Raman signal from a material.

Light cannot couple to all phonon vibration modes. “Raman active” phonons require polarizable lattice bonds for a dipole oscillation that the photons couple to, and must also obey momentum and energy conservation laws.

2.3.1 The phonons of graphene

For graphene, the two optically active phonons used in Raman spectroscopy are at the Γ and K points of the dispersion. They are labelled by the symmetry of their vibrational modes in figure 2-10 as the E_{2g} and A_{1g} phonons.

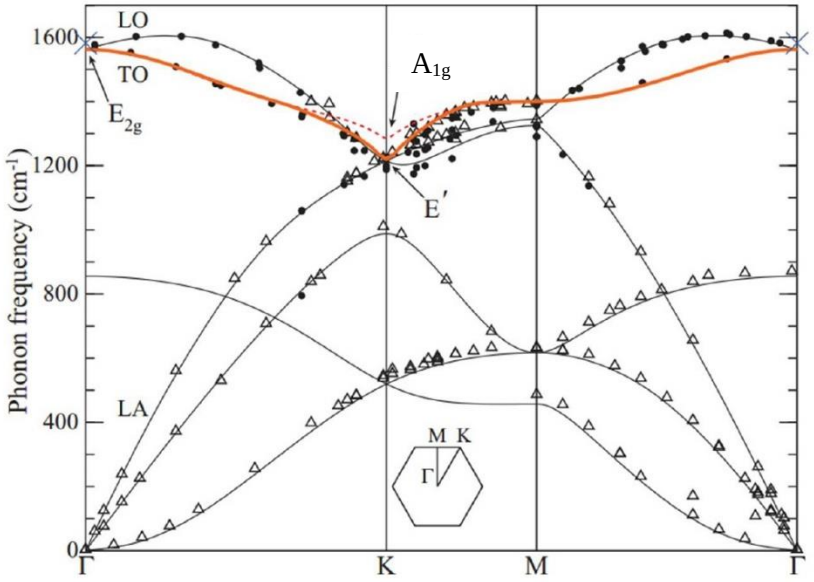

Figure 2-10: Theoretical (lines) and measured (points) phonon dispersion of graphene, adapted from Venezuela et al.[57]

The E_{2g} phonon exists at the centre of the first phonon Brillouin zone at the Γ point. The lattice motion of this phonon has the two atomic sub-lattices oscillating in opposite phase to each other. There are two degenerate vibrational modes of the E_{2g} phonon, related by the orientation of the oscillations to the lattice, shown in figure 2-11.

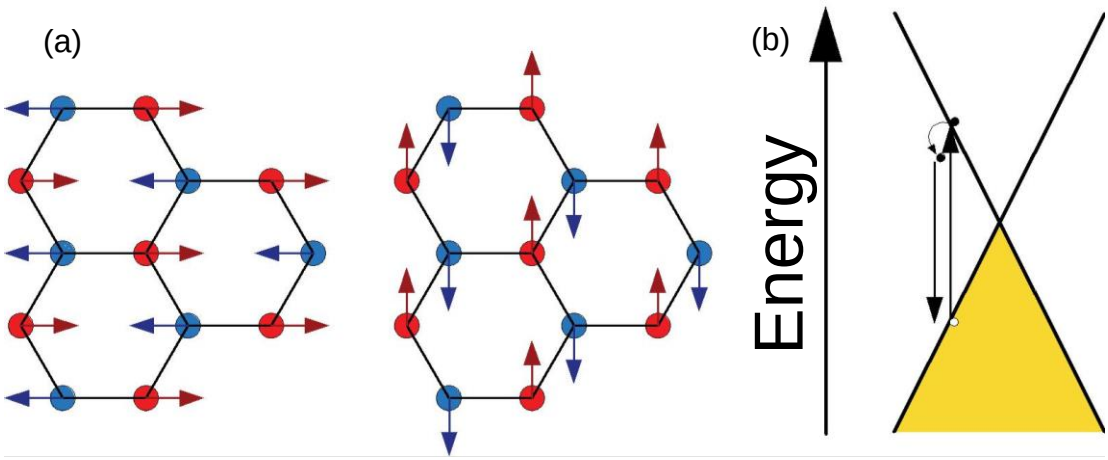

Figure 2-11: Graphene E_{2g}/G peak phonon vibrational modes (a), and associated electron energy transition (b).

The optical transition of the Raman interaction is resonant at all light wavelengths due to the linear electron dispersion always allowing a direct electron transition from the valence band to the conduction band. This boosts the interaction probability of the Raman scattering event. The spectral peak associated with this transition is also present in graphite, and is known as the G peak.

The A_{1g} phonon exists at the corner of the first Brillouin zone, at the K point. The lattice motion is a “breathing” oscillation of the hexagonal lattice structures of graphene. The large phonon momentum of the K point prevents Raman access to this phonon under usual conditions, therefore the phonon requires either an elastic electron scattering event off a lattice defect or a second-order scattering event, creating two phonons with opposite momentum, to be Raman active.

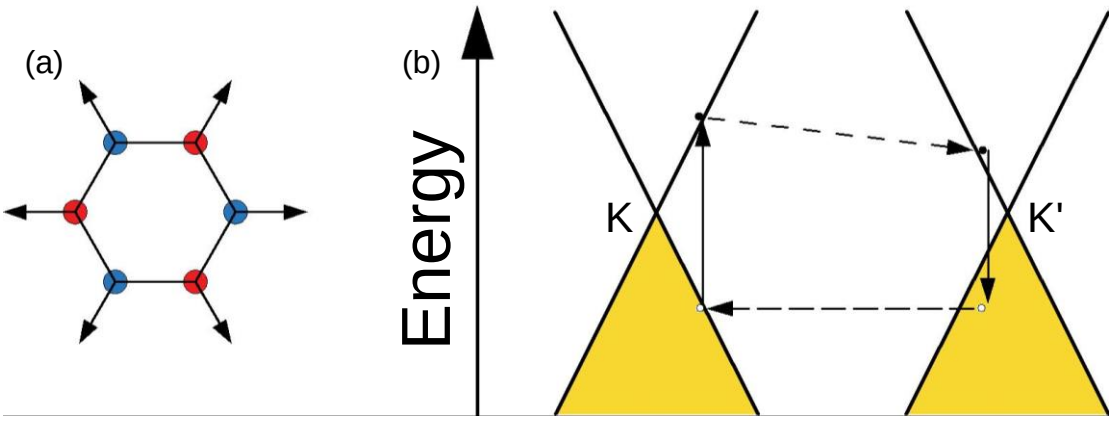

Figure 2-12: (a) A_{1g} phonon mode of the D and 2D graphene Raman peaks. (b) One possible electron scattering path of the D spectral peak: the first inter-valley transition creating a phonon, while the second is an elastic scattering event off a defect. The 2D peak has both inter-valley transitions create phonons.

This multiple electron scattering Raman process of the A_{1g} phonon causes it to be doubly resonant, as both the initial excitation and the inter-valley scattering to both begin and end in real electron states, further enhancing the interaction probability. There are two Raman spectral peaks associated with the A_{1g} phonon: the D peak, which is associated with the defect scattering event (figure 2-12 (b)),

and is used as a measure of graphene quality, with perfect, single-crystal graphene having zero intensity of this peak. The 2D peak is the second harmonic of the D peak and is caused by double phonon creation, and is therefore always present. The D and 2D peak energies are dependent on the excitation wavelength. The energy of optical photon excitations puts them beyond the near-K approximation made for equation (2.8), and beyond the linear dispersion regime in figure 2-4. The return to a non-linear dispersion causes the energy of the inter-valley scattering (figure 2-12) to shift with photon energy by about 50 cm^{-1} eV^{-1} in the optical range.[58-60]

2.3.2 Raman of graphene

The Raman spectrum of graphene can be used to identify the number of graphene layers in a particular flake, and also contains information of its quality, strain and doping due to their effects on the lattice phonons.[47,48,59,61] Examination of the D, G and 2D Raman peaks is used to define these qualities.

Monolayer

The Raman spectrum of monolayer graphene consists of two main spectral peaks: the G and 2D peaks, whose mechanisms have been described in the previous section (2.4.1). The G peak is located around 1585 cm^{-1} and the 2D peak around 2700 cm^{-1} and both have a Lorentzian peak shape as only natural broadening is present. Approximate values are given due to sample-dependent strain and doping shifts of the peak positions, and the 2D peak dispersion with excitation wavelength (section 2.3.1). The D peak does not appear in defect free graphene, such as figure 2-13, but is at half the energy shift of the 2D peak. The D+D'' peak visible in figure 2-13 comes from an alternate inter-valley scattering that involves a combination of an A_{1g} and an E' phonon, from the K point in figure

2-10.[62] This peak appears around 2450 cm^{-1} and is slightly asymmetrical due to its sub-components. The D+D'' is not used as often for Raman spectral analysis over the G or 2D peaks due to its comparatively lower signal intensity. The identifying features for monolayer graphene are a single-Lorentzian 2D peak, and the 2D/G peak intensity ratio between 2 and 5, which varies with doping.

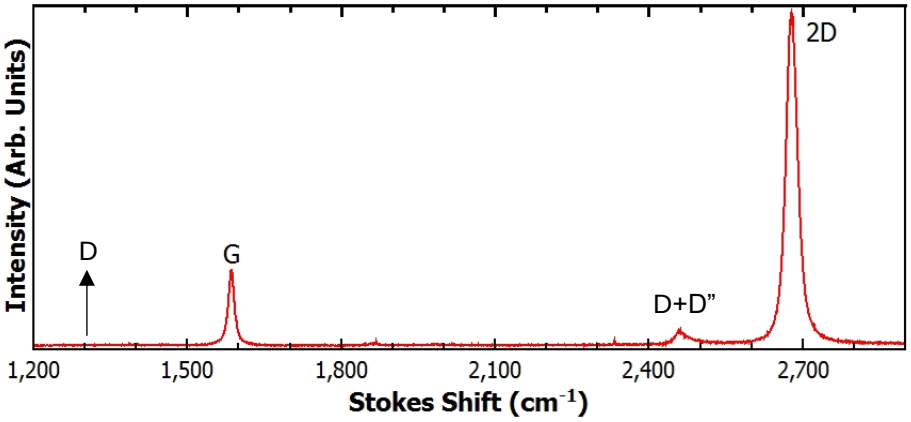

Figure 2-13: Raman spectra of monolayer graphene from 1200 cm^{-1} to 2900 cm^{-1} with peaks of interest labelled, as measured with a 532 nm laser. The absence of the D peak comes from the probed area being a single crystal and defect free.

Bilayer

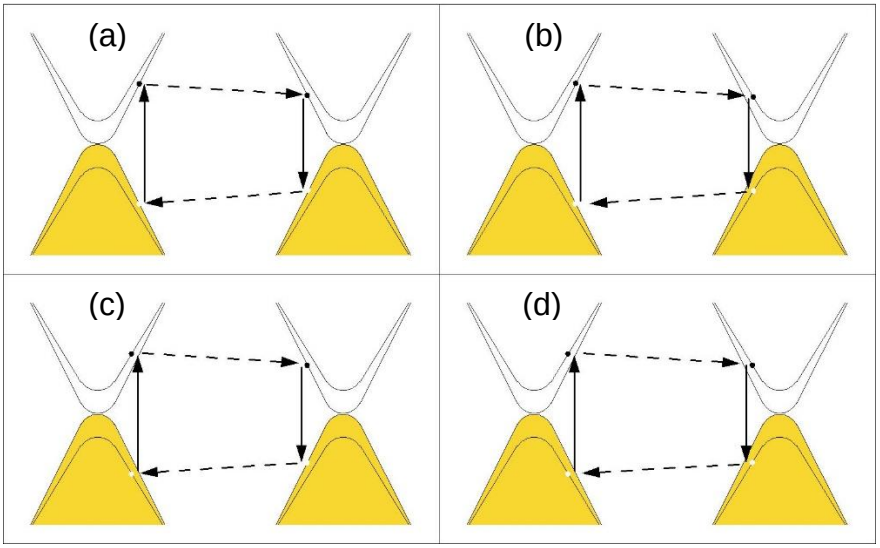

Figure 2-14: (a-d) 2D Raman scattering paths of bilayer graphene.[63]

Bilayer graphene has the same peak distribution as monolayer graphene with the exception of the 2D peak. For bilayer graphene, the 2D peak is shifted to higher energy, has an increased peak width and an internal structure involving four sub-peaks. This is caused by the modified electron distribution at the K-point in bilayer graphene, allowing for four different Raman scattering pathways of slightly different energies and interaction probabilities, shown in figure 2-14. These four different scattering paths give rise to the four sub-peaks of differing energies and intensities, giving the combined 2D bilayer graphene peak a left-sloping top, and a shoulder protrusion, show in the inset of figure 2-15.

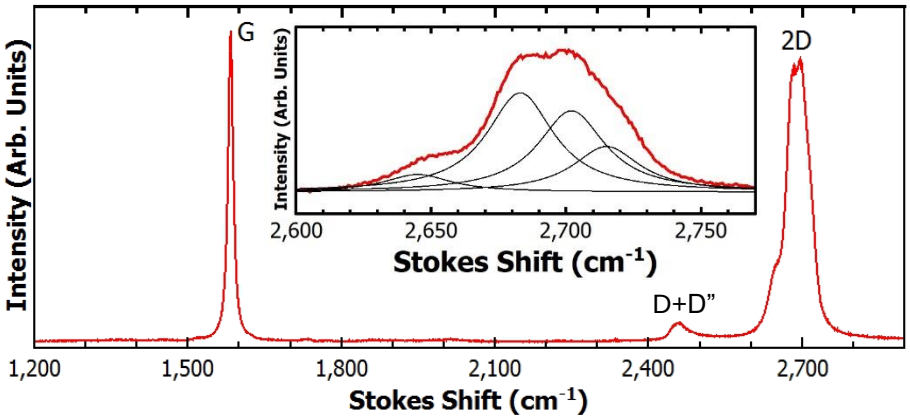

Figure 2-15: Raman spectra of bilayer graphene from 1200 cm^{-1} to 2900 cm^{-1} with peaks of interest labelled, as measured with a 532 nm laser. The inset shows an expanded view of the 2D peak, with an approximate fit of the four sub-peak features in black.

Bilayer graphene is most easily identified by a shoulder in the 2D peak, and a 2D/G peak intensity ratio in the range of 0.75 to 1.5.[64] The change in relative intensities arises from the dispersal of the 2D peak sub-elements, combined with a linear scaling of G peak intensity with number of graphene layers.[64]

Tri-layer

Tri-layer graphene has a similar peak profile to monolayer and bilayer graphene and maintains the broadened, non-Lorentzian profile of the 2D peak from bilayer

graphene (figure 2-16). The 2D peak has a different profile to the 2D case however, missing the shoulder feature, and having a right-facing slope at the top (figure 2-16, inset). This particular 2D peak shape is unique to tri-layer graphene, as well as a 2D/G peak ratio from 0.75 to 0.5.[64]

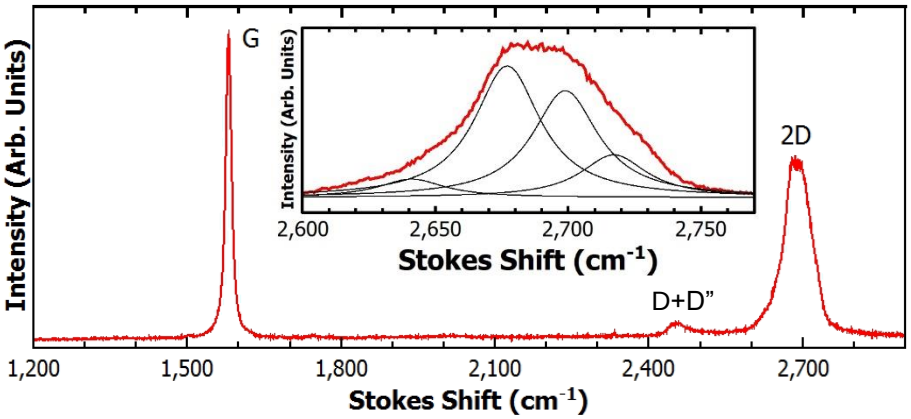

Figure 2-16: Raman spectra of trilayer graphene from 1200 cm^{-1} to 2900 cm^{-1} with peaks of interest labelled, as measured with a 532 nm laser. The inset shows an expanded view of the 2D peak, with an approximate fit of the four sub-peak features in black.

2.3.3 Strain effect on Raman spectra

Since lattice vibrations are significantly affected by the properties of the lattice, they make an excellent measure of changes in the properties of a substance. Therefore, effects such as strain, doping and temperature, addressed in sections 2.3.3, 2.3.4, and 2.3.5 respectively, can be measured through changes in the Raman spectrum of graphene. These effects are described for monolayer graphene only as the mechanisms do not change for bilayer and tri-layer graphene.

The volume of a crystal lattice is related to vibrational properties by the Grüneisen parameter, which is a material-specific value that determines the change in phonon vibrational frequency with a change in lattice volume or density.[13]

Therefore, a deforming strain of the graphene lattice causes a shift in the associated phonon energies.

Uniaxial strain

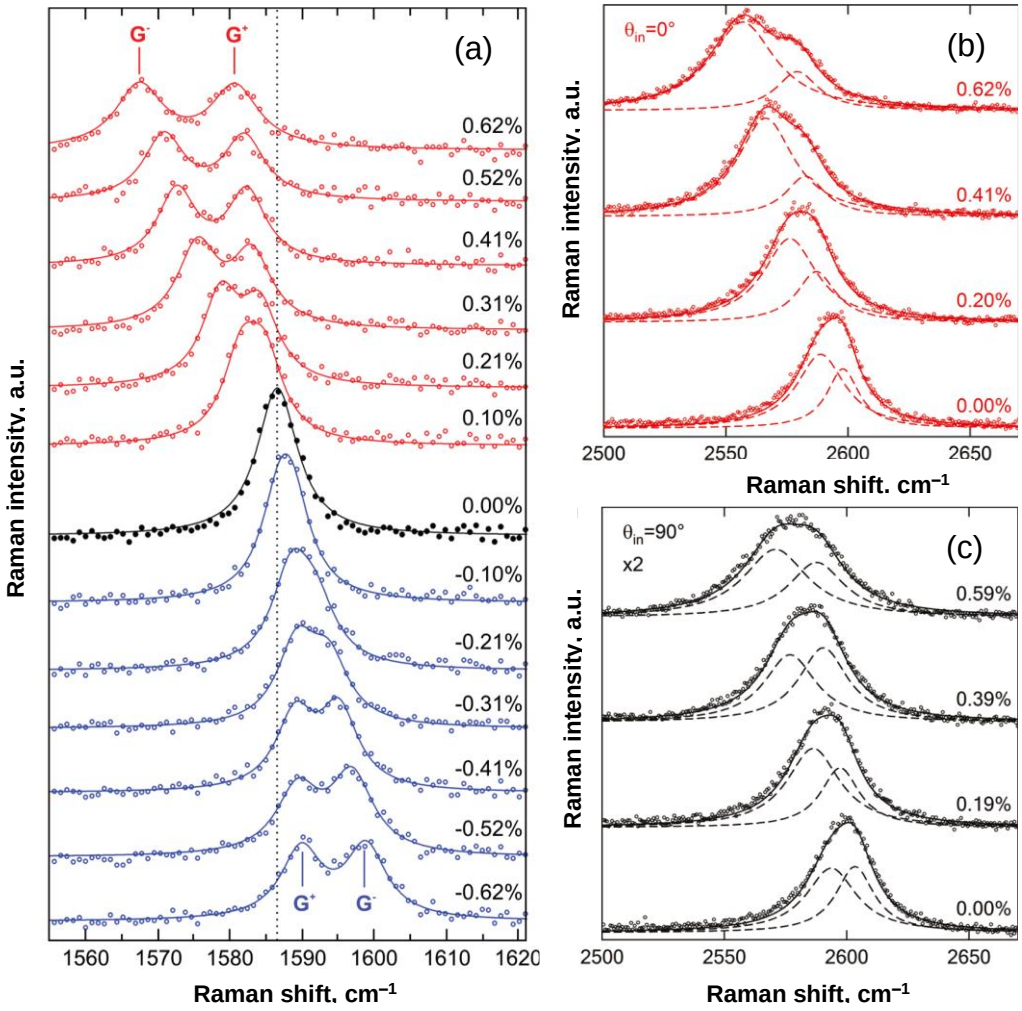

Figure 2-17: Splitting of G and 2D Raman peaks induced by uniaxial strain, from substrate deflection, as measured with a 785 nm laser. (a) G peak strain splitting with both tensile (red) and compressive (blue) strains, the split peaks are labelled G^+ and G^-, adapted from Frank et al.[14] (b) 2D peak strain splitting with tensile strain and laser polarisation parallel to the strain axis. (c) 2D peak strain splitting with tensile strain and laser polarisation perpendicular to the strain axis. Data of (b) and (c) adapted from Frank et al.[65]

In addition to shifting the energy of the Raman peaks, a uniaxial strain breaks the directional degeneracy of the graphene lattice. This causes the G peak to split into two components. Additionally, the 2D peak undergoes a polarisation-dependent split. Both splittings are related to the orientation of the graphene lattice to the strain direction.[13,14,65,66] This has been observed in graphene

strained by a flexible substrate undergoing a two-point bend, such as shown in figure 2-5.

Uniaxial strains cause a peak shift of 29 cm^{-1}/% for the G^- component and 10 cm^{-1}/% for the G^+ component and is the same for compressive and tensile strains, with compression giving a positive shift and tensile negative (figure 2-17).[13,14,67] The 2D peak exhibits a shift of 59 cm^{-1}/% for the lower energy component, and 31 cm^{-1}/% for the higher component with only the relative magnitude of the peaks changing with polarisation angle.[65,66] Shift values are derived from an average of results, and have an uncertainty of 10%.

Biaxial strain

The isotropic nature of biaxial strain keeps the directional degeneracy of the graphene phonons intact so peak splitting, such as in the uniaxial case, does not occur. Biaxial strain has been achieved as a five-point bending of graphene on a flexible substrate, as well as in pressurised graphene balloons and blisters.[13,15,44] The biaxial strain dependence on peak position was measured to be 57 cm^{-1}/% for the G peak, and 144 cm^{-1} for the 2D peak, with 5% uncertainty, giving a negative shift for tensile strain and a positive shift for compressive (figure 2-18).[13,15,44] In conclusion, both lattice strains, uniaxial and biaxial, will cause a decrease (increase) in phonon energy with tensile (compressive) strain, but only strains with a uniaxial component will cause a broadening or splitting of the G peak, or polarisation dependent 2D peak splitting.

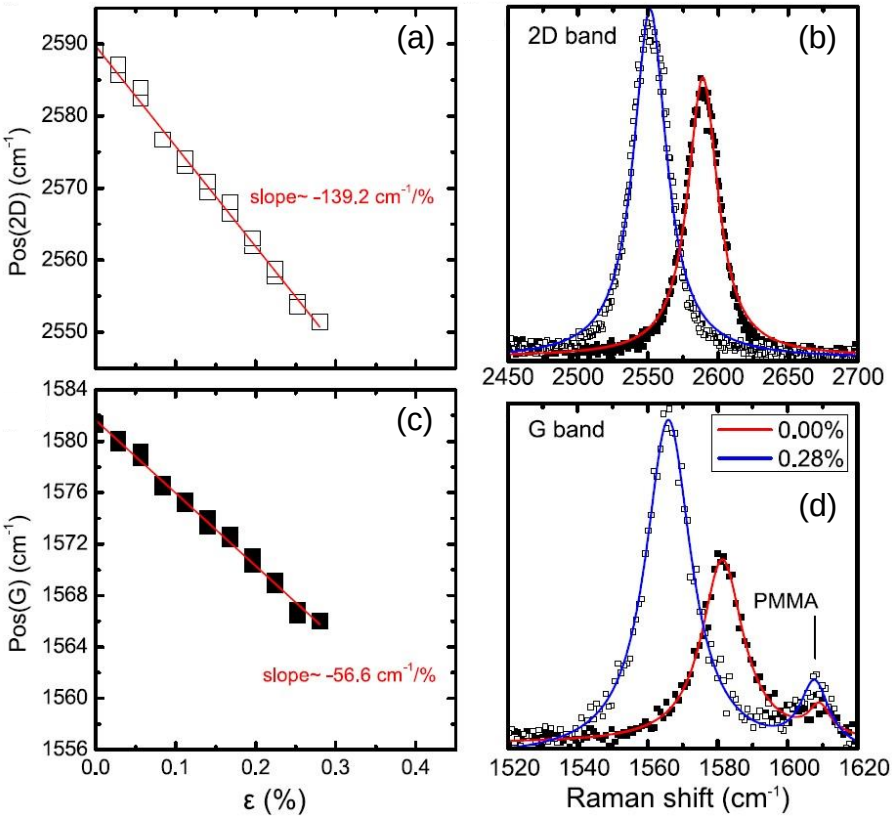

Figure 2-18: Strain shift of the 2D peak (a, b) and G peak (c, d), using the tensile strain of a five-point substrate deflection and 785 nm laser. The total trend with strain is shown in (a) and (c), with an example peak shift shown in (b) and (d). Data adapted from Androulidakis et al.[15]

2.3.4 Doping effect on Raman spectra

Doping has multiple effects on the phonons of graphene. Large charge concentrations are possible due to the 2D nature of graphene, allowing dopant to native atom ratios in the order of 10^5 to be achieved.[69] This level of charge density affects the carbon-carbon bond length in graphene, causing a general increase (decrease) the phonon frequency for positive (negative) doping.[70]

Graphene has a particularly strong E_{2g} electron-phonon coupling, as these phonons and electron-hole pairs can readily excite each other around the K point of the electron Brillouin zone (figure 2-2, 2-4).[71] This low energy coupling is strongest when:

$$E_F \leq \frac{\hbar\omega_G}{2}, \quad (2.20)$$

where ω_G is the frequency of the G peak. The coupling therefore causes the E_{2g} phonon lifetime to be significantly reduced when relation (2.20) is satisfied. This does not occur for the A_{1g} phonon as it does not easily couple to electrons due to the large phonon momentum blocking transitions.

At zero doping, there is also a Kohn anomaly at the Γ point of the phonon Brillouin zone (figure 2-10). This comes from the interaction between lattice and electron resonance, causing a reduction in phonon energy.[61,68] A Kohn anomaly causes the softening of phonon wavevectors that are resonant with an electron Fermi-surface wavevector. Increasing charge density, Fermi energy, removes this softening effect and shifts the phonon dispersion to higher energies at the Raman active point. For example, the downwards kink in the LO band at the phonon dispersion Γ point of figure 2-10, becomes flattened out and thus increasing the energy of the E_{2g} phonon.[61,68]

G peak position

The Kohn anomaly behaviour is the dominant doping effect on the G peak position. Figure 2-19 shows that the G peak energy increases with any doping increase across ordinary doping ranges (< ± 4x10^{13} cm^{-2}).[68,70,72,73] At electron concentrations above 4x10^{13} cm^{-2}, the bond shortening effects become equal to the Kohn anomaly shift effect, and further doping causes a decrease in phonon energy.

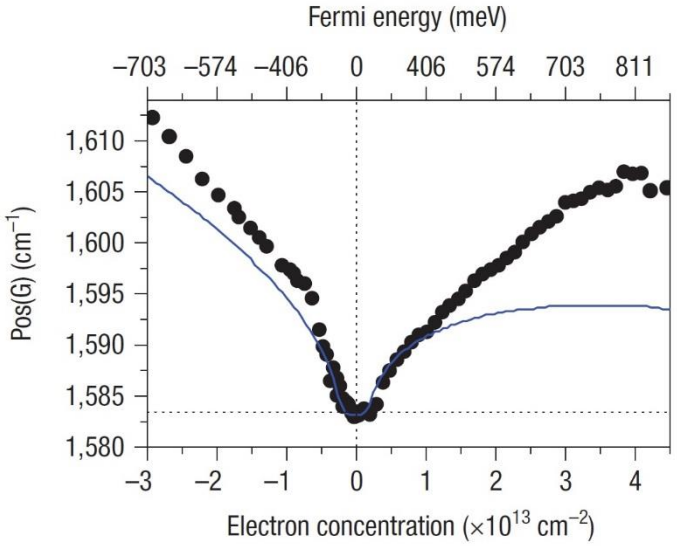

Figure 2-19: Graphene G peak position as a function of doping induced by an electrochemical top-gate. The blue line is the prediction from the combined Kohn anomaly and charge concentration effects on the lattice. The black circles are measurements. From Das et al.[70]

2D peak position

The A_{1g} phonon frequency is expected to be only affected by the bond length effects of charge doping.[68,69] However, it has been observed that the 2D peak position also increases with negative or positive doping (figure 2-20). However, the phenomenon is much weaker than the G peak shift, and is only dominant at charge concentrations below 2.4×10^{13} cm^{-1}.[70,72] This would be caused by a shift in the phonon dispersion around the K point in figure 2-10, which exhibits a strong frequency singularity. While the dispersion is not expected to shift at the K point, the magnitude of the singularity has the effect of magnifying even small fluctuations. This combined with the general bond shortening shift results in a more asymmetrical dependence of the 2D peak position on doping than for the G peak. This gives the 2D peak a more distinct frequency dependence between positive and negative charge carriers.

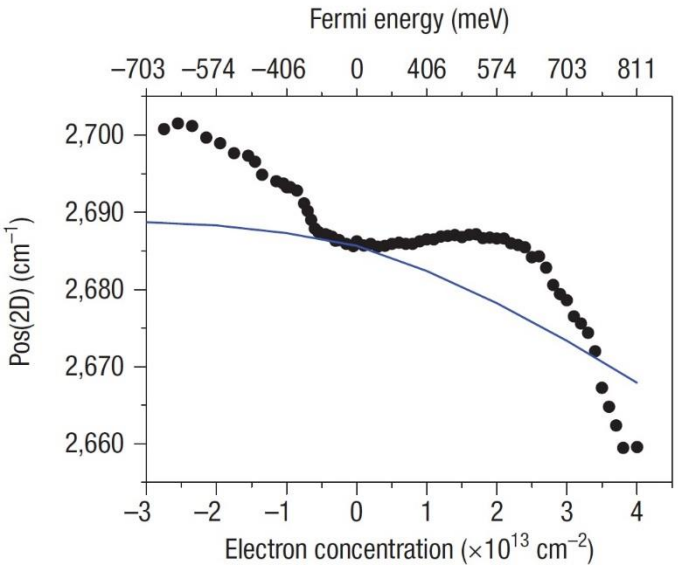

Figure 2-20: Graphene 2D peak position as a function of doping induced by an electrochemical top-gate. The Blue line is the prediction from charge concentration effects on the lattice. The black circles are measurements. From Das et al.[70]

G peak width

The strong electron-phonon coupling of the E_{2g} phonons shortens the lifetime of the quasi-particles. This in turn lowers the associated uncertainty in the phonon lifetime and by the Heisenberg uncertainty principle, increases the uncertainty in the phonon energy:[74]

$$\Delta l \Delta E \gtrapprox \frac{h}{2\pi}, \quad (2.21)$$

where l is particle lifetime and E is energy. This causes a lifetime broadening of the G peak at doping concentrations that satisfy relation (2.20). Charge doping therefore causes the FWHM of the G peak to fall to a constant value of 5-8 cm^{-1}, corresponding to weak/no electron-phonon coupling, for fermi energies greater than half the phonon energy.[69,70,72,73]

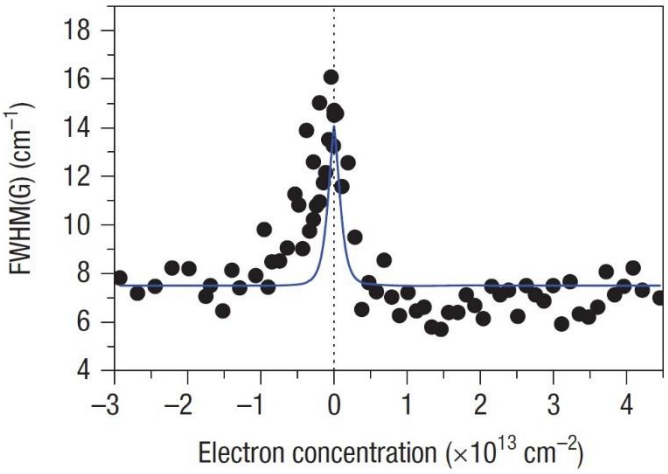

Figure 2-21: Graphene G peak FWHM as a function of doping induced by an electrochemical top-gate. The Blue line is the prediction from lifetime broadening. The black circles are measurements. From Das et al.[70]

As shown in figure 2-21, there is a large amount of variance within peak width results and from theoretical predictions. These fluctuations makes the G peak FWHM a poor indicator of specific doping value outside of a binary: low doping is >9 cm^{-1} and high doping is <8 cm^{-1} FWHM.[61,70]

Peak broadening with doping does not occur in the 2D peak as the A_{1g} phonon does not easily couple between electron dispersion bands which is required for strong coupling. Therefore the peak width is solely determined by phonon-phonon interaction lifetimes like the G peak under high doping.[3]

G and 2D Peak Ratio

The decrease in G peak FWHM with doping is also accompanied by an increase in the relative peak intensity compared to the 2D peak.[70,72,69,73,75] Therefore the ratio of the 2D and G peak areas or heights can also be used as a measure of doping concentration.[75]

2.3.5 Temperature-dependent phonon behaviour

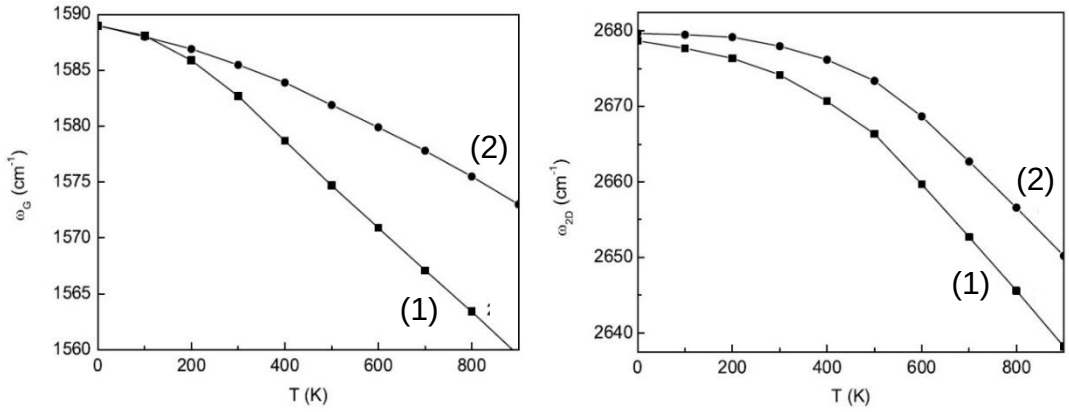

Figure 2-22: (1), The Raman peak position with temperature of the G (ω_G) and 2D (ω_{2D}) peaks caused by the phonon self-energy shift from the 3- and 4-phonon interactions. (2), the Raman peak positions from the combined phonon-phonon and electron-phonon contributions. Calculated by Apostolov et al.[76]

The phonon frequency in graphene also has a temperature dependence. The phonon-phonon interactions (self-energy) contribution to the phonon frequency changes with temperature for both the E_{2g} and A_{1g} phonons. The combined the frequency shift from the two lowest phonon-phonon interaction orders has been predicted to cause a decrease in phonon energy with increasing temperature in the range of 0–1000 K.[71,76] This shift combines with a contribution from electron-phonon interactions, which is expected to cause phonon hardening with temperature and counteract some of the shift from the phonon self-energy, as shown in figure 2-22.[76] The electron-phonon also causes a temperature dependence on the G peak linewidth, resulting in a decreasing FWHM in the range of 300–1000 K.[71]

2.3.6 Strain and doping separation

In order to measure either strain or doping in isolation using Raman, the other factors affecting peak shapes and positions would need to be externally controlled or separated. Using the difference in the shifts caused by strain and

doping in the G and 2D Raman peaks of graphene, it has been demonstrated that the strain and doping contributions to the combined peak position can be isolated. These differences are shown in figure 2-23, and the process used to determine this is described in section 5.1.3–5.1.4.[42,74]

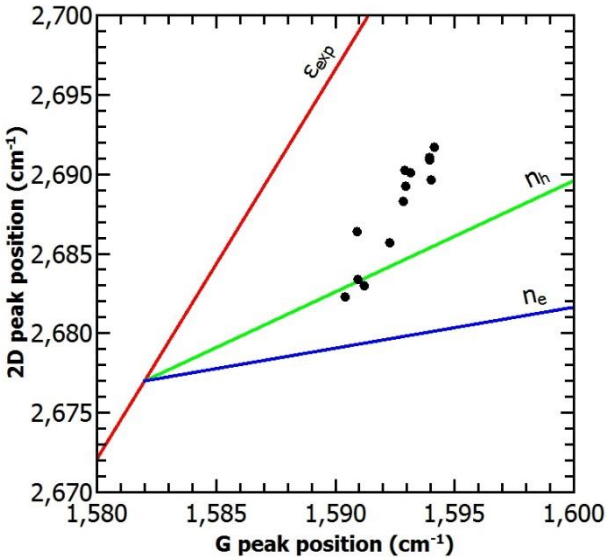

Figure 2-23: Example correlation of the 2D and G Raman peaks of graphene from section 5.1.3–5.1.4. The hydrostatic strain gradient is labelled ε_{exp} (red), the doping gradients are labelled n_h (green) and n_e (blue) for hole and electron doping respectively. The point where the lines intersect denotes the zero strain/doping position.

The method, developed by Lee *et al.*, correlates the 2D and G peaks in order to use the gradient $\frac{\Delta\omega_{2D}}{\Delta\omega_G}$, which is different depending on whether the peak correlation is a result of a hydrostatic strain $(\varepsilon_{xx} = \varepsilon_{yy})$ or charge doping. The strain and doping contributions to peak position can be separated out for any point in the correlation by taking the distance along the strain and doping gradients required to relate that point to the zero strain/doping position (figure 2-23, line intersect). This method is commonly used to optically identify strain in graphene systems.[45,47,50,77-80]

In order to account for the independent temperature dependence of phonon energy, it must be subtracted from the Raman peak positions before performing the peak correlation.[47,48] This is particularly necessary for measurements with varying temperatures as this would add a false dependence to the Raman peak correlation. The phonon shift would be interpreted as a false doping dependence as it shifts the G peak more than the 2D peak, similar to the n_h or n_e line in figure 2-23.

While the correlation method works well for hydrostatic strain systems, a more complex strain system will involve a combination of biaxial and shear strains. It has been demonstrated that the biaxial strain can be separated into hydrostatic and uniaxial components.[77] The uniaxial and shear strain components can be independently identified by the magnitude of the peak splitting of the G or 2D peaks. The hydrostatic component is then the average position of the two split peaks (G^+, G^- and $2D^+$, $2D^-$), which is then used in the correlation method as previous to determine the strain.

2.4 Hexagonal boron nitride

Boron nitride can form as a crystal lattice of a similar structure to graphite: as a series of stacked 2D crystal layers. An individual sheet of h-BN exhibits the same hexagonal lattice structure as graphene and has a similar lattice constant: $|\mathbf{R}_{graphene}| \approx 2.460$ Å and $|\mathbf{R}_{h\text{-}BN}| \approx 2.505$ Å of figure 2-1.[81] This means the structural properties of h-BN are comparable to that of other 2D materials: weak inter-layer bonding and flexible membrane properties at a low number of layers.

Unlike the graphene lattice from figure 2-1, the A and B sub-lattices of h-BN are not identical but each sub-lattice is either all boron or all nitrogen. Therefore, there

is a difference in the on-site energy of electrons between the boron and nitrogen sites, breaking the inversion symmetry of the lattice.[82] When creating the electron Hamiltonian, the difference in on-site energy gives rise to diagonal terms in h-BNs Hamiltonian, giving the h-BN equivalent to equation (2.2):

$$\begin{pmatrix} 0 & \varphi_A^* H \varphi_B \\ \varphi_B^* H \varphi_A & 0 \end{pmatrix} = \begin{pmatrix} \epsilon_B & t^* \sum_i e^{-i\boldsymbol{k}.\boldsymbol{R_i}} \\ t \sum_i e^{i\boldsymbol{k}.\boldsymbol{R_i}} & \epsilon_N \end{pmatrix}, \quad (2.23)$$

where ϵ_B and ϵ_N refer to the boron and nitrogen site energies respectively. Alternatively, setting one of the on-site energies to a zero reference leaves the other as $\Delta\epsilon_{BN}$ achieves the same dispersion. As with two or more graphene layers, this diagonal $\Delta\epsilon_{BN}$ term determines the band gap of h-BN (~6 eV) when solving for $\epsilon(k)$.

This significant bandgap and similar physical structure is why h-BN has seen increasing use as an insulating substrate for graphene.[83] The chemical stability and structural similarity between the two substances causes a significantly lower inherent doping and reduced resistive effects in the graphene compared to conventional SiO_2 dielectric surfaces. While the band gap of h-BN is not as large as SiO_2 (~9 eV), it is compensated by allowing closer gate proximity in h-BN/graphene devices.[84]

2.5 Atomic force microscopy

AFM allows for the measurement of both features below the diffraction limit of visible light, that limits the resolution of optical microscopy, and the topography of surface features.[85] This is achieved by a physical probe consisting of a sharpened point, typically with a tip radius in the order of 10 nm, mounted on a

cantilever, depicted in figure 2-24. A surface is then measured by bringing this tip into physical contact with the surface in either “contact” or “tapping” mode.

In contact mode AFM, the probe is dragged directly across a surface while mounted on a stage. The repulsive interaction with the surface causes the cantilever to be deflected. A laser is reflected off the top face of the probe and the surface height is calculated either from the induced angular laser deflection, or from the stage translation required to counteract the deflection. Contact mode is not always practical as water vapour, condensed on a surface, can create surface tension forces at the probe tip in ambient conditions. Plastic deformation of the cantilever is also possible if the scanning tip encounters too large a step in surface level.

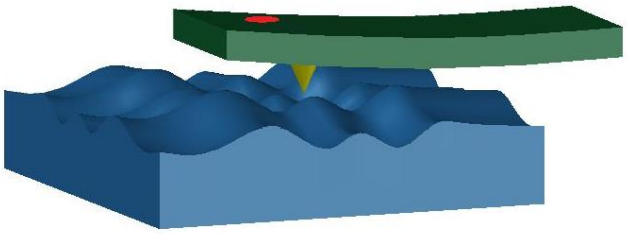

Figure 2-24: Representation of a surface (blue) being probed by an AFM tip (yellow) mounted on a cantilever (green). The cantilever deflection is measured by the change in reflection of a laser spot (red).

Tapping mode AFM is used to avoid the erroneous forces acting encountered in contact mode.[86] Oscillating the surface probe avoids constant surface contact and the issues it creates, effectively “tapping” the surface to make measurements. The surface height is calculated from its effect on the cantilever oscillation amplitude, which is maximised by oscillating the probe near its resonant frequency. Surface features are then inferred by this change in the oscillation damping effect with surface height.

2.6 Scanning electron microscopy

SEM is also a means to improve resolution below the diffraction limit of light. In this case, electrons are used for imaging in the place of the photons in an optical microscope, and refractive lenses are replaced by shaped magnetic fields.[87] The initial high-energy electrons interact with a substrate, ionising lower energy secondary electrons. The secondary electrons are accelerated by a reverse potential to a detector to create an image of the surface. In principle, the theoretical resolution of the image is determined by the primary electron De Broglie wavelength (λ_B) and is therefore dependent on momentum (p):[88]

$$\lambda_B = \frac{h}{p}. \quad (2.24)$$

In practice, the secondary electrons can scatter multiple times before leaving the surface, giving a resolution in the order of 50 nm. An additional benefit of SEM is the ability to perform energy dispersive (X-ray) spectroscopy or EDS.[87] The typical primary electron acceleration potential of 1-50 kV is great enough to ionise electrons in the deep 1s atomic orbitals, or K shell for X-ray spectroscopy (figure 2-25). This allows for X-ray spectroscopic fingerprint identification of atomic elements as these electron orbitals close to the nucleus are heavily isolated from external factors and are energetically invariant. Additionally, if the interaction cross-section of each element is known, the ratio of atomic elements can also be determined.[87]

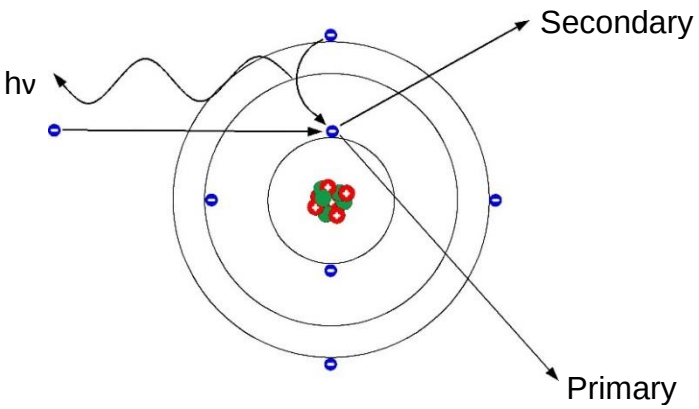

Figure 2-25: X-ray emission (hv) from a graphene carbon atom caused by the ionisation of an inner orbital electron by an incident, high-energy electron.

There are difficulties in performing EDS on lighter elements, atomic numbers from 4 – 11. The X-Ray energy has a greater dependence on bonding pattern as this changes the amount of screening provided by higher orbitals. The ionisation interaction cross-section of inner orbitals determines the x-ray fingerprint intensity, which has an inverse-square dependence on ionisation energy. Therefore the lightest elements have the largest cross-sections which will also shift depending on atomic bonding. This causes these elements to be susceptible to inaccuracies in relative number or mass ratio measurements. Likewise, the lack of inter-orbital transitions means hydrogen, helium and lithium have no EDS signal.

2.7 Conclusion

This chapter has detailed the means by which strain effects on graphene have been previously measured using spectroscopy. The various means by which strain can be induced are covered, and how, through device or substrate design, this strain may be intentionally modified. It is clear that Raman spectroscopy is an exceptional method for non-invasively measuring graphene and multilayers in

addition to experimentally induced strain and doping. The motivation for thermal strain is outlined due to the parity between it and transport device measurements. The possibility of multiple effects being induced in the same experiment is considered and methods of isolating these have been addressed.

3 Predictions

This chapter addresses the expected results of the strain and doping measurements described in chapter 2, based on the experimental methods used, which are discussed in chapter 4. This includes the effects of the surface topography of the chosen substrates and how metal contacts may enhance the pinning effect on graphene. The strain profile with temperature is then predicted for the ideal-contact thermal expansion scenario, for comparison to the measured results. The results expected from multi-layered graphene and h-BN substrate graphene were then speculated on, in comparison to single layer graphene on silicon substrates.

3.1 Monolayer graphene on Si/SiO_2

3.1.1 Surface roughness

SiO_2 has an amorphous atomic structure which gives it a rough surface at nanometre scales. Oxidised silicon substrates, as used in this study, have been shown to have roughness features in the range of 0.5 nm to 1 nm in height across length scales between 25 nm and 50 nm.[83,89,91] When graphene or other flat 2D materials are transferred to these surfaces, it will attempt to conform to the new topography. The deformation will induce nanometre-scale strain regions in the graphene and cause semi-suspended regions between larger roughness features, shown in figure 3-1 (a). These topological fluctuations randomise the strength of the contact forces between the graphene and SiO_2 which may change the expected thermal expansion strains. Either slipping/crumpling of graphene

(figure 3-1 (b) and (c)) or strain-free thermal expansion in suspended regions (figure 3-1 (a)) will cause a different strain to that predicted by a thermal expansion mismatch.

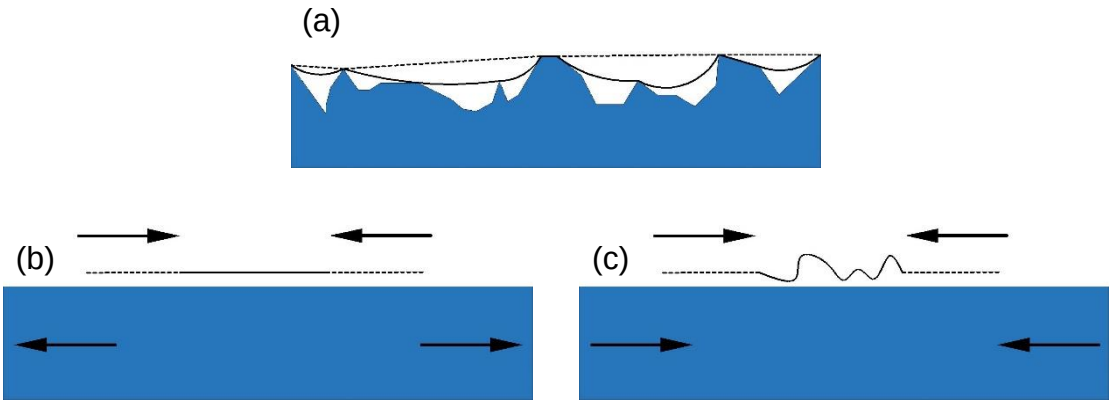

Figure 3-1: (a) Graphene suspended between SiO_2 surface roughness features (dashed line). When the graphene expands relative to the substrate, it can do so without inducing strain by filling in the surface roughness (solid line). (b) Graphene slipping to reduce strain on a substrate that is expanding in comparison to the graphene. (c) Graphene crumpling to reduce strain on a substrate that is contracting in comparison to the graphene.

The presence of nanometre surface roughness, or variations in strain field would be difficult to detect optically because roughness feature size is smaller than resolution. However, a distribution of surface induced strains may manifest as a broadening of both the G and 2D graphene Raman peaks when compared to suspended graphene to eliminate substrate effects. The existence of suspended regions would be detectable if it causes a delay in Raman shift with applied strain, indicating the graphene is freely relaxing.

3.1.2 Metal contacts

Electronic graphene devices on Si/SiO_2 require the addition of source/drain contacts, top/back gates, and/or cross-current contacts. Electronic measurements are also commonly performed at low temperatures, using nitrogen or helium cryogenics, for thermal noise reduction, allowing easier measurement

of quantum phenomena. This will necessarily cause thermal strains in electronic device measurements. In addition to the substrate TEC mismatch strain, the effect these structures have on graphene devices must be understood. In addition to metal deposition strains, the contacts may prevent the slipping or crumpling of graphene seen in thermally strained graphene (section 2.2.3), enhancing the expected strain.[46,48] Simple uniaxial and biaxial strains do not create the coherent pseudo-electromagnetic effects discussed in section 2.2, however, unintended contact effects on strain may give rise to localised potential fields.[88] Understanding these effects will allow device designers to avoid creating undesired electronic effects.

Three types of contacting are investigated in this study: isolated and uncontacted graphene; two-point contacted graphene; and two-point nailed-contact graphene in which the metal “nails” go through the graphene and into the substrate.

Uncontacted

Without contacts, the Van der Waals forces from surface contact is the only force on graphene, inducing the expansion mismatch strain and preventing slipping or crumpling (figure 3-2). As mentioned in section 2.2.3, flexible substrate and thermal expansion strain measurements have observed that when the elastic deformation potential becomes greater than the Van der Waals surface attraction, graphene will slip or crumple. The relaxation results in a lower resultant strain than predicted by the TEC mismatch.[46,48]

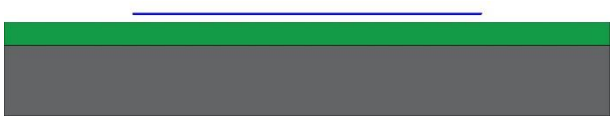

Figure 3-2: Isolated graphene flake (blue) on a silicon substrate (grey) with an oxide layer (green).

Contacted

Electronic contacts are created by depositing metals onto graphene samples, covering a region on top of the graphene (figure 3-3). This will double the surface contact area and hence increase the Van der Waals force from the regions of graphene directly under the metal. The extra contact force may prevent the slipping or crumpling of graphene at high strains. The contacts may also physically block the expansion of graphene relative to the substrate. With decreasing temperature, the enhanced pinning in a single direction would cause an asymmetrical biaxial strain, observable as a broadening or splitting of the Raman G peak with strain.

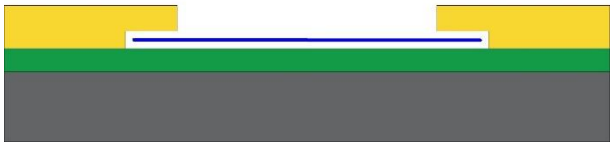

Figure 3-3: Contacted graphene flake (blue) with metal contacts (yellow) on a silicon substrate (grey) with an oxide layer (green).

Metal deposition strains, discussed in section 2.2.3, are expected to be induced by this sample geometry. The range of these strains beyond the contact edge (<1 μm) are much shorter than the total sample length (>8 μm) and do not contribute to the Raman strain signal when measuring at the sample centre.[10,11,12] Edge-only contacting is also possible with graphene to avoid the resistive effects of transferring charge out of the graphene plane. These contacts are not investigated due to the reduced clamping effects.

Nailed contacts

A second contacting style was investigated as a means to enhance graphene: by etching a series of holes into a graphene flake and into the substrate below,

contacts can be fashioned into “nails” (figure 3-4). In addition to the predicted pinning and strain effects of top contacts which should still be present, the nails would also prevent the slipping of graphene when it contracts relative to the substrate. These structures are used in fully suspended graphene with no substrate, using the nails for sample stability.[49]

Figure 3-4: Nailed graphene flake (blue) with metal contacts (yellow) on a silicon substrate (grey) with an oxide layer (green).

In addition to the metal deposition strain, the nail-configuration contacts will induce localised strains around the nails when the sample-substrate expansion strain overcomes the Van der Waals force limit. The resultant strain variation will be dependent on the nail separation, with a closer spacing of nails creating a more uniform strain pattern, and distance from the contact nails. Such strain distributions would be discernible through either a Raman-shift map of strained graphene close to the contact regions, or as an increase in both G and 2D Raman peak width with increasing strain.

The aim of this study is to investigate how the additional pinning of contacts such as these change the strain effects in graphene devices at cryogenic helium temperatures, similar to transport measurements. Additionally, if no graphene slipping or crumpling is achieved, a measure of the TEC of graphene is also possible. This allows for a measure of the TEC of graphene at a lower temperature than any other measurement technique (<30 K) and significantly lower than previous thermal expansion strain TEC measures (<200 K).[16,17,48]

3.1.3 Thermal expansion mismatch

Graphene on a Si/SiO_2 substrates has been shown to experience a change in strain with changing temperatures, from the difference in TEC between the graphene and substrate.[17,19,46-48] For silicon substrate oxide layers that are sufficiently thin (295 nm), it can be assumed that the resultant expansion is dominated by the bulk silicon thermal expansion coefficient (TEC).[17,47,48] Given that thermal expansion is isotropic, the strain induced in the graphene is hydrostatic and does not cause Raman peak splitting.

Therefore, the expected strain can be calculated from the difference between the TECs of silicon and graphene. As with the substrate oxide layer, it is assumed that the silicon TEC determines the expansion of graphene as long as the graphene remains in contact with the substrate. The thickness ratio between the substrate and graphene of ~10^6 causes the graphene to be deformed over the substrate, despite the Young's modulus ratio of graphene to silicon being ~5. Therefore, the expected strain of graphene on Si/SiO_2 can be resolved by equating the strain to the thermal expansion:[40]

$$\varepsilon = \frac{\Delta L}{L}, \quad (3.1)$$

$$\varepsilon \frac{1}{\Delta T} = \frac{\Delta L}{L}\frac{1}{\Delta T} = \frac{1}{L}\frac{\Delta L}{\Delta T} = \alpha, \quad (3.2)$$

where T is the temperature, α is the TEC, ε is the strain and L is the length dimension of the graphene. As the graphene strain is imposed by the substrate, the resultant TEC of the graphene is defined as the thermal expansion of the silicon substrate, minus the suppressed thermal expansion of the graphene:[48]

$$\varepsilon = \int_{T_0}^{T} \left(\alpha_{Si} - \alpha_{graphene}\right) \Delta T, \quad (3.3)$$

where T_0 is the starting temperature (room temperature). In order to calculate an expected strain dependence of graphene on Si/SiO_2, an approximation of equation (3.3) was calculated.[20,93] The thermal expansion difference, $\alpha_{Si} - \alpha_{graphene}$ from figure 3-5, was fitted with a first order, second order and sixth order polynomial, with the condition that the TEC is zero at zero Kelvin, to determine the level of accuracy of fit that is required to best approximate the integral described in equation (3.3). These fits are also displayed in figure 3-5.

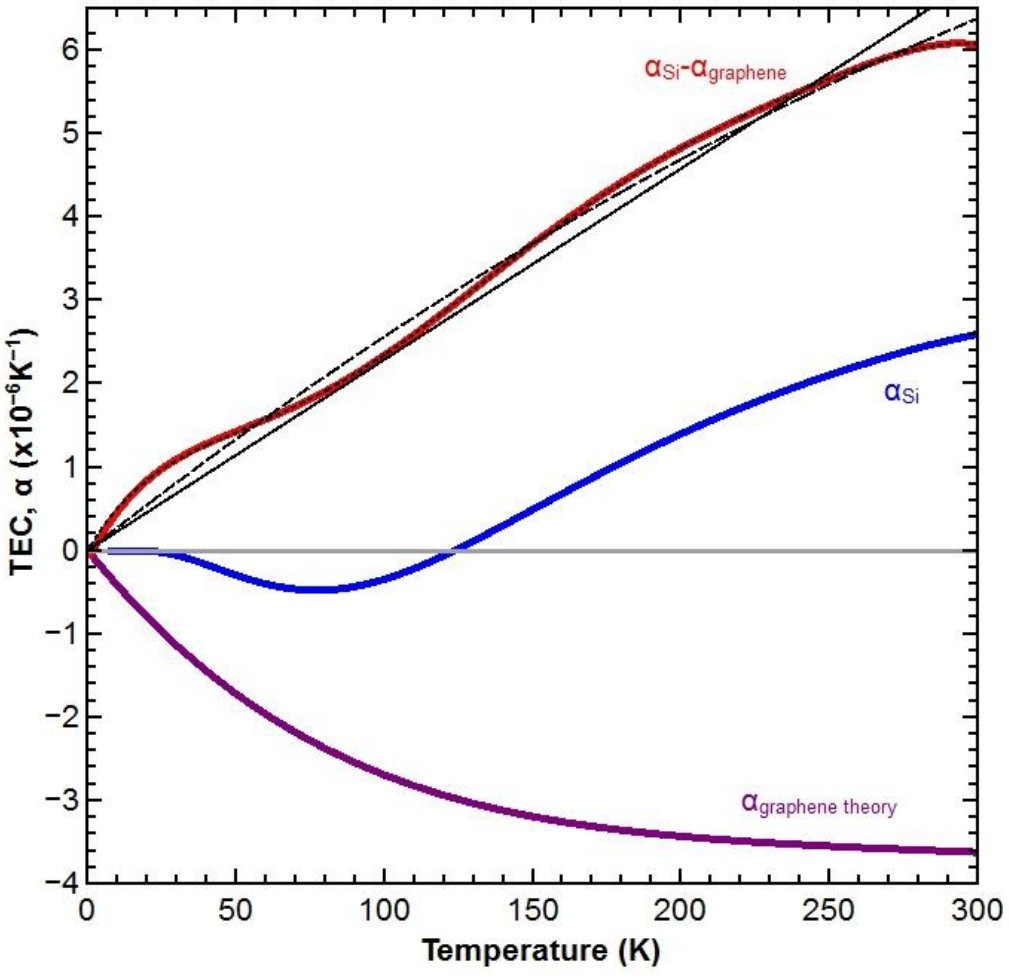

Figure 3-5: Theoretical TEC of graphene, $\alpha_{graphene\ theory}$ (purple) as predicted by Mounet et al.;[20] measured TEC of silicon $\alpha_{Si\ exp.}$ (blue) measured by Middelmann et al.;[93] and the difference between the two (red). The first order fit is shown as a solid line, the second order fit a dashed line, and the sixth order fit a dotted line. The zero TEC point is marked with a grey line.

The differences between the integrals of these three fits are shown in figure 3-6, which shows no significant change in expected strain with greater fitting algorithm order as the first order component of all three fits was dominant. Therefore, the first order fit $(y = mx)$ of the TEC was used as an acceptable approximation. The resultant thermal expansion mismatch strain predicts a steep strain gradient starting at room temperature which decreases with a reduction in temperature, caused by the convergence of the graphene and silicon TECs when approaching zero Kelvin. The strain from the first order fit takes the form:

$$\varepsilon = \frac{m}{2}T^2, \quad (3.4)$$

where m is the gradient of the straight-line fit in figure 3-5 (dashed line).

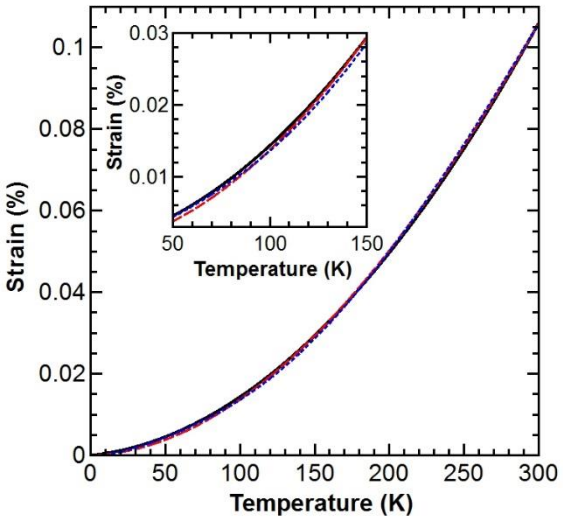

Figure 3-6: Comparison of the resultant strain of the three different order fits of the α_{Si}-$\alpha_{graphene}$ line in figure 3-5. Black line: first order fit, red dashed line: second order fit, blue dotted line: sixth order fit.

3.2 Two and three layer graphene

The negative TEC of graphene is caused by the occurrence of out-of-plane phonon vibrational modes.[20] Therefore, any changes in these phonon energies

caused by stacking graphene layers will affect the resultant in-plane TEC of the stack. The Grüneisen parameter of two-layer graphene is predicted to be less negative than for single layer graphene.[94] This reduction in the relation between changing phonon energy and lattice volume is expected to result in multilayer graphene having a less negative TEC than the single layer case. The two- and three-layer graphene TEC is therefore expected to have values somewhere between those for single layer graphene and graphite.[94] Graphite has a negative TEC over the temperature range studied, but with a significantly lower magnitude.[20] This is brought about by the stacked graphene inhibiting the out of plane vibration modes of the individual layers. A direct measure of multi-layered graphene TEC has not yet been performed to confirm this.

Doping shifts and effects have been shown to behave similarly for single- and multi-layered graphene. However, due to the 2D definition of doping concentration, the dopants are distributed between the layers and the magnitude of the Raman doping shift is thus divided by the number of layers.[95]

3.3 Graphene with h-BN substrate

As a 2D material comparable to graphene, hexagonal boron nitride (h-BN) offers a substrate with a matching structure to graphene within 1.7%.[96] An ultra-flat substrate with a matching smoothness to graphene could have significantly enhanced surface contact effects compared to a rougher SiO_2 surface. As well as increasing the Van der Waals forces and pinning effects, the closely matching lattice structure may interfere with the graphene transverse phonon modes. In comparison, semi-conforming graphene on an uneven SiO_2 surface easily allows the graphene phonons to freely oscillate perpendicular to the surface plane.

Therefore, a sufficiently flat substrate, matching graphene, could shift the energy of or entirely suppress these phonons by being physically blocked. This blocking of transverse phonons would change the TEC of graphene, reducing or removing the negative contribution from these phonons.

The unit cell similarity between graphene and h-BN causes lattice matching between the two, usually by graphene conforming to the lattice parameter of a bulk h-BN substrate. The resultant Moiré pattern distributes this strain in large, tensile-strained regions with lattice matching and boundaries between the matched regions with a compensating compressive strain.[96] These nanometre-scale strain patterns should result in a broader Raman G and 2D peak in comparison to suspended graphene flakes.

The roughness of an h-BN surface is itself partially dependent on the underlying substrate roughness. h-BN has an attenuating effect with thickness on this underlying surface roughness.[83] For a graphene/h-BN device built on a Si/SiO_2 substrate, the roughness of the h-BN surface was shown to modify the roughness of the underlying substrate by a factor of $\frac{1}{r}$, where

$$r = 1 + 0.129h, \quad (3.5)$$

where h is the height of h-BN thickness in nm. This would ideally require the selection of h-BN crystals of at least twenty layers to achieve a smoothing of an underlying silicon substrate by a factor of two.

3.4 Conclusion

The manner in which samples are prepared and fabricated could have a significant effect on the strain results that are expected. These variations are difficult to measure as the predicted effects are similar to those caused by other known phenomena. For example: G peak broadening is caused by both inhomogeneous strain and lower doping concentrations, and both may change between samples if substrate-induced strain and doping are inconsistent.

The approximation of the expected strain caused by the TEC difference between the graphene and silicon substrate is used for comparison with strain measurements using Raman spectroscopy in chapter 5. This prediction ignores the possibility of slipping, crumpling or surface roughness effects and therefore should be the theoretical maximum strain over this temperature range, as these effects serve to reduce the resultant graphene strain.

4 Sample manufacture and experimental techniques

This chapter covers the methods by which the graphene samples used in this study were manufactured. The chapter begins with describing the manufacture of single-crystal graphene flakes and the methods by which the flakes were shaped and made into contacted devices. The design criteria used to ensure standardised and directly comparable devices is also covered.

The experimental techniques are covered in the second half of this chapter. This details the methods used for temperature dependent Raman measurements of single and multi-layer samples. This consists of the cryostat cooling, excitation laser, and spectrometer measurement systems. The methods used to calibrate and improve the resultant detector signal with these systems is then elaborated upon.

4.1 Mechanical exfoliation

The graphene samples used in this study were manufactured by mechanical exfoliation as it produces large quality single-crystal flakes with length scales of 1-10 μm. These samples sizes are suitable for optical microscopy while avoiding signals from flake and contact edge effects. Using bulk crystals of highly ordered pyrolytic graphite (HOPG) as the exfoliation material allowed for large, single-domain graphene flakes to be cleaved. Two sheets of low-tack cleanroom tape with an acrylic adhesive were used to exfoliate a fragment from a larger HOPG crystal for

10-20 cycles to disperse the graphite to a surface area similar to that of the final substrate. The substrate is pre-heated to 90 °C before the graphite-tape is pressed onto the surface to transfer the material to the substrate surface. The substrates used were a silicon (Si) base of 0.5 mm thickness with a 295 nm thick oxide layer (SiO_2) on the top surface. The Si base was n-doped to a concentration of 4-7x10^{19} cm^{-3}. Prior to graphene transfer, the oxide surface is pre-treated with an oxygen-argon (O_2:Ar) plasma which removed surface contaminants without etching the SiO_2 layer. This prevents the trapping of contaminants between the graphene and substrate, which dopes the graphene and affects the surface contact forces.

4.2 Graphene identification

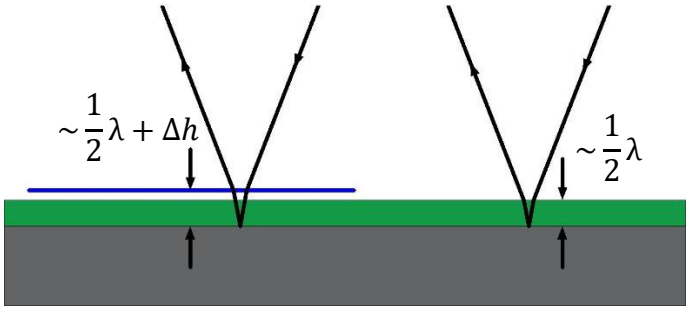

Figure 4-1: Thickness difference between graphene (Δh) plus oxide layer (left) and oxide layer (right) in terms of the constructive interference wavelength, λ.

Graphene flakes were searched for manually by microscope, however the thickness of graphene causes it to present a very low optical contrast. The reflective substrate and transparent oxide layer creates thin film interference at visible wavelengths, allowing for easier graphene identification by the difference it causes in the constructive interference wavelength, shown in figure 4-1. This interference

enhancement boosts the apparent contrast of individual graphene layers to 5-6%. Graphene identification is performed either by contrast or colour variation. Contrast variation uses a monochromatic green light (560-520 nm) to enhance the contrast difference of graphene which has less constructive interference at this wavelength than the bare substrate. Colour variation uses broadband illumination to observe the colour difference caused by the change in the constructive interference wavelength.[31] Identified graphene and multilayered graphene were then independently confirmed and classified by their Raman fingerprint, as shown in figures 2-13, 2-15, and 2-16.

4.3 Graphene and substrate etching

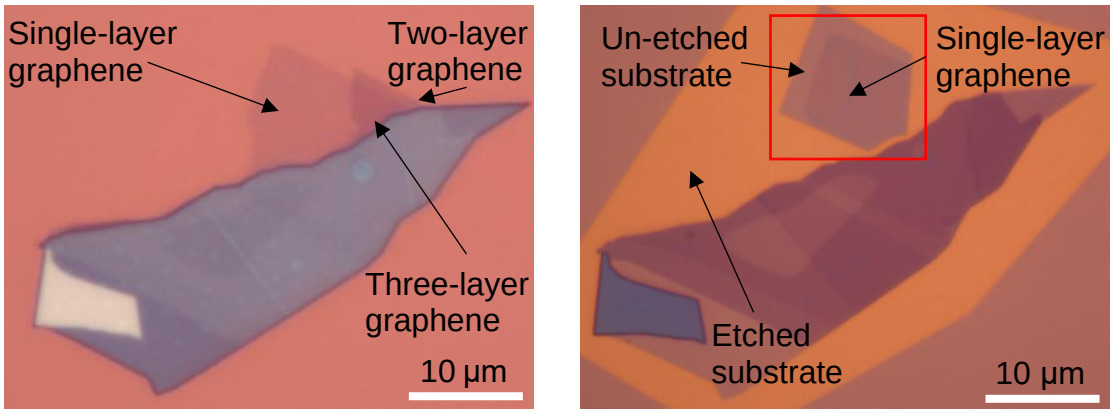

Figure 4-2: (left) Graphene flake as exfoliated. (right) Graphene flake (red box) isolated from multilayers and bulk graphite, and re-shaped by CHF_3 plasma etching. The lighter substrate regions show where the oxide layer thickness has been reduced by etching.

To avoid unintended pinning effects, the identified graphene was isolated from the surrounding graphite. Reactive ion etching (RIE) was used to isolate graphene flakes, form the flakes into regular rectangular shapes, and to create “nail holes” for the nailed contact design type. The before and after result of this is demonstrated in

figure 4-2. A trifluoromethane (CHF_3) gas mix of CHF_3:O_2:Ar was used to create a high-fluoride reactive plasma capable of etching both graphite and SiO_2, allowing for the simultaneous etching of the sample shape and nail holes in the same manufacturing step. To selectively etch sample areas, a 350 nm polymethyl methacrylate (PMMA) etch mask was created using electron beam lithography, chosen for its ability to achieve high resolution writing.

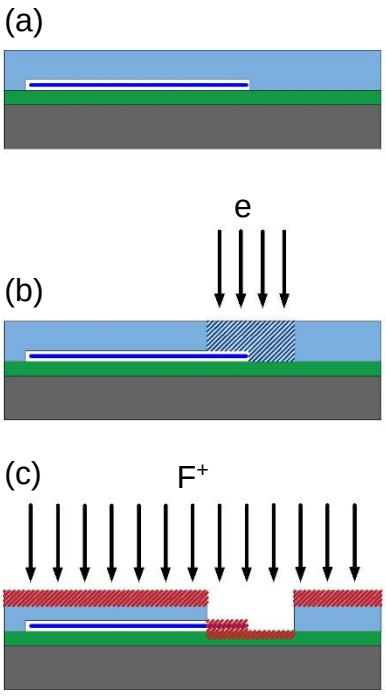

Figure 4-3: (a) PMMA polymer coating (light blue) of a graphene flake (dark blue) and Si (grey) substrate with an SiO2 oxide layer (green). (b) Electron beam lithography of selected PMMA regions (blue hatching). (c) RIE etching with high-fluorine gas (red hatching).

The PMMA was deposited in solution and spin-coated before drying to ensure an even thickness. An electron beam writing pattern was created in 2D modelling software. The designs were scaled and positioned using optical images of the samples and calibration markers on the substrate. The electron beam was accelerated with an 80 kV potential at a current of ~10 nA in order to de-polymerize

the positive-resist PMMA through its entire thickness. The beam was focused on the desired regions using magnetic lenses as in scanning electron microscopy (SEM). These exposed PMMA regions are then removed with a selective solvent, leaving the un-exposed PMMA as a sacrificial layer for the etching process. After etching, the remaining PMMA is removed with a stronger solvent. The described etch process is depicted in figure 4-3.

The reactivity of the fluorine ions from the CHF_3 gas was observed to induce a significant heat buildup at the sample surface causing cross-linking of the PMMA polymer in the sacrificial layer. This led to sample contamination by insoluble polymer films, covering the sample area (figure 4-4). The insoluble films could be avoided by lowering reactive ion etch rate. This was achieved both by lowering the power of the ionising radio frequency (RF) field, and by lowering the amount of CHF_3 either by lowering the total chamber pressure or gas ratio. A SiO_2 etch rate of 4 nm over 30 seconds, with 5 minute stabilization periods was used to etch 20 nm nail holes without insoluble polymer buildups.

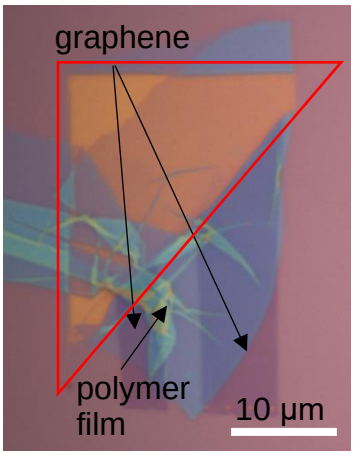

Figure 4-4: Insoluble PMMA polymer film, randomly folded during the removal of PMMA after etching. The films were created by RIE crosslinking during the etching process and form along the edges of etched regions (red).

4.4 Device designs

4.4.1 Contact designs

A two-point contact design was employed to investigate contact pinning effects, due to the relative simplicity of manufacture across a range of graphene flake geometries and sizes from 6 μm to 20 μm. To maintain parity with equivalent transport devices, gold (Au) contacts were used. Chosen for its high conductivity, the chemical inertness of gold makes it additionally desirable for long-lasting devices. However, to reliably adhere to SiO_2, gold requires a wetting layer. For this study, chromium (Cr) was used. The contacts were positioned along opposite sides of the graphene flakes, with parallel edges. The contact edges were also aligned to be as perpendicular to the exposed edges of the graphene flakes as possible.

4.4.2 Si substrates

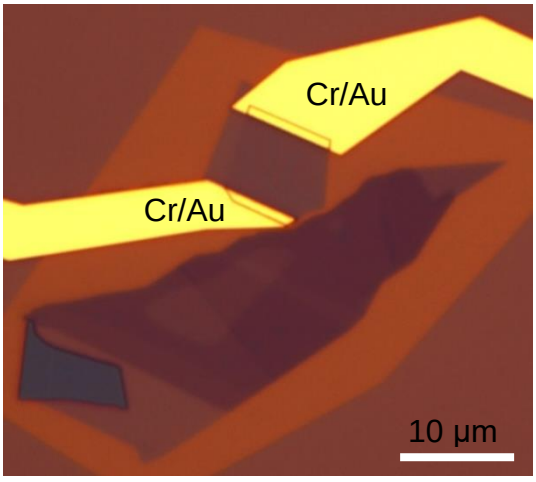

Figure 4-5: Completed device of the graphene flake from figure 4-2 in the "contacted" design style. The 20 nm layer of gold on top of the graphene is visible from the outline of the height step it causes.

Three device styles were created for graphene flakes on SiO_2 surfaced substrates: uncontacted, contacted, and nail-contacted devices. Uncontacted graphene samples were made from flakes of at least 6 μm in diameter and were created by simply isolating the graphene flake from the surrounding material as shown in figure 4-2.

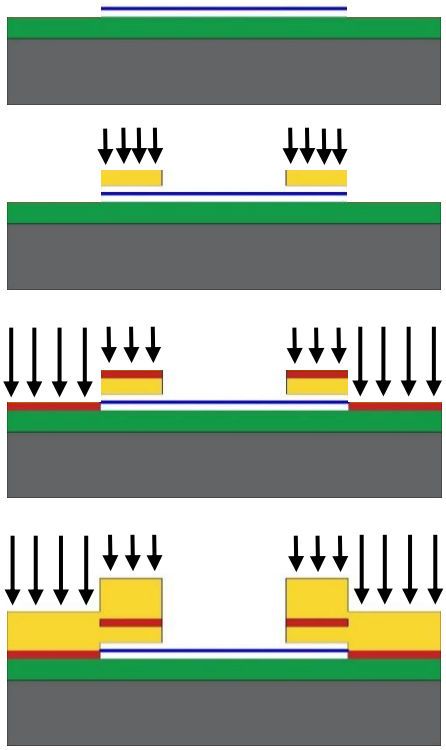

Figure 4-6: Cr/Au contact schematic for Si/SiO_2 devices. Au contacts (yellow) are deposited on top of the graphene (blue) and SiO_2 (green), with a chromium (red) wetting layer. The Si substrate is grey.

As with uncontacted samples, contacted and nail-contacted graphene are at first also isolated from the surrounding material by etching. The graphene contacts designs allowed for at least 1 μm of overlap between the contact and graphene, and a 6 μm gap between two contact edges (figure 4-5). In order to maintain an Au-graphene interface, the contact metal was deposited in two stages: first the deposition of 20 nm of gold on top of the contact-graphene overlap region, second

the deposition of 5 nm chromium and 100 nm of gold over the entire area of the contact design (figure 4-6). This ensures the direct Au-graphene top-contact while allowing for the adhesive chromium wetting layer for the Au-SiO_2 interface. This also maintains parity with the metal layering for the nailed contact samples.

The nailed contact samples, discussed in section 3.1.2, are designed and fabricated in a similar manner to the contacted samples, but with a difference in the substrate etching stage. In addition to isolating the flake, a series of round holes are also etched through the graphene and substrate, 0.3 μm diameter with a 2 μm spacing, under the gold-graphene region, parallel to the contact edge. As per section 4.3, these holes were 20 nm deep and were filled in with gold during the first deposition stage of thermal evaporation.

4.4.3 h-BN devices

The process of stacking graphene on hexagonal boron nitride (h-BN) resulted in some differences in contact design and manufacture. h-BN flakes were manufactured by mechanical exfoliation onto a Si/SiO_2 substrate using the same process as graphene, but with fewer exfoliation cycles (5-10). In order to be stacked, the exfoliated graphene was deposited on top of a substrate with a polymer stack of polyvinyl alcohol (PVA) and PMMA instead of directly onto a Si/SiO_2 substrate. Graphene flakes are then lifted off the substrate by dissolving the PVA layer with drop-casted water, leaving the graphene on a free-floating PMMA film. The film and was then lifted by the edges, inverted, and the graphene and h-BN flake were aligned before stamping the film on to the h-BN substrate. The PMMA film was then used as the deposition mask for a set of 5 nm chromium and 100 nm gold contacts directly

on to the graphene and substrate. This is done to pin the graphene to the substrate prior to the PMMA film removal to prevent the loss of the graphene flake (figure 4-7). This requirement means that graphene on h-BN substrates were not made with the uncontacted and nailed configuration, and are only directly comparable to contacted graphene on SiO_2 substrates.

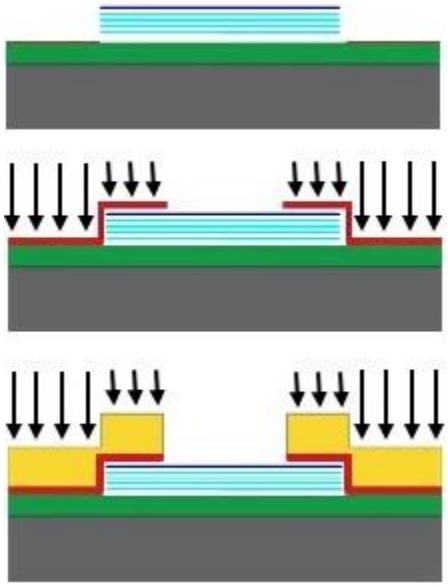

Figure 4-7: Cr/Au contact schematic for h-BN substrate devices. In this case, the chromium (red) wetting layer is deposited directly onto the graphene (blue) and SiO_2 (green). The Au (yellow) is then deposited in a single stage on top. The graphene sits on a h-BN stack (cyan), and the Si substrate is grey.

4.5 Metal deposition

Both metal contacts were deposited using thermal evaporation. As with etching, the metal contact geometry was again designed and aligned with 2D modelling software, and the mask written by electron beam lithography. This time, the 350 nm PMMA film served as a deposition mask, allowing metal to be deposited up to the polymer thickness. Masked samples were mounted above a receptacle holding the deposition material. The gold and chromium were then evaporated in a high vacuum

chamber (10^{-5}–10^{-6} mbar) using an electrical heating filament. The high vacuum environment allows the metals to evaporate at significantly lower temperatures, for example, the boiling point of gold became ~900 K. Additionally, the high vacuum environment increases the mean free path of gaseous atoms to a length larger than that of the chamber dimensions, creating a ballistic trajectory between the material receptacles and sample surface. This allows the evaporated metal to deposits evenly on the sample surface. The deposition thickness is measured by a piezoelectric resonator also in the path of the deposition.

4.6 Cryostat

4.6.1 Properties

A cryostat with a short distance between the sample and viewing window was required in order to perform microscopy, therefore an Oxford Instruments MicrostatHe helium flow cryostat was used. The cold finger configuration allows the cryostat external viewing window to be closer to the sample compared to a cryostat where the cryogen is in contact with the sample. The sample-window distance is reduced by only requiring the insulating vacuum layer between the sample and the outer wall, also removing the need for the window to be impervious to liquid helium. For the cryostat used in these experiments, the distance between the front and back windows of the sample chamber was 22 mm. The distance was short enough to allow for optical microscopy using a long working distance lens, with a 50 times magnification factor and 17 mm focal length. The lens was used as the objective lens for both the excitation laser and emitted Raman signal. The laser itself was

aimed onto the objective and sample using a mirror small enough to prevent blocking of the majority of the Raman signal in its path from the sample to the spectrometer.

Cooling was achieved using a continuous flow of liquid helium to the copper cold finger, which cools the attached sample by conduction (figure 4-8). This allows for a minimum stable temperature of 4.2 K, with the possibility of temporarily reaching lower temperatures by inducing He evaporation. Higher temperatures were maintained by counteracting the cooling of the He flow with a resistive heating element, located near the end of the cold finger between the He flow and the sample

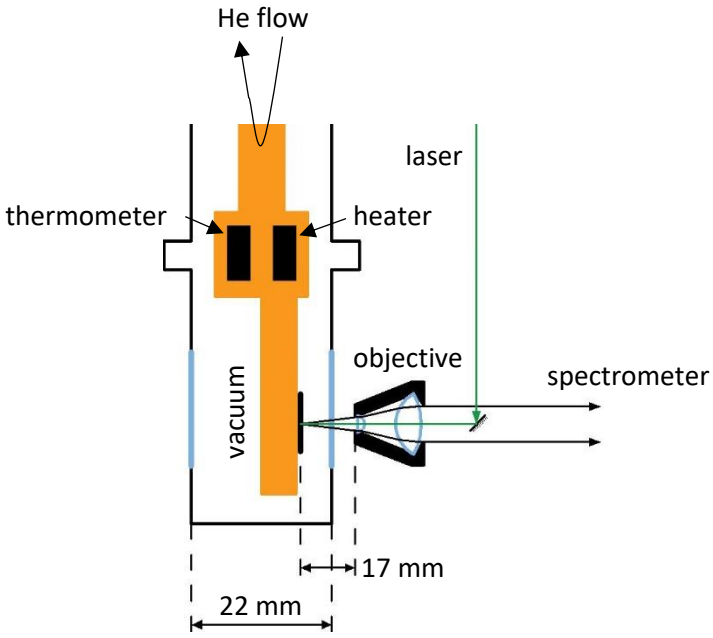

Figure 4-8: Cryostat and objective lens configuration. The incoming laser (green arrow) passes through the objective lens onto the sample (black), and the Raman signal (black arrows) is collected by the same lens and is sent to the spectrometer.

space (figure 4-8). Any temperature between 300 and 4.2 K could be reached first through coarse adjustments of the flow regulating valve on the helium input and then through fine adjustments of the resistive heating element, controlled by an Oxford

Instruments intelligent temperature controller (ITC). The ITC is a proportional-integral-differential (PID) controller, automatically adjusting the heating current based on a temperature sensor in the cold finger, located next to the heating element (figure 4-8). Due to the location of the temperature sensor and the heater to the sample and He input, a temperature stabilisation delay was required to allow the sample to reach temperature equilibrium with the sensor.

Samples were attached to the cold finger using a rubber latex glue deposited in a heptane solvent, which, when dry, is resistant to both vacuum and low temperature conditions. The latex also maintains sufficient flexibility at low temperatures for samples to avoid differential thermal contraction effects between the samples and the cold finger. To achieve a consistent sample orientation and maintain maximum thermal contact between samples and the holder, samples were glued along the sample top and bottom edge, allowing direct copper (Cu) to silicon (Si) thermal contact. Glue deposits between the sample and holder would not only reduce the thermal conductivity from copper to silicon, but introduce a varying sample tilt with respect to the holder.

4.6.2 Stage mounting

The cryostat was suspended in front of the laser path from a three-axis translation stage. The stage clamped to the cryostat near the points where the vacuum and helium lines attached to the cryostat to reduce torque from external movement. The sample holder was designed such that the sample was mounted offset to the cryostat centre line and closer to the viewing window. This ensured that long working distance

objectives would remain clear of physical contact with the viewing window, preventing breakages.

The laser was aimed at the sample with the assistance of a video microscope, inserted between the laser mirror and spectrometer in figure 4-8. This equipment positioning allowed the sample to be viewed under bright field illumination while at the same time observing the laser spot position. The laser spot was measured using known feature lengths to be at least 6 μm along its shortest diameter. This gave the lower limit of graphene sample size in order to select areas free from flake edge effects and metal deposition strains.

4.6.3 Vibration damping

Significant sample vibrations were caused by both the vacuum pump and the helium flow pump oscillations. At the micron scale of the graphene samples, these vibrations made maintaining laser accuracy impossible. Vacuum pump vibrations could be avoided by not pumping during measurements as the cryostat was able to maintain vacuum pressures below 10^{-4} mbar for the 8 hour experiment duration, sufficient to maintain the required insulation of the vacuum chamber. Clamping of both the pumping and helium flow lines to a large stabilising mass proved to sufficiently damp oscillations from both sources such that they were not observable under microscope magnification.

The flow rates required for temperatures below 6 K caused inconsistent sample oscillations with the same period as the temperature oscillations, which could not be consistently damped. This prevented samples being measured below these temperatures. Avoiding the temperature range below 6 K is not disruptive as the

thermal expansion differential between graphene and silicon from 4.2 K to 6 K is significantly less than at any other temperature. The temperature range <10 K is predicted to have an insignificant effect on total strain as demonstrated in figure 3-6.

4.7 Laser

A Uniphase 2214-25MLYVW argon ion (Ar^+) laser, filtered to output at the 514.5 nm emission line was used for Raman excitation. The laser output was heavily filtered with three bandpass filters with an attenuation factor of 10^6 outside the bandpass width of 3 nm, to remove fluorescence emissions from minor Ar^+ transitions. The heavy filtering was necessary as these satellite emissions ranged from an equal to significantly greater intensity than the graphene Raman signals being studied. At the filtered wavelength, the laser output a power of 24 mW as measured at the laser output by the heating a thermopile sensor, after the bandpass filters and without any neutral density (ND) filters. All incident powers quoted in this study were measured from this position, before the mirror and objective in figure 4-8. The laser power was adjusted by placing ND filters after the bandpass filters, with the laser always operating at maximum power output. The laser was primarily linearly polarised with an 80:20 ratio between orthogonal polarisations, where 80% was the maximum output at any polarisation orientation.

An excitation wavelength shorter than 600 nm was selected for this experiment to avoid the broad silicon infrared photoluminescence (PL) signal from the sample substrate. The tail end of which is significant in magnitude compared to the graphene

Raman signal and adds a distorting, nonlinear background to the signal, such as when using a 795 nm wavelength laser.

4.7.1 Laser damage

In addition to the unintentional laser heating effects, described in previously, the Raman laser power must also be limited to prevent sample damage caused by laser exposure. Exposure to laser powers above 7 mW caused visible discolorations of smaller size than the laser spot on the surface on graphene samples, after 8-18 hours of accumulated exposure.

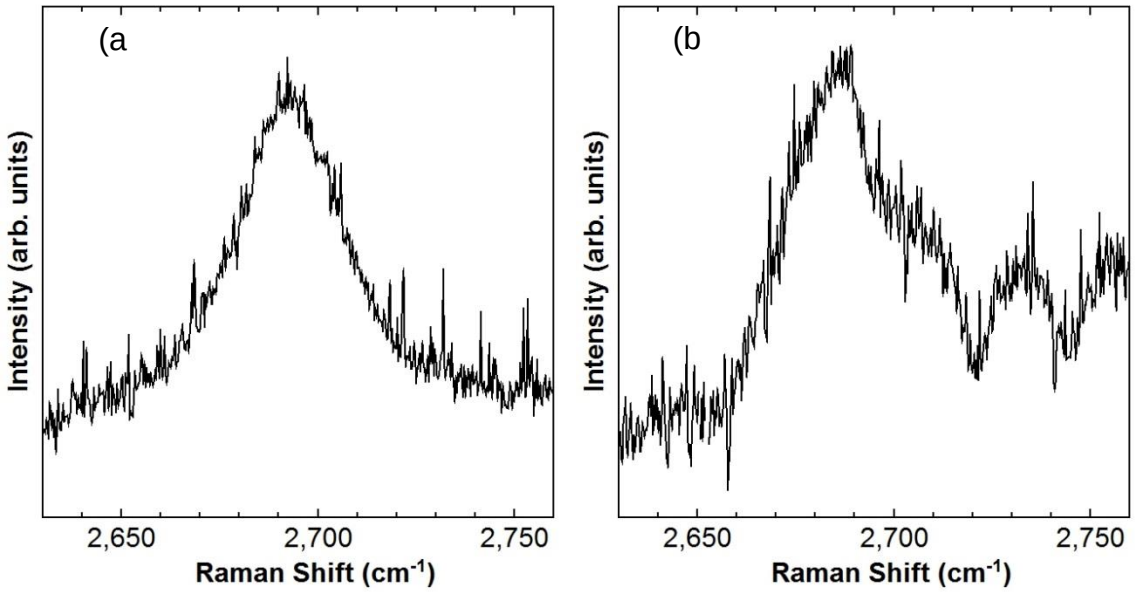

Figure 4-9: Before (a) and after (b) effect of laser-induced damage on the 2D Raman peak of the graphene sample shown in figure 4-10 (c). The G peak also undergoes the same distortion.

The damage is also indicated by a change in the background signal of the measured Raman spectra as shown in figure 4-9: a general increase in background level and the appearance anomalous spectral features. This damage threshold time appears

to be dictated by sample size, as smaller samples have limited heat dissipation or because it forces repeated laser exposure on the same location. The onset and extent of damage appears independent of cumulative laser exposure. The progression of the discolouration is displayed in figure 4-10. The discoloration is a change in the interference length of the light reflected off the silicon substrate base, therefore the combined thickness of the sample and silicon oxide layer is changed in this damage process.

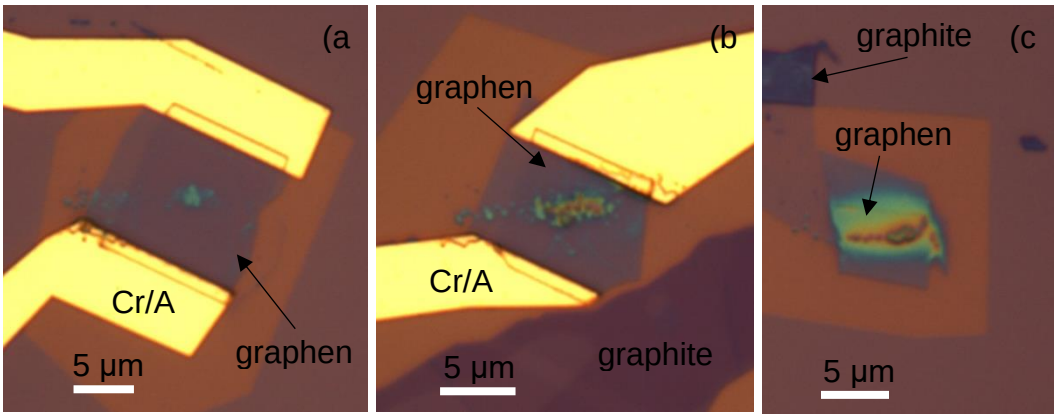

Figure 4-10: Left to right: progression of the visible discoloration caused by laser exposure given by examples across three different samples. (a) Nailed graphene after 2130 mins. of cumulative exposure, (b) contacted graphene after 330 mins. of cumulative exposure and (c) uncontacted graphene after 680 mins. of cumulative exposure.

4.7.2 AFM analysis

The microscope image cannot determine if the laser-induced damage features are protruding or recessed from the graphene surface, only that there is a height difference. Therefore the features were measured using an AFM (atomic force microscope, section 2.5) to determine their height profile, using an 8 nm radius probe tip in tapping mode.

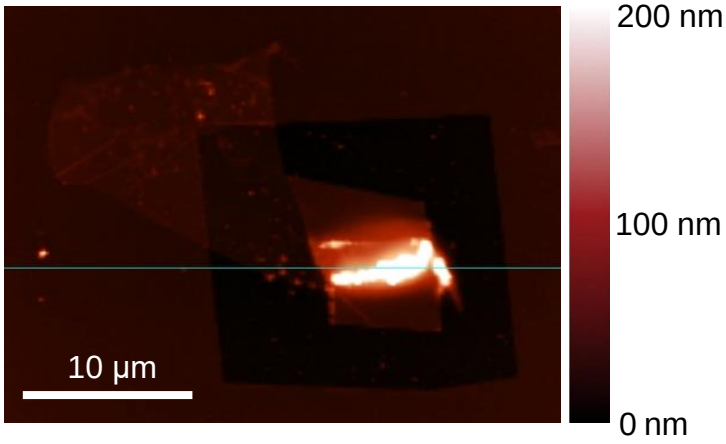

Figure 4-11: AFM micrograph of damage of figure 3-10 (c). The grey line denotes the AFM tip path for the 1D height profile measurement.

The measurements in Figure 4-11 found that the damaged regions are significantly raised above the surface of the graphene and sample. The damage has a peak height of 680 nm above the graphene surface height, as measured in the 1D height profile from figure 4-11. Peak heights of 50 nm and 250 nm above the graphene were also observed for the samples in figure 4-10 (a) and (b) respectively. These results demonstrate that this sample damage is not a laser ablation process, but more likely an induced chemical reaction within the sample. The samples were measured in vacuum conditions: 10^{-5}–10^{-6} mbar, making chemical reactions with air molecules unlikely.

4.7.3 SEM analysis

The damaged regions were also analysed with an SEM (scanning electron microscope, section 2.6) to determine their elemental composition using EDS (electron diffraction spectroscopy) in an attempt to determine the nature of the sample damage, shown in figure 4-12. The improved resolution of the SEM reveals that the smallest damage features are in the order of 200 nm in size, which is below

the laser excitation wavelength (514.5 nm) and are hemispherical in shape. This again suggests a chemical reaction is responsible, as heating damage should not be concentrated to an area smaller than the heating mechanism.

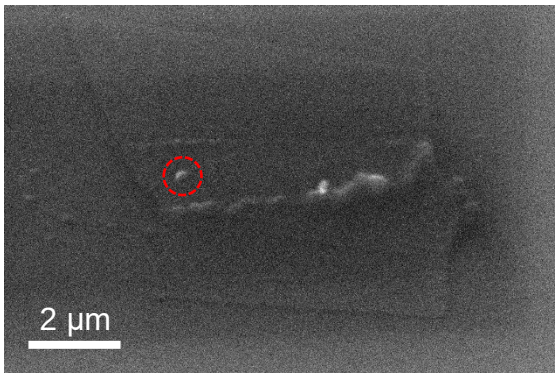

Figure 4-12: SEM image of the sample in figure 3-10 (c) and figure 3-11. Specific damage from EDS sampling is highlighted with a red circle.

A series of EDS sampling points, using a 10 kV electron acceleration potential, were taken across the sample in figure 4-12: 10 on the damaged regions, 10 on the graphene regions and 6 control points on the bare Si/SiO_2 substrate. All sampling points detected silicon, oxygen and carbon atoms in varying ratios, which rules out reactions with atmospheric nitrogen. The detection of carbon atoms away from the graphene region is attributed to the sampling area of the EDS being significantly larger than the damage features it creates (figure 4-12, red circle) and thus overlapping graphene regions to some extent in all cases. This also makes the differences between the damaged and undamaged regions difficult to resolve due to overlapping sampling areas. This results in the carbon ratio, by number of atoms, to be 42.6 ± 0.6 % on the bare substrate, 59 ± 2 % on graphene, and 63 ± 0.4 % on damaged areas, with silicon and oxygen ratios exhibiting an inverse trend. The damaged regions have only a small increase in carbon ratio over graphene regions.

It is unlikely that these raised regions are depositions due to the vacuum environment and more likely created by a re-structuring of the existing sample and substrate material present.

As mentioned in section 2.6, EDS analysis of elements lighter than neon can be unreliable due to the proximity between inner and outer shell electrons. Therefore, these measurements should not be taken as absolute atomic ratios. Further measurements of graphene are made at lower laser powers (3-7 mW). The lower power significantly reduces the incidence of damage to around one in twelve, but does not prevent it in every case. This was an acceptable improvement in failure rate, previously 100%, while maintaining an acceptable signal to noise ratio. Results in these damage cases have been removed from further analysis.

4.8 Calibration

4.8.1 ITC calibration

The ITC control was calibrated for the rhodium-iron (RhFe) resistance thermal sensor in the cryostat using a variable resistor. The resistor was used in the place of the thermometer in the ITC circuit to manually input the temperature-resistance profile required for the ITC calibration. The RhFe resistance profile was previously measured by fitting a standard RhFe temperature-resistance curve to a three-point resistance measurement of the thermocouple, spanning the temperature range of the thermal sensor of 500 K to 3 K. This resulted in a temperature uncertainty of ± 2 K at 500 K and ± 0.05 at 3 K.

4.8.2 Spectrometer calibration

A two-stage spectrometer was used to measure the Raman signals, which used a dispersive diffraction grating to select the wavelength measured by a charge-coupled device (CCD). The CCD had square pixels with a side length of 25 μm, which gave a resolution of 0.008 nm per pixel. The spectral range across the entire CCD for a static exposure was therefore 4.3 nm (491 pix.), and the range for a Raman spectra was between 150 cm^{-1}, at a 1400 cm^{-1} shift from the 514.5 nm laser wavelength, and 130 cm^{-1}, at a 2700 cm^{-1} shift from the laser. The difference in spectral ranges at different Raman shifts is caused by CCD capturing a constant wavelength range at all wavelengths. These spectral ranges were broad enough to capture any one of the graphene and multilayer Raman peaks in a single CCD exposure. The spectrometer diffraction grating angle was calibrated using the emission lines of a mercury (Hg) lamp. Calibration was performed using the 546.1 nm, 578.2 nm, and 576.96 nm mercury lines, due to their wavelength proximity to the graphene G (560.2 nm) and 2D (597.5 nm) Raman shifts from the laser wavelength used.

Calibration drifts of up to 7 cm^{-1}, for both G and 2D graphene Raman peaks, were observed and corrected during the course of the experiment. If present when performing the correlation method from section 2.3.6, this calibration offset would resemble a shift in the overall doping level in the sample. This is because doping shifts the G and 2D peaks by a similar amount to each other, unlike strain which causes an inequivalent peak shift. Therefore, a correlation offset would not result in an error in strain, but an incorrect shift to the doping magnitude.

4.8.3 Signal to noise intensity

The signal to noise ratio was optimised through adjustments of the experimental equipment: the laser power, beam path, spectrometer entrance slit width and CCD exposure time were used to increase signal strength.

The Raman signal could be linearly increased with an increase in the incident laser power, however, the power had to be balanced against laser heating effects reducing sample temperature accuracy.[97] Assuming thermal contact between the sample and cold finger, it was estimated that laser powers below 10 mW would cause heating of less than 3 K at cryogenic helium temperature (4.2 K), where the thermal conductivity of the substrate is the lowest.[98] This was confirmed by observing no change in peak behaviour around the 4.2 K low temperature limit when the laser power was varied from 14 mW to 3 mW. The presence of laser heating would be expected to introduce an effective minimum temperature at the sample surface and prevent changes of the observed Raman trends when decreasing the temperature further.

The mirror position in figure 4-8 was adjusted to maximise the Raman signal reaching the spectrometer. By reflecting the laser beam off the corner of the mirror, the rest of the mirror was positioned out of the signal path between the objective and the spectrometer. A conventional beam splitter is not able to provide more than 100 % combined throughput of the laser and signal which is achievable with this mirror system.

The spectrometer entrance aperture width determines both the amount of signal that enters the spectrometer, and also the permitted range of incident angles of the signal through the entrance. This allowed for the total signal incident on the CCD detector

to be increased at the cost of wavelength resolution at the CCD due to the increase in focal points at the spectrometer entrance.

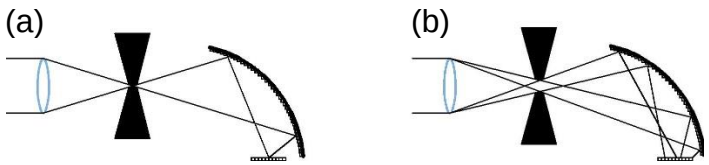

Figure 4-13: Effect of widening spectrometer aperture slits. (a) Perfect point-source slits (black) focus monochromatic light onto the same point of the CCD when reflecting off the diffraction grating. (b) An entrance slit of finite width creates a continuum of focal points at the slit and CCD. This causes multiple pixels to be illuminated by the same photon wavelength.

This broadening is insignificant when it is less than that of the natural spectral peak width being measured. For example, the graphene Raman G peak from figure 2-13 has a peak width of 13 cm^{-1} (0.42 nm). Therefore, artificial peak broadening was minimised while maximising signal by using a slit width of 300 μm. This width gave an approximate peak broadening of 0.25 nm, which is less than the FWHM of the G peak signal.

Increasing the CCD exposure time is the means of increasing the signal-to-noise ratio that does not have a quality trade-off. Taking a longer average of incident photons increases the dominance of the consistent Raman signal over the random nose. The signal to noise improvement should scale as a function of square root of the collection time, as with the error of an average. Including the previous signal to noise calibrations, an exposure time of 5 minutes gave an acceptable ratio of peak intensity to noise magnitude of ≥ 7, with minor improvements using longer exposure times. However, there was a hardware saturation limit with exposure time: the CCD pixel charge did not reset until the end of an exposure, therefore there was a

cumulative maximum number of photon counts a pixel could store before saturating. This gave a maximum exposure time of

$$t = \frac{c_0}{I}, \quad (1)$$

where t has been changed from chapter 1 to now be the maximum exposure time, I is the intensity rate of the signal in the inverse units of the exposure time, and c_0 is the maximum cumulative pixel count of 32000. While this upper limit did not affect Raman measurements ($s = 4$ hours), it was an issue during spectrometer alignment measurements where maximum laser powers and signal strengths were required.

4.8.4 Spectrometer alignment

Spectrometer and laser alignment was achieved using the fluorescent polymer F8BT (Poly[9,9-dioctylfluorene-alt-benzothiadiazole]) which has a band gap in the visible spectrum of a different wavelength to the laser. F8BT was drop-cast in solution onto a bare region of the graphene device substrates at a concentration of 25 mg ml^{-1}. This created an emissive film coating which, unlike Raman or Si PL signals, was visibly distinguishable from the reflected laser beam and originated from the same plane and orientation as the graphene sample would be. Maximising the F8BT PL signal at the spectrometer was sufficient to observe a graphite Raman signal at the maximum laser output. The graphite Raman signal was then similarly maximised, allowing the measurement of graphene Raman signals at the laser powers used for results measurement.

4.9 Conclusion

The fabrication processes detailed in this chapter of the un-contacted, contacted and nailed-contact samples are the means by which all samples measured in this study were made. These devices allowed for a comparison between the typical methods used for optical spectroscopy of graphene, an uncontacted flake, and that of electronic measurements, using metal contacts.

The laser induced sample damage was not expected as only incorrect temperature measurement was predicted from laser heating. The further analysis of the affected regions was inconclusive as to the exact mechanism of the damage beyond laser exposure.

The cryostat and spectrometer were adjusted to optimise the Raman signal from graphene samples. This resulted in a required exposure times of 5-10 minutes to obtain a satisfactory signal to noise ratio. The optimisation was necessary because the narrow angular aperture of the long working distance objective lens did not collect a large portion of the sample signal and the ionised gas laser generating noise from fluorescence.

5 Results

This chapter starts with covering the Raman spectroscopy measurements performed on one to three layer graphene on SiO_2 substrates. The strain behaviour with temperature (T) of these materials is examined and thermal expansion coefficients (TECs) of the samples are calculated. A comparison between the directions of temperature change is made, in addition to the differences in sample designs from section 4.4.

The correlation of spectral peaks from section 2.3.6 allows doping concentrations to be analysed in tandem with strain. Additional means of calculating dopant concentration from Raman spectra, described in section 2.3.4, are then employed to confirm these results.

The chapter then concludes with a preliminary study into the effects replacing the SiO_2 substrates with h-BN was made. Observations are then made about how significant an effect the flatter substrate has on the resultant strain and TEC of graphene.

5.1 Monolayer graphene

This section deals with the Raman measurements of monolayer graphene, and the processes used to calculate the strain, Thermal expansion coefficient and doping from this data. The nature and magnitude of the strain are discussed with respect to the theoretical predictions and the TEC is compared to theoretical calculations. From now on, graphene will be referred to as monolayer graphene to differentiate it between bilayer and tri-layer graphene.

5.1.1 Raman spectroscopy

Using the apparatus described in chapter 4, the characteristic G and 2D Raman peaks are measured in runs between room temperature to near liquid helium temperatures of 4-6 K in two directions. Method 1 consisted of starting at room temperature, cooling the sample slowly over the course of 8 hours down to 4-6 K, stopping to take Raman spectra during the cool down. Alternatively, in Method 2 the sample was quickly cooled to liquid helium temperatures in 10-15 minutes, the temperature was then allowed to stabilise for 30-60 minutes and slowly increased over 8 hours, taking Raman spectra in the same manner as before. This allowed the entire temperature range to be covered while maintaining a delay before each measurement is taken for temperature equilibration between the sensor and sample. Results are categorised by sample type as manufactured: “Uncontacted”, “Contacted” and “Nailed” describing the contact design used for each sample from section 4.4.

Three device types from a single flake

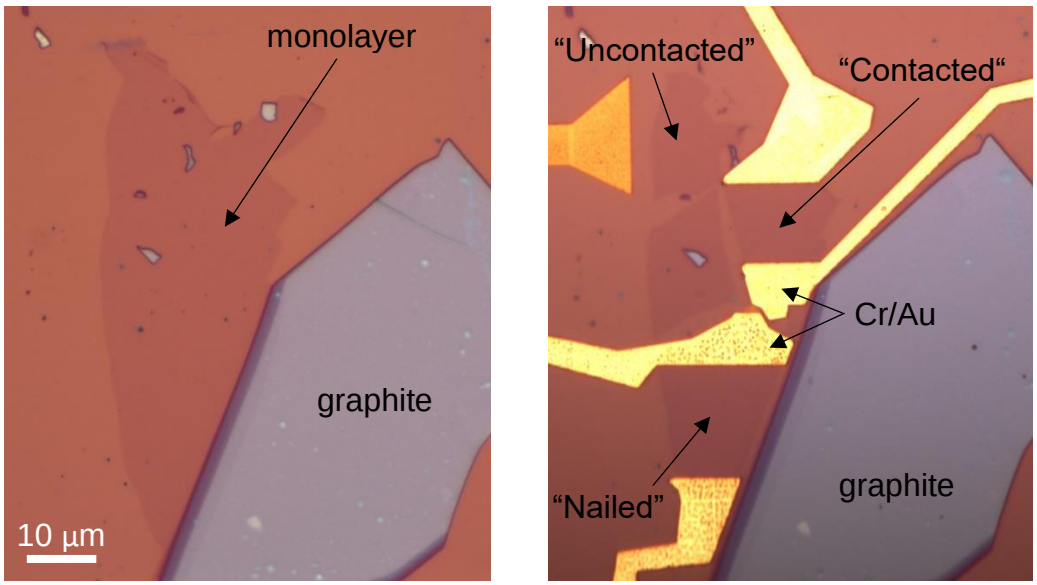

Figure 5-1: Three separate device types made out of a single monolayer flake (a) before and (b) after manufacture.

All three device types were made out of a single monolayer flake in order to test the different pinning effects they may create: “Uncontacted”, “Contacted” and “Nailed”. Figure 5-1 shows the initial flake and finished devices. This triple-sample flake will be used to demonstrate the process of obtaining strain, TEC and doping data.

Raman spectroscopy

These three samples were measured using Method 1, taking 30 K incremental steps down from room temperature, with a 20 minute delay at each increment before measuring to allow for temperature stabilisation. The Raman spectra were taken from the 514.5 nm laser described in section 4.7 at 3 mW output, an exposure time of 5 minutes and a spectral range of 130 cm^{-1} at the spectrometer. Figures 5-2 to 5-4 show a representative selection of the G and 2D Raman spectral peaks of all three devices as the temperature is changed.

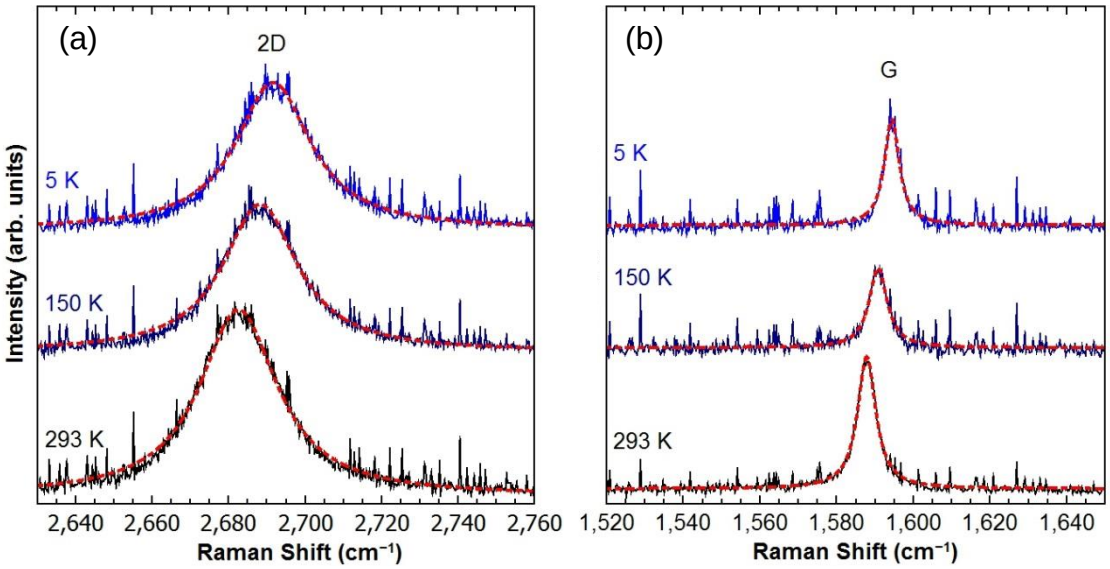

Figure 5-2: 2D (a) and G (b) peaks of the “uncontacted” monolayer sample as temperature is changed from 293 K down to 5 K. The red dashed lines show the Lorentzian functions which were fit over each of the peaks.

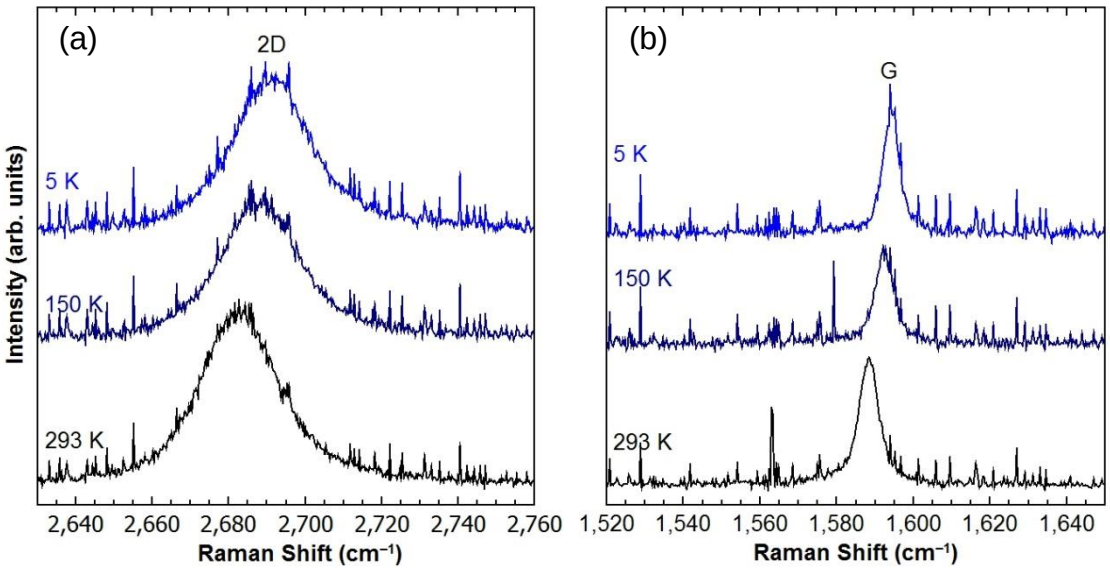

Figure 5-3: G (a) and 2D (b) peaks of the "contacted" monolayer sample as temperature is changed from 293 K down to 5 K.

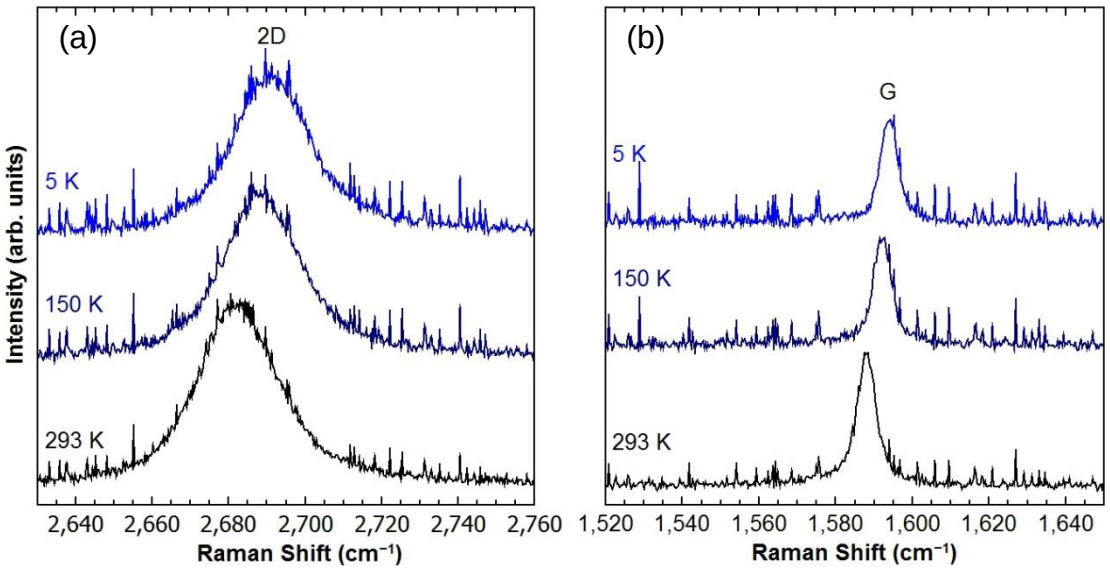

Figure 5-4: G (a) and 2D (b) peaks of the "nailed" monolayer sample as temperature is changed from 293 K down to 5 K.

All three device types exhibit a Lorentzian 2D and G peak at the frequency shift values expected from section 2.3.2. The 2D peak width is ~21 cm^{-1} at half intensity (FWHM), and is 1.4 times greater in height than the G peak, of ~6 cm^{-1} FWHM. These values are consistent with monolayer graphene with some level

of doping, induced by the manufacture process.[61,63,70,75,99-101] The peak characteristics do not exhibit any significant differences between the three contact types. The sharp spike spectral features arise from laser fluorescence lines and specular reflection off gold contacts, and are always present with varying intensity. Non-repeated peaks arise from random noise such as cosmic rays.

The Raman 2D and G peaks both show an increase in Raman shift energy with decreasing temperature which, as discussed in section 2.3.3, can be caused by an increase in compressive strain;[12-14,44,45,80] a shift in the doping level away from the Dirac point;[57,72] or temperature effects on the phonon anharmonic interactions.[71] A uniaxial strain breaks the degeneracy of orthogonal phonon vibrational directions, resulting in a split of both the 2D and G peaks.[12-14,65,66] This could be expected if the sample contacts were pulling or pushing on the graphene flakes along one axis, such as in the two-point contact geometries investigated. The Raman peak shape does not show this broadening or splitting with temperature, thus any strain measured is caused by an isotropic strain induced by the substrate's contact with the graphene.

5.1.2 Temperature dependence of peak position

The 2D and G peaks were modelled as a Lorentzian function, equation (5.1), and fit with a least squares algorithm after normalising the spectrum's baseline to zero:

$$y = \frac{2A}{\pi}\frac{w}{4(x - x_0)^2 + w^2}, \qquad (5.1)$$

where A, w and x_0 are the fitting parameters relating to the peak area, full width half maximum (FWHM) and central maximum position respectively. The Raman

energy shift value was taken from the x_0 fitting parameter. The peak positions were then examined as a function of temperature in figures 5-5 to 5-7.

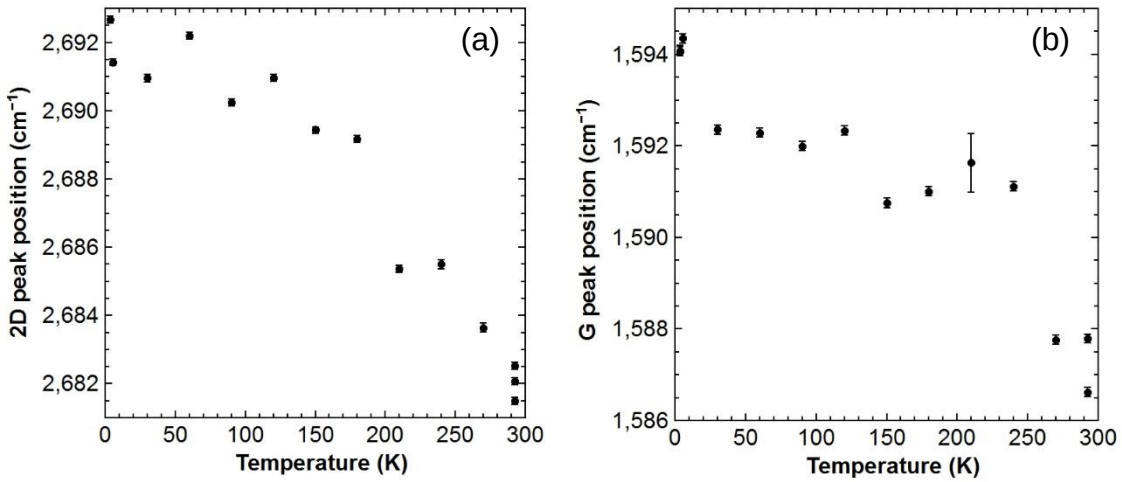

Figure 5-5: "Uncontacted" monolayer graphene 2D (a) and G (b) peak position with changing temperature.

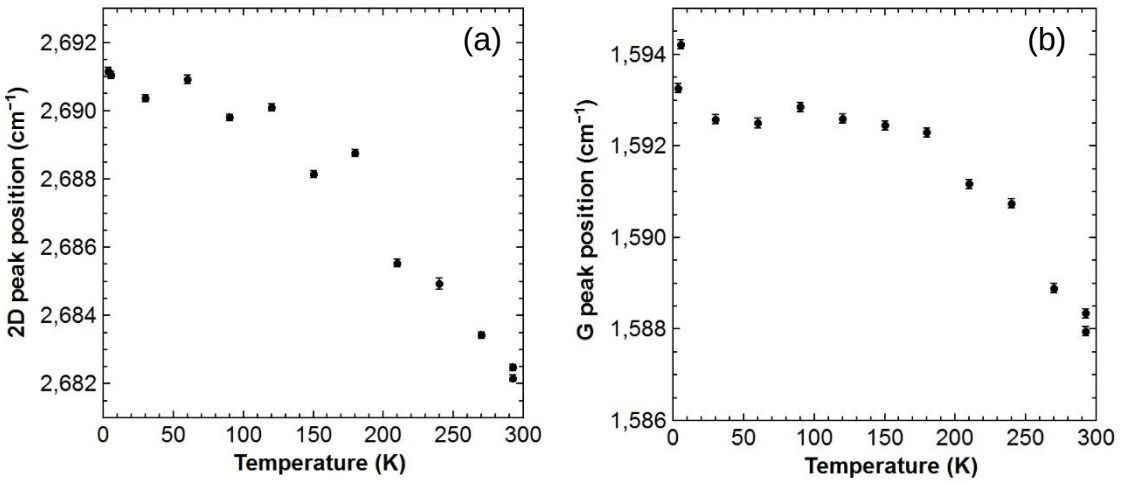

Figure 5-6: "Contacted" monolayer graphene 2D (a) and G (b) peak position with changing temperature.

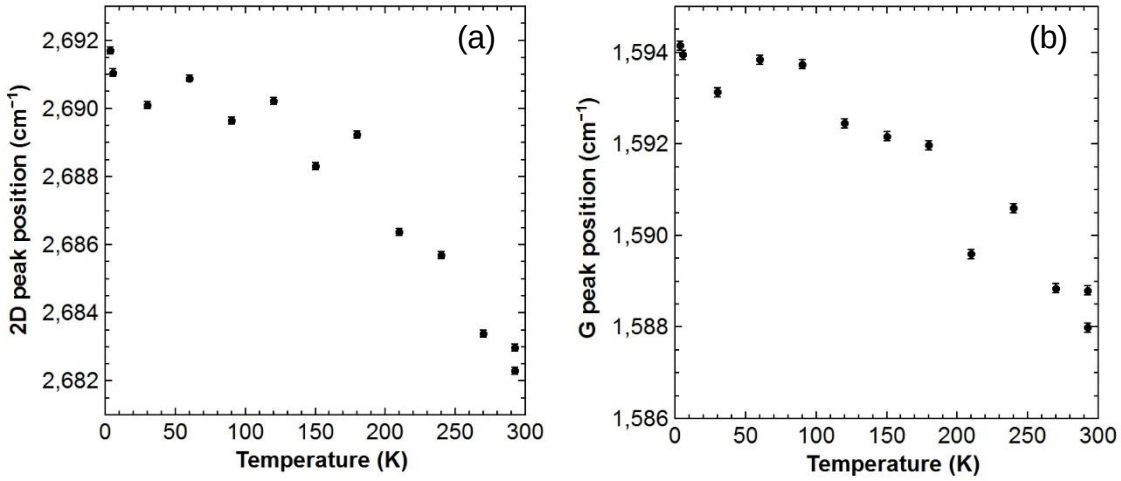

Figure 5-7: "Nailed" monolayer graphene 2D (a) and G (b) peak position with changing temperature.

All three samples show an increase in the Raman shift energy with decreasing temperature, for both 2D and G peaks, which is consistent with previous Raman measurements of this type.[46-48,55,102] Both peak positions also exhibit a non-linear change in Raman shift with temperature. This has also been observed in previous measurements and attributed to slipping or crumpling when the force required to strain the graphene becomes greater than the Van der Waals force between the graphene and substrate.[47,48] The error bars were calculated from the uncertainty in the Lorentzian fit to the spectral data. Additionally, the unusually large uncertainty in the uncontacted sample was the result of cosmic ray noise, coincident with the Raman peak position.

All three samples show scatter in individual peak positions, but in general exhibit a peak shift of 9-10 cm^{-1} for the 2D peak and 6-7 cm^{-1} for the G peak over the whole temperature range.

5.1.3 Strain – doping separation

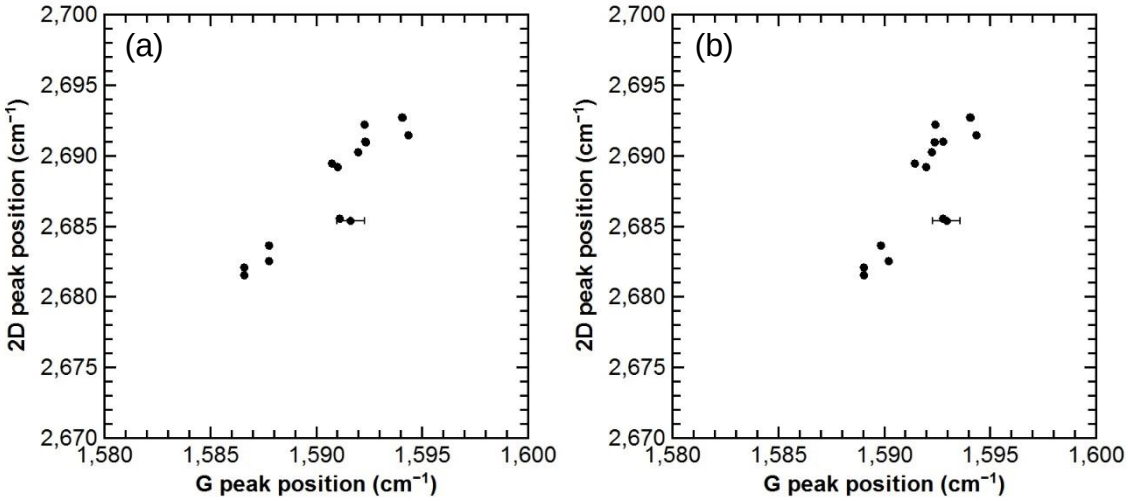

Figure 5-8: Before, (a), and after, (b), the G peak phonon shift contribution is removed from the correlation data of the sample, "uncontacted".

In order to extract the strain-only component of the peak positions the 2D/G peak correlation method is used, as described in section 2.3.6.[47,50,78] First, the independent contribution of the anharmonic phonon shift to the G peak is subtracted from the data, which has a magnitude of 3.4 cm^{-1} between zero Kelvin and room temperature.[47,48,71,76] Since this contributes ~50% of the total peak shift, it must be taken into account. The theoretical prediction of the phonon shift was fitted with a third order polynomial and subtracted from the measured G peak shift points. The 2D phonon temperature shift is not accounted for as the magnitude of the shift over the investigated temperature range, < $2cm^{-1}$, is much less than the peak shift caused by other contributions.[47,76] This caused the theoretical 2D phonon shift to have a contribution to the resultant strain and doping values less than the final uncertainty range. The modified peak positions are shown in figure 5-8, in the style of a correlation plot.

The strain and doping components are identified by their different effects on either the 2D or G peak positions. Strains cause a shift in the 2D peak position between

2.2 and 2.8 times larger than the corresponding shift in the G peak position.[44,45,78-80] Any strain-only peak shift in monolayer graphene should therefore only move the peak correlation position along a line with a gradient of 2.45. Equivalently, hole doping, or decrease in the Fermi energy causes a shift in the 2D peak that is 0.7 times that of the shift of the G peak.[70,78] Electron doping, or increases in the Fermi level, cause a shift in the 2D peak that is 0.26 times the G peak shift.[70,78] The differences in electron and hole doping were found not to significantly change the final strain dependences calculated, determined in section 5.1.9. Additionally, hole doping is the expected doping mechanism for graphene on a SiO_2 substrate, therefore results and analysis will be for the assumption that doping will follow a 0.7 gradient described previously.[47,50,78] A comparison between the two doping types is performed in section 5.5.

A measurement at minimal strain and doping is required to give an origin point for the strain and doping lines. This was found through measurements of suspended graphene monolayers, which should be minimally affected by the substrate strain and doping. This origin point was used to explicitly calculate strain and doping values. A G peak position of 1581.6 cm^{-1} and 2D peak position of 2677 cm^{-1} was used.[78]

5.1.4 Isolating strain and doping

The correlation graphs in figure 5-9 can be used to infer the strain and doping characteristics of the graphene samples. The neutrality point, where all three strain and doping lines meet denotes the origin position for a graphene flake with zero strain, tensile or compressive, and zero doping concentration. An increase in only tensile strain from this point would cause the correlation point to move downwards along the red strain line (ε_{exp}), due to the phonon softening it causes

on the 2D and G peaks, while an increase in only compressive strain from the neutrality point will causes the correlation to move upwards along the red strain line, with both 2D and G peak increasing in energy shift due to the corresponding phonon hardening.

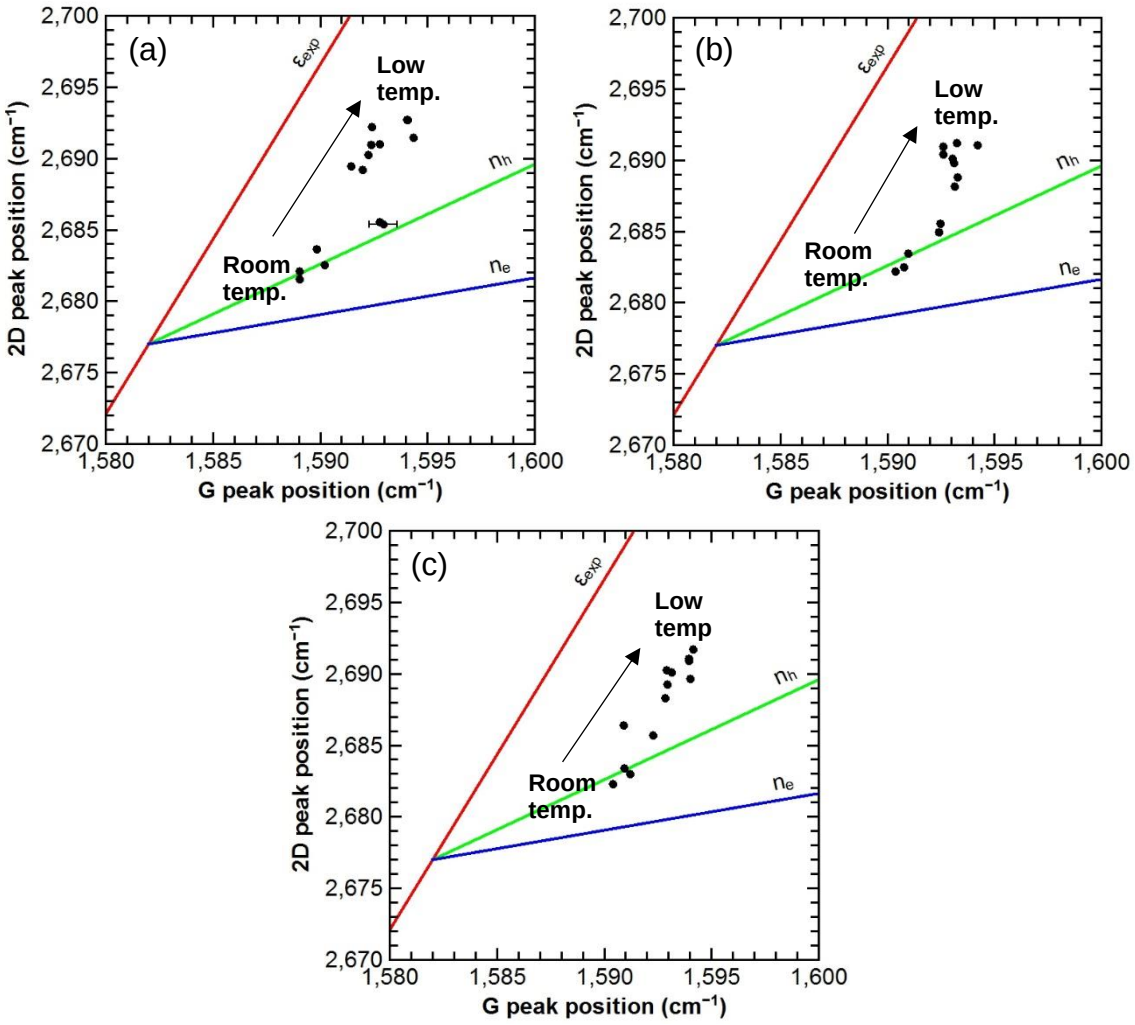

Figure 5-9: 2D – G peak correlation of uncontacted (a), contacted (b) and nailed (c) samples. Where ε_{exp} is the red zero-doping strain correlation, n_h is the green zero-strain hole-doping correlation, and n_e is the blue zero-strain electron doping correlation.

Unlike strain, increases in doping always shift the correlation point to the right along the doping line. Therefore, any position of the 2D and G peak correlation that sits to the right of the ε_{exp} strain line can be described as a combination of a strain-only component and a doping-only component. Since we are assuming hole doping, this will be a combination of the vectors of the ε_{exp} and n_h lines.

Figure 5-9 shows that all three samples start at approximately zero strain at room temperature, sitting on or near the n_h doping line. The three samples then all shift to some strain amount with decreasing temperature, with no clear net shift along the doping vector.

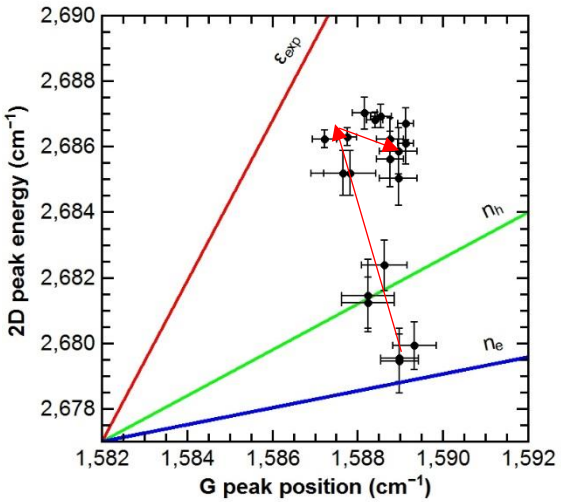

Figure 5-10: Example of large correlation point scatter and unusual relation. The red arrows indicate the temperature dependence of the correlation.

Two methods were investigated to isolate the strain and doping components of the correlation plots. The first was to fit the data set with a single line and anchor the data points to the line based on their G peak position compared to the fit line position. To obtain the strain (doping) values, the line was then shifted along the doping (strain) vector until it matched the strain (doping) line, dragging the data points with it. The values of these new point positions would be compared to the zero strain/doping position to determine their absolute strain (doping) shift. This method works for correlations with linear relations in 2D-G peak space. Other samples that have a large point scatter in correlation space, or with an unusual doping relation with temperature, such as in figure 5-10, there is a high chance of an incorrect shift being applied to the data points. Taking an averaged line through the data set will produce an incorrect shift to the data points at low temperatures.

The second method to determine the strain-only (doping-only) shift of the correlation points is by shifting the positions of the data set on an individual, point-by-point basis. Shifting each point along to the doping (strain) vector n_h (ε_{exp}) until they lie along the strain (doping) line, ε_{exp} (n_h), leaving the strain (doping) only component of the peak shift compared to the neutrality point. The G peak difference from the neutrality position was then used as the basis for calculating the strain amount from the Raman peak positions. This second method was used for all result from now on.

Phonons are related to lattice volume by the Grüneisen parameter, therefore Raman peak values can be related to strain. Measurements of graphene strain in doping free environments, such as flexible substrates and pressurised balloons put the G peak shift to biaxial strain ratio as 57 cm^{-1}/%, from a corresponding Grüneisen parameter of 1.8.[13,44]

5.1.5 Temperature dependence of strain

The strain shift of the G peak was used to calculate the strain, in a similar way to previous studies, and to also avoid the need to include the 2D peak shift contributions from anharmonic phonon effects.[47,62,71,76] The strain dependence with temperature, as a percentage strain, is shown in Figure 5-11, where negative (positive) values denote compressive (tensile) strain. The theoretically predicted strain from figure 3-6 is also overlaid onto the data, matched to the measured strain values at the lowest temperature with no fitting parameter to the gradient.

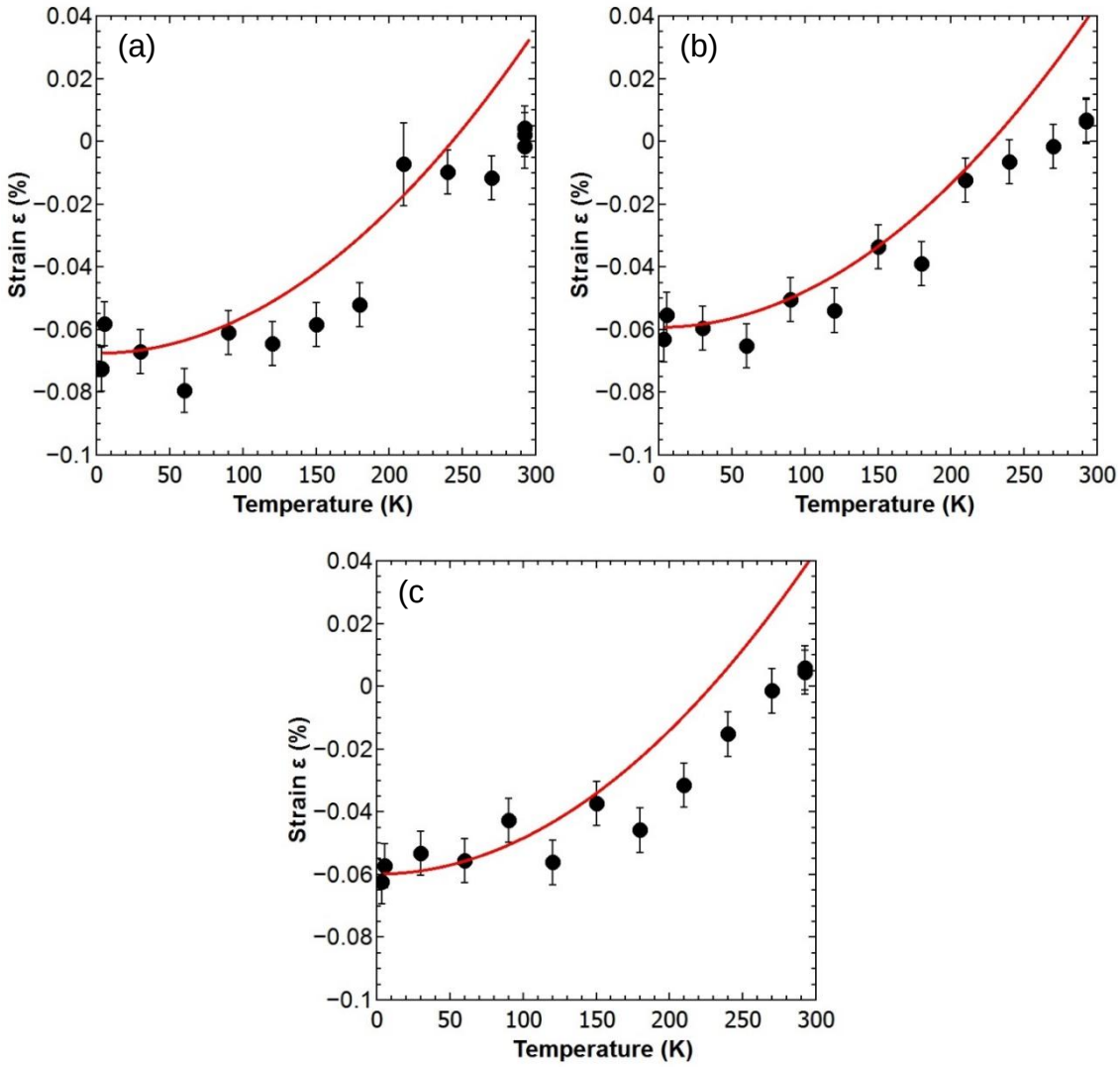

Figure 5-11: Strain dependence of uncontacted (a), contacted (b), and nailed (c) monolayer graphene samples as a function of temperature, as extracted from 2D and G peak correlation analysis. The red lines show the un-fitted theoretical predictions of strain using the theoretical TEC, figure 3-6.

All three sample types exhibit an approximately unstrained state at room temperature. The samples all increase in compressive strain as temperature decreases which is consistent with the expectation of a thermal expansion mismatch between graphene and a SiO_2/Si substrate. The strain gradient is not linear and turns to zero by around 100 K, resembling the theoretical prediction of a T^2 dependence of the strain from section 3.1.3. These results also show no significant strain difference within uncertainty between the three types of contacts used. This suggests that any kind of clamping effect caused by the gold contacts

does not significantly affect the surface contact and adhesion between the graphene and the substrate. Therefore, either the slipping or crumpling caused by compressive strains are not sufficiently prevented by the contacts, or the force of the strain is not large enough to overcome the inherent Van der Waals bonding between the graphene and SiO_2, such that contacts are not needed to induce the full TEC mismatch strain.

5.1.6 Warming and cooling differences

The strain shifts with temperature were compared depending on whether the sample was cooled slowly: method 1, or was cooled quickly: method 2, as defined in section 5.1.1. Here, the intention was to examine if there were hysteresis effects on the strain depending on the temperature cycle. This would be expected if there are sudden changes in strain state during thermal cycling, such as spontaneous crumpling or delamination. This behaviour was reported when heating graphene from room temperature on a substrate.[46,54]

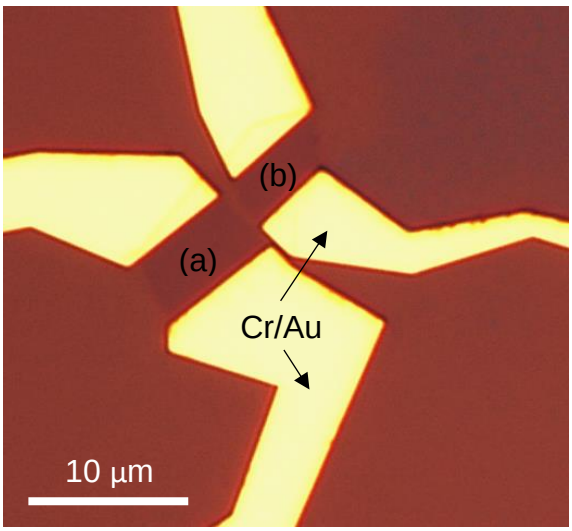

Figure 5-12: Monolayer graphene samples "nailed 2" (a) and "contacted 2" (b).

Two monolayer samples were compared, one contacted (contacted 2) and one with nailed contacts (nailed 2), between cooling methods 1 and 2, using 20-30 K steps and a 10-20 minute measurement delay. A 5 minute exposure time and 514.5 nm laser at 4 mW output were used as previously described in section 5.1.1. The two samples were made out of a single, continuous flake that was etched into two comparable samples, shown in figure 5-12. The Raman and strain values of these two samples were compared, as described previously.

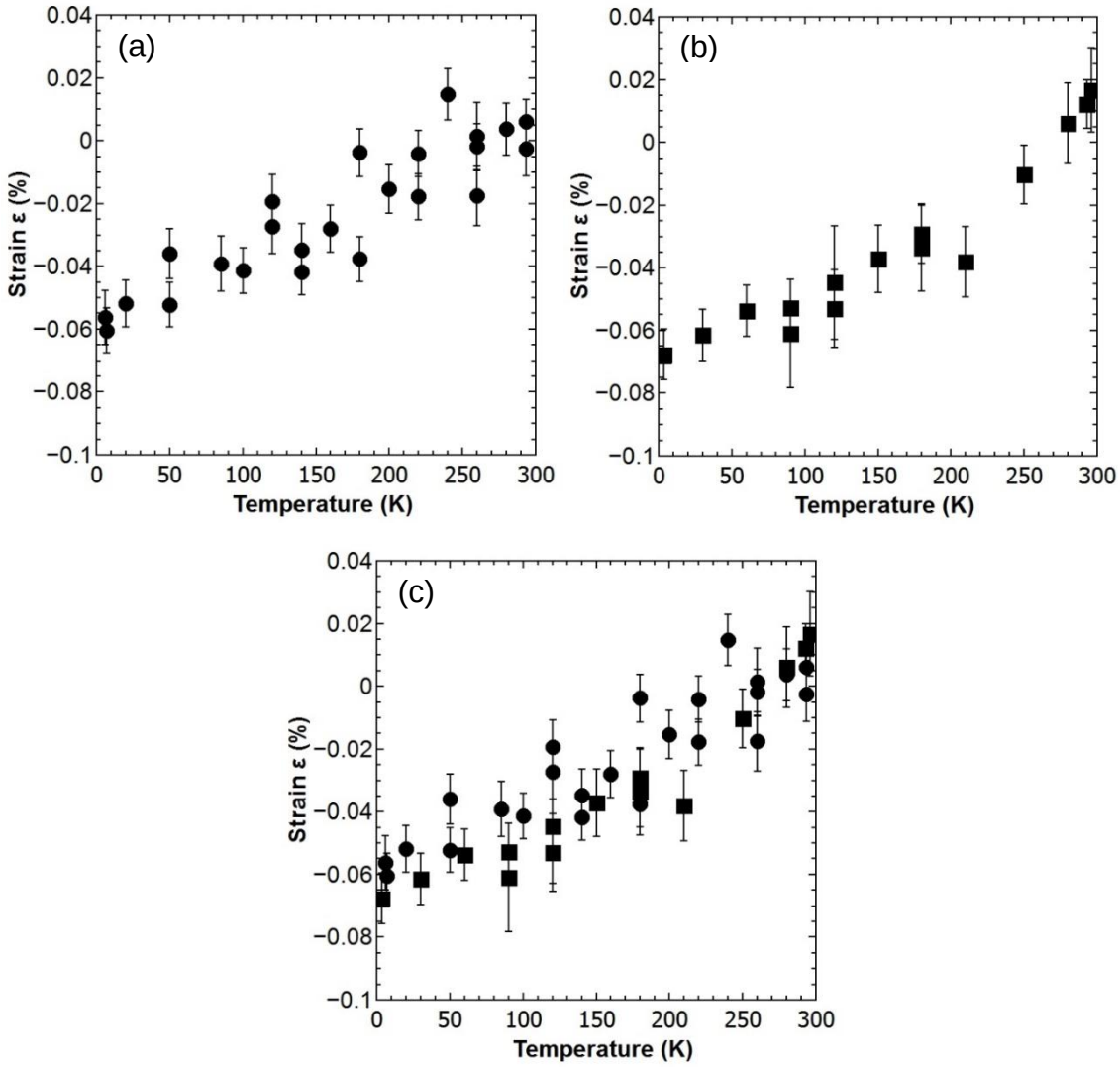

Figure 5-13: Strain dependence of contacted 2. Showing method 1 data (a), method 2 data (b), and with both data sets overlaid (c).

Method 1 and 2 are examined first separately, and then overlaid, in order to determine the amount of conformity between the data sets.

The sample in figure 5-13: contacted monolayer 2 has a similar strain profile when cooling slowly or warming slowly, and when overlaid, the data shows agreement between the two, within the uncertainty range of the strain values.

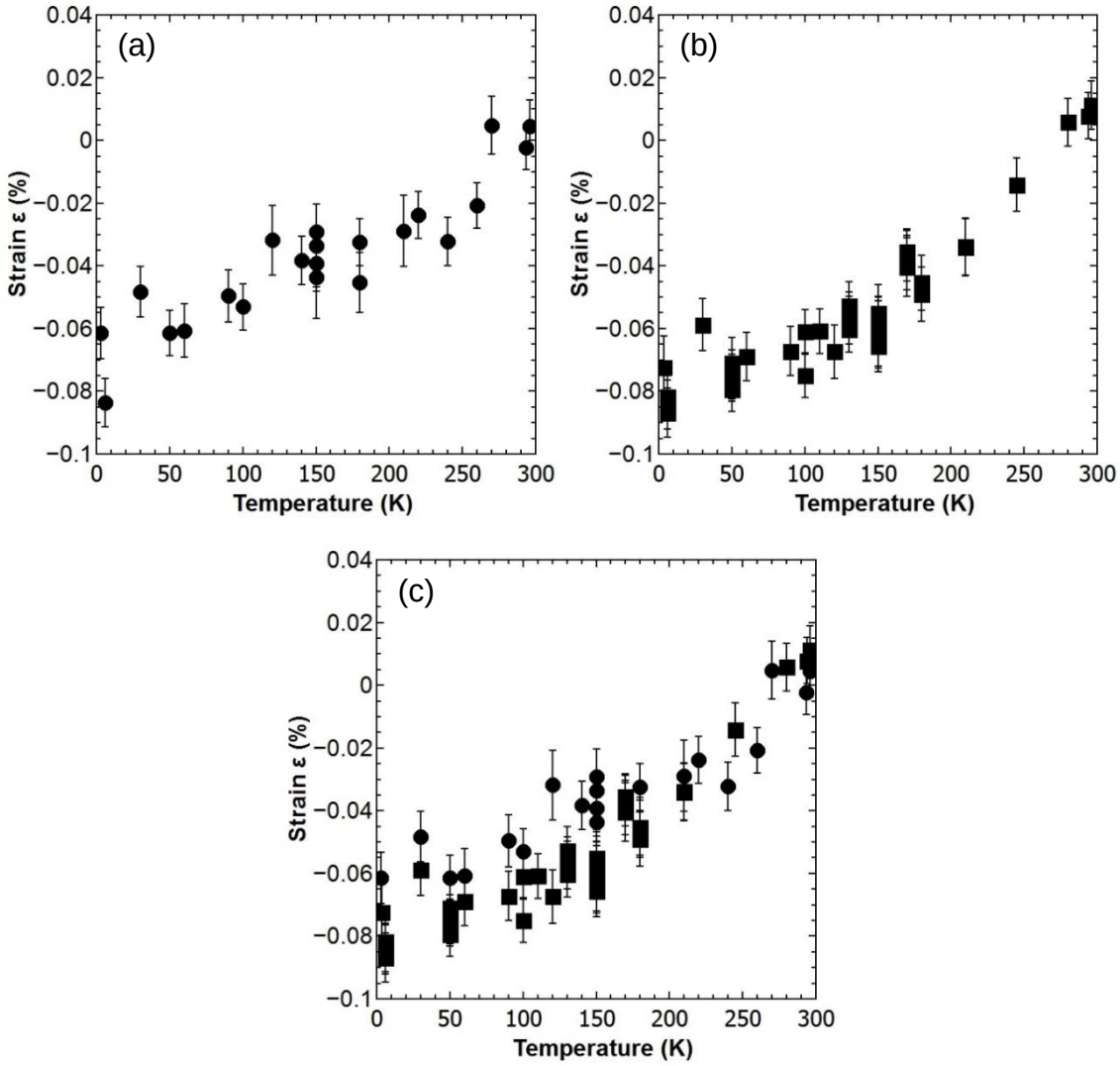

Figure 5-14: Strain dependence of nailed 2. Again, showing method 1 data (a), method 2 data (b), and with both data sets overlaid (c).

As with contacted 2, nailed 2, shown in figure 5-14, also shows agreement between the two different measurement cases, with the data of the two sets falling within each other's uncertainty range.

The uncertainty strain data does not always overlap at all temperatures, however the lack of consistent divergence between methods 1 and 2 at all temperatures and across all samples suggests that the two measurement methods do not

create a significant difference in strain dependence. Therefore it is likely that all temperature effects are comparable to each other, regardless of cooling method. This would allow the comparison of data measured at slowly varying temperatures with other experiments, such as electrical transport experiments which tend to use faster cooling and static temperatures.

5.1.7 Thermal expansion coefficient

In order to perform the reverse of the theoretical strain prediction: calculating a TEC from the measured strain data, fitting parameters are needed to match the theoretical function, equation (3.5), to the data. To start with, equation (5.2) was used as a parameterisation of the theoretical strain function:

$$\varepsilon = \frac{m}{2} T^n + c. \quad (5.2)$$

The value c is taken to be the lowest temperature measurement of strain, or the average of the lowest measurements when multiple measurements are available. No x^1 term was included as this would result in a differential with a constant term, and thus a TEC that does not tend to zero at 0 K. Equation (5.2) was then fitted to the three strain data sets of the uncontacted, contacted and nailed samples, using n and m as fitting parameters. This proved to be over-fitting and led to powers ranging from 0.9 to 3 with an uncertainty of up to 30%, and gradients ranging from 7×10^{-5} to 2×10^{-2} with uncertainties as high as 170%. When integrated to find the TEC dependence, these large errors cause the uncertainty in the calculated TECs to span the whole range from zero to beyond the theoretical TEC in every sample. The fitting parameters were then limited to only the gradient term, m, and keeping the power constant at $n = 2$, equation (5.3).

This value was the median of the fit values of n, and is also the prediction from the fit of the theoretical strain in equation (3.4),

$$\varepsilon = \frac{m}{2}T^2 + c. \quad (5.3)$$

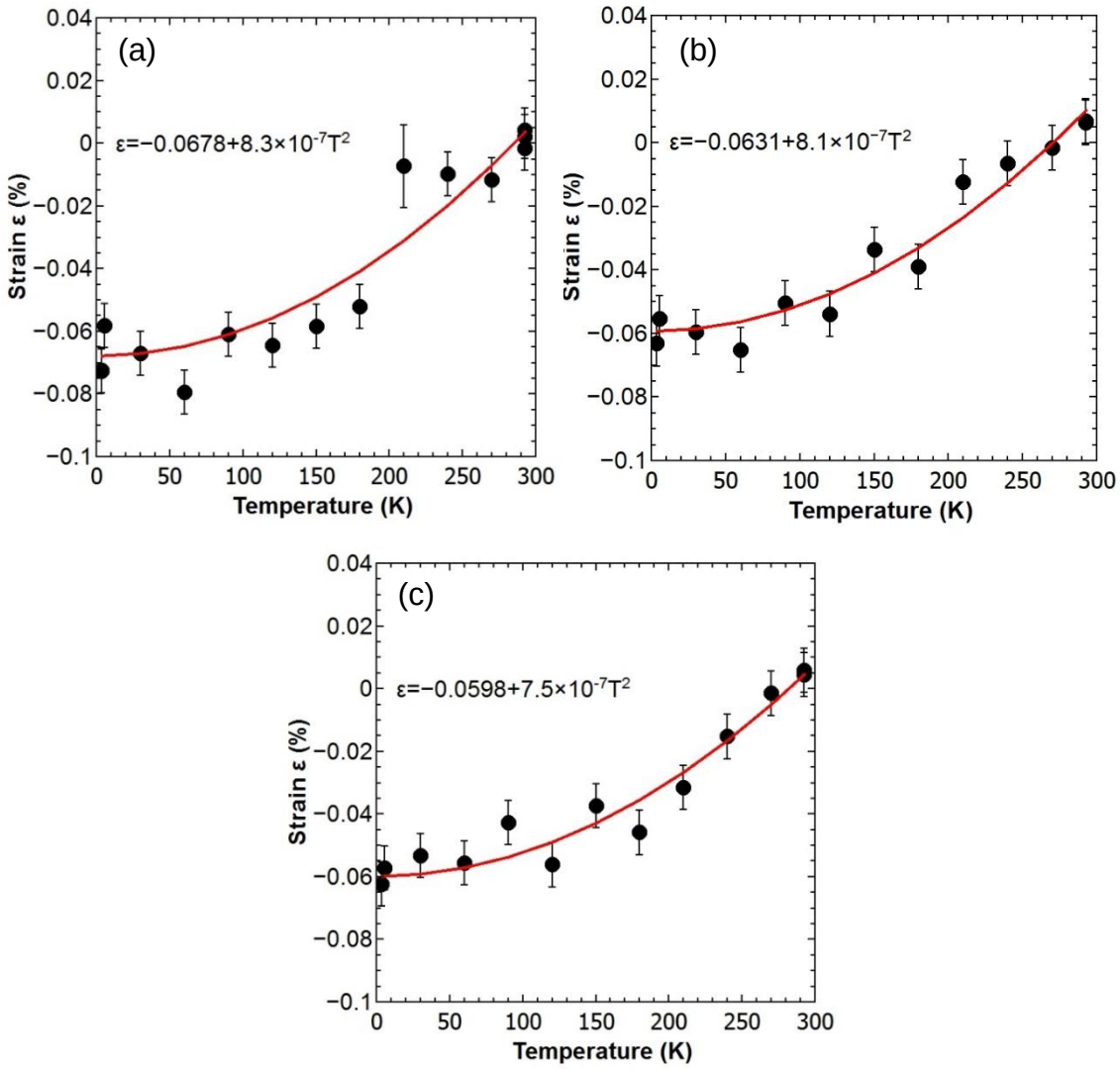

Figure 5-15: Strain dependence of uncontacted (a), contacted (b), and nailed (c) monolayer graphene samples as a function of temperature, with fitting using equation (3). The equation of the fit lines (blue) are displayed.

These fits are shown in figure 5-15, which takes the data from figure 5-11, using the fitting parameter, m, to fit the predicted strain to the measured results. This result in an uncertainty in m in the order of 5% which is acceptable. It should be noted that the theoretical TEC difference, in figure 3-5, between silicon and

graphene cannot be approximated as linear above 300 K. Therefore extrapolations of the fits beyond the range of figure 5-15 will not be valid as the strain is no longer a function of T^2. The TEC in the range of 0−300 K is then calculated by rearranging equation (3.4):

$$\alpha_{graphene} = \alpha_{Si} - mT, \quad (5.4)$$

and the calculated $\alpha_{graphene}$ is directly compared to the theoretical TEC in figure 5-16.

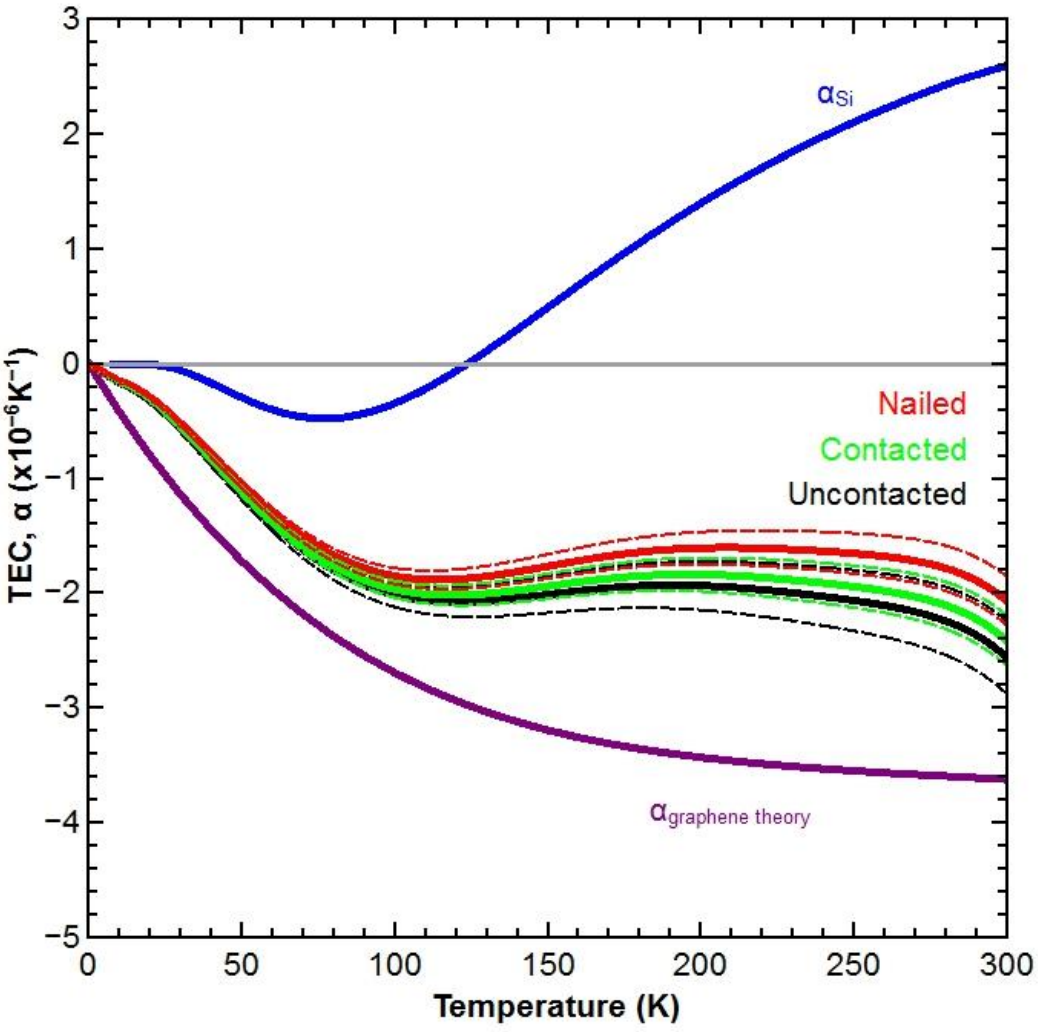

Figure 5-16: Calculated TECs from the three samples described: uncontacted (black), contacted (brown) and nailed (red). The upper and lower uncertainty bounds are given by the dashed lines in the corresponding colour. The TEC of silicon is in blue, and the predicted graphene TEC is purple.[20,93]

The TEC of the graphene samples exhibit a non-quadratic dependence with temperature. This arises from the subtraction of the linear differential of the data fit from the polynomial silicon TEC, which adds the polynomial trend of α_{Si} to the resultant graphene TECs. However, this still allows for a second order polynomial to fit approximately within the uncertainty bounds. In order to achieve a resultant graphene TEC dependence more fitting with the theory, a higher order polynomial fit would have to be considered when fitting the strain (figure 5-15), which was determined to not be appropriate given the added uncertainty from additional fitting parameters. An analysis of figure 5-16 reveals that the three samples, made from a single exfoliated flake, show a grouping of their TEC dependence with temperature around half the magnitude of the graphene theory prediction. Given the closeness of the overlap of their uncertainty bounds, the type of device contacts does not appear to have an effect on the resultant TEC with temperature, as seen previously with strain.

This independence of contact type was seen across all graphene monolayer flake devices, figure 5-17, which shows a significantly larger spread of TEC dependences in comparison to figure 5-16. This demonstrates that the sample variance is a greater factor for device attributes than any particular manufacturing technique.

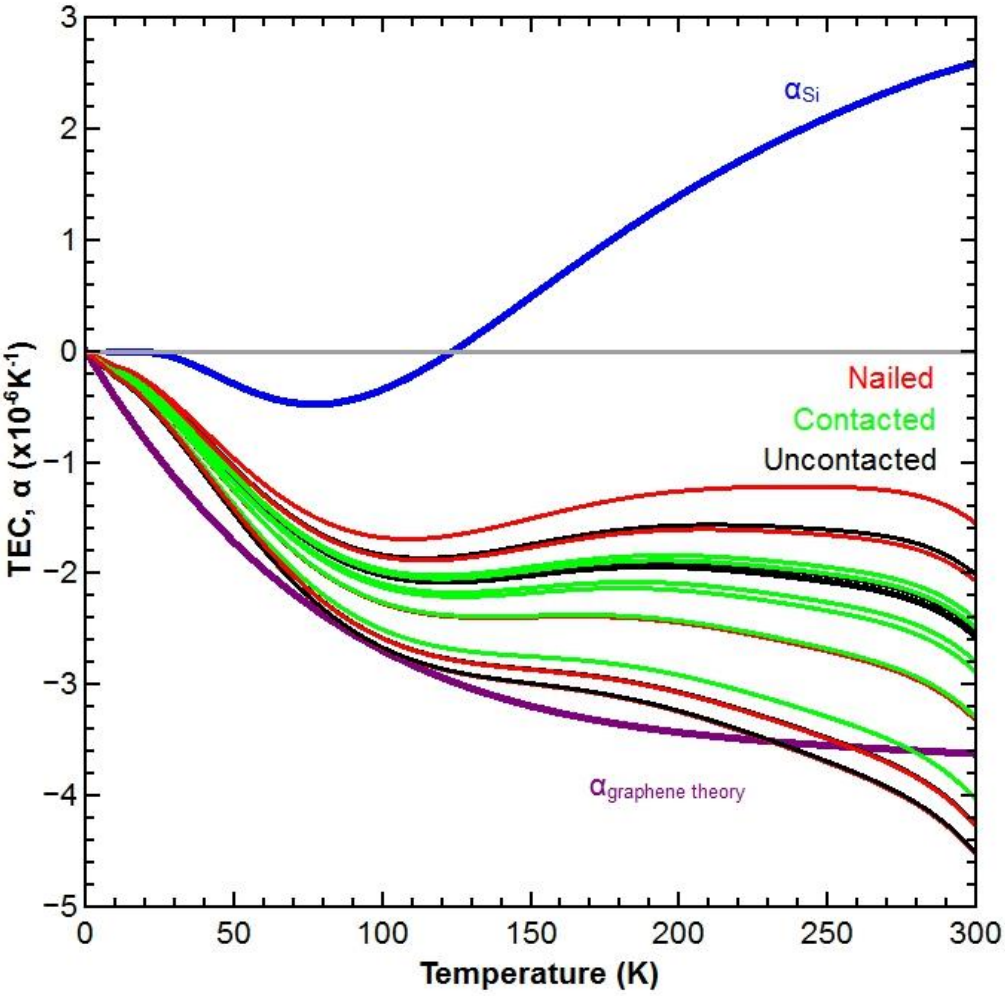

Figure 5-17: TEC dependence of all monolayer samples, showing all sample types: uncontacted (black), contacted (brown) and nailed (red). As before, the TEC of silicon is in blue, and the predicted graphene TEC is purple.[20,93]

5.1.8 Strain and TEC discussion

What is observed is a range of measured TEC values from $–1.2x10^{–6}$ $K^{–1}$ to $–3.8x10^{–6}$ $K^{–1}$ at 250 K, with the predicted theory value being a lower bound to the results, being $–3.6x10^{–6}$ $K^{–1}$ at the same temperature. This range of results is caused by the strain mechanisms varying across samples, since the assumption in the TEC calculation method used is that the change in strain is caused entirely by the Si-graphene TEC mismatch. Therefore, other mechanisms causing a

different resultant strain, such as crumpling or slipping, would result in a lower strain differential and affect the calculated TEC dependence. Given a distribution of exfoliated samples of graphene on a SiO_2 surface, there is a bias towards surface contact that reduce the maximum TEC strain rather than increase it, from bubbles and uneven surface contacts.[42,91] Therefore, the theoretical TEC is expected to be the lower bound for the range of calculated TEC values.

A crumpling or slipping of graphene on its substrate could be responsible for a lower observed strain gradient. In this case, when the force imparted by the substrate on the graphene, causing the strain, exceeds the Van der Waals force between the two, the graphene can slip, crumple or corrugate. When under a compressive strain, the graphene will expand and reduce the resultant strain. This would be expected to show as a transition in the strain dependence at some critical temperature to a plateau, or a transition to a reduced strain amount compared to the theoretical prediction.

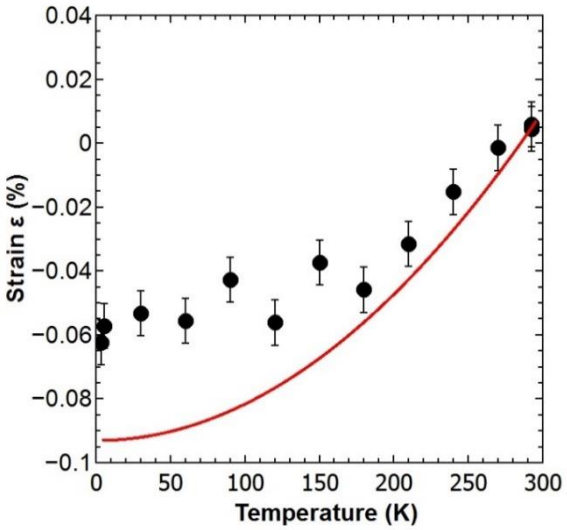

Figure 5-18: Strain dependence and predicted strain of the nailed sample from section 5.1.1 (figure 5-11 (c)) with the theoretical strain dependence (red) shifted to coincide with the room temperature data points.

This may be the case in the strain dependence of the nailed monolayer sample, figure 5-18, which displays the strain mostly conforming to the theory line at

higher temperatures and suddenly departing from this dependence at a critical temperature.

This mechanism should also cause a consistent under-estimation of the magnitude of the TEC across all samples. However, this does not predict the range of dependences observed in figure 5-18. This explanation could still be valid if the samples have a distribution of surface contact profiles, varying their Van der Waals interaction strength, if there are different levels of contact between the graphene and the substrate. This is justified as the SiO_2 surface of the substrates used presents an uneven surface to which graphene can have a varying amount of conformity, as depicted in figure 5-19, explaining the range of strain dependences observed up to the maximum of the theoretical prediction.[89,90] It would be difficult to use this data to calculate the amount of surface contact of individual samples, as the surface contact itself would be one of the fitting parameters as defined as the Van der Waals force between the graphene and surface.

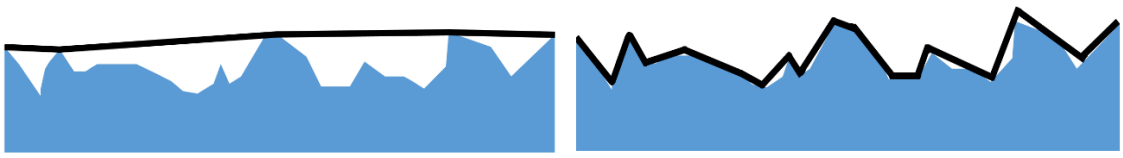

Figure 5-19: Representation of imperfect graphene contact with sample as manufactured at room temperature (left), and at some temperature T < room temperature, once the graphene has expanded to conform to the SiO_2. The SiO2 substrate is shown in blue and the graphene in black.

It could also be the case that graphene undergoes an amount of thermal expansion without strain. As in the situation depicted in figure 5-19, the graphene starts partially suspended on the SiO_2 surface, and as it expands with cooling, it fills in the gaps between the graphene and the substrate without being strained. Once the graphene fully conforms to the substrate, the graphene then undergoes

compressive strain, also causing the resultant total change in strain with temperature being lower than predicted.

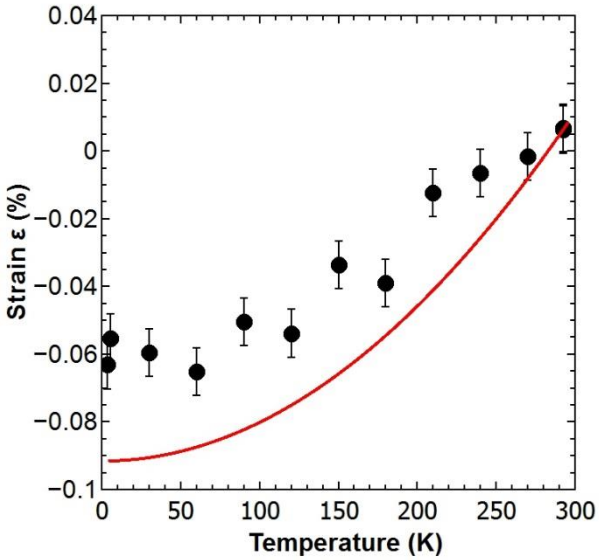

Figure 5-20: Strain dependence and predicted strain of the contacted sample from section 5.1.1 (figure 5-11 (b)) with the theoretical strain dependence (red) shifted to coincide with the room temperature data points.

In this case, it would be expected to observe a range of strain dependences due to the different starting point of sample-substrate conformity. A lower strain gradient than theory at higher temperatures would be expected while the graphene is transitioning from semi-suspended to full contact with the substrate. This behaviour could be seen in the contacted sample, shown in figure 5-20, where the theoretical and measured strain deviate immediately from the room temperature start point. Also, observing figure 5-11 (b) shows a good conformity of results with the theory at the low temperature range suggesting the divergence happens near the start of the cooling process.

This model of strain variation can be used to estimate the surface roughness of the SiO_2. Assuming the graphene reaches a fully conforming state with the SiO_2 surface, the difference in the total change in strain over the entire temperature

range between the theory and measured values is used to calculate the depth of the surface features. Graphene is expected to act as a membrane when placed on a rough surface, so greater contact and adhesion is expected on the peaks of a rough substrate and gaps caused by imperfect contact is expected at the troughs in between them.[2,3,25,89] The graphene expansion on the SiO_2 was modelled as the difference between the chord and arc length of a circle segment, as shown in figure 5-21, where the relation between the chord length, c, arc height, h, and arc length, s, is approximated as:[91]

$$s \approx \sqrt{c^2 + \frac{16}{3}h^2}. \quad (5.5)$$

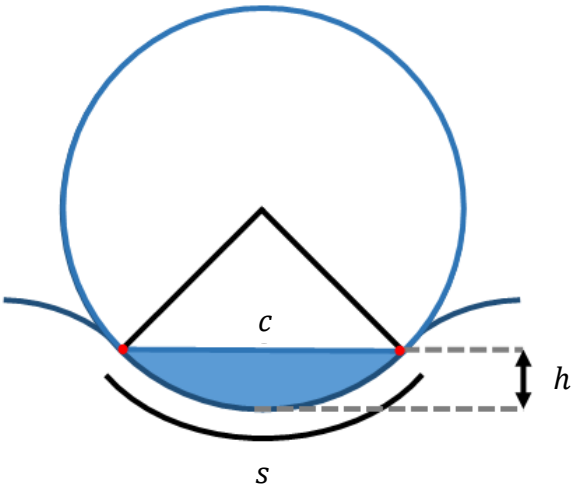

Figure 5-21: Segment of a circle with the chord length, c, the arc length, s, and segment height, h, as labelled. In this model, the graphene is pinned above the red points and separated from the substrate below it. It then expands to fill the entire arc length when decreasing temperature.

The graphene starting position is along the chord of the circle, which can be found by looking at the peak separation of SiO_2 surfaces from AFM measures.[83,89,90] These investigations reveal that an SiO_2 surface consists of undulating peaks with a period between 25 and 50 nm, as shown in figure 5-22. The chord and arc length difference is equated to the unstrained expansion of graphene. This is taken from the strain difference between the theory and measurements at 0 K,

such as in figure 5-20. The average difference in strain at 0 K of the initial three samples (section 5.1.1) is 0.034 ± 0.0014 %, giving a segment/roughness depth, h, between 0.286 ± 0.005 nm and 0.57 ± 0.01 nm for a chord length, c, defined as the roughness period of 25 to 50 nm.

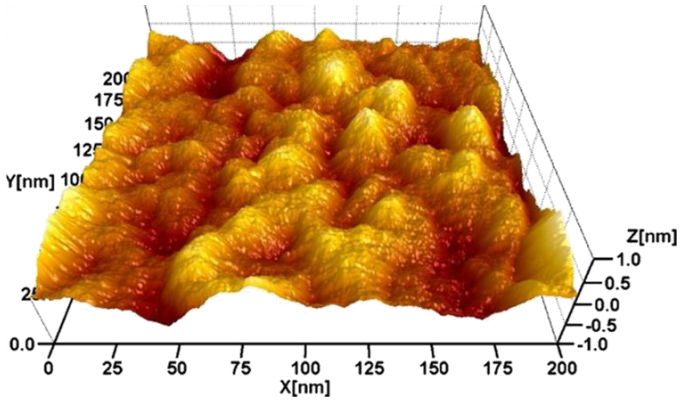

Figure 5-22: AFM Surface profile of a Si/SiO_2 substrate surface, as measured by Geringer et al.[90]

This predicts a roughness depth 0.0114 ± 0.0002 times the separation between surface peaks. This strain model is consistent with the range of surface heights of SiO_2 surfaces as measured by AFM, which find a standard deviation in the surface roughness of 0.4 nm.[83,89,90]

5.1.9 Doping

The monolayer graphene samples exhibited inconsistent doping dependences, this is seen qualitatively by comparing figure 5-9, where the data depicts a constant but unchanging doping with temperature with figure 5-10 in which the sample not only has a different room temperature doping amount, but a variable doping with temperature. The differences in room temperature doping is caused by differences in manufacture, a combination of random substrate doping and contaminants from the manufacturing processes, as described in chapter 4. The variance of the doping with temperature is considered to be a measure of the

electrical contact of the graphene: a low resistance contact allows free movement of electrons into the reservoir of the attached gold (figure 5-1), keeping the charge density of the whole system constant for small changes in graphene doping. For a doping dependence to be seen, the electron density would have to be constrained only to the graphene flake by a poor electrical contact with high resistance. This, however, does not explain why there are uncontacted graphene samples that exhibit no doping dependence, such as figure 5-9 (a).

Doping is investigated further in section 5.5 to establish the range of doping concentrations across all sample types, and to determine if there are any coincidences in the samples that exhibit any doping dependences.

5.2 Bilayer graphene

Since the strain and doping behaviour of bilayer graphene is not expected to differ greatly from the monolayer case, the same methods of determining the monolayer strain and doping can be easily converted to the bilayer case. The same measurement methods were used as in the monolayer case, and the same three types of samples: uncontacted, contacted and nailed are investigated

A bilayer graphene flake with top contacts, shown in figure 5-23 is used here to demonstrate the differences between the monolayer and bilayer graphene analysis processes.

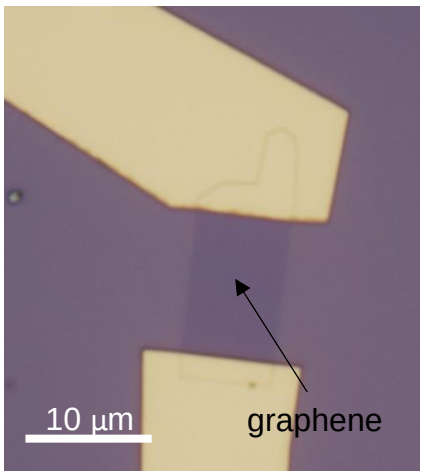

Figure 5-23: Bilayer Graphene sample with gold top contacts partially covering the upper and lower sections of the flake.

5.2.1 Raman spectroscopy

As with the monolayer devices, the bilayer sample was measured using method 1, in 30 K temperature steps and a 20 minute waiting time delay before measurements.

The bilayer sample in figure 5-24 clearly shows a broader 2D peak, at 43 cm^{-1} FWHM, than the monolayer case, figures 5-2 to 5-4. The broadening is caused by the expected separation in energy of the four sub-peak Raman transitions (section 2.3.1). While the G peak FWHM of 13 cm^{-1} does not match the sample in section 5.1.1, it is not expected to be dependent on number of graphene layers.[61] The wider bilayer G peak is therefore caused by a lower doping in comparison to the given monolayer examples, which is demonstrated during the correlation analysis.

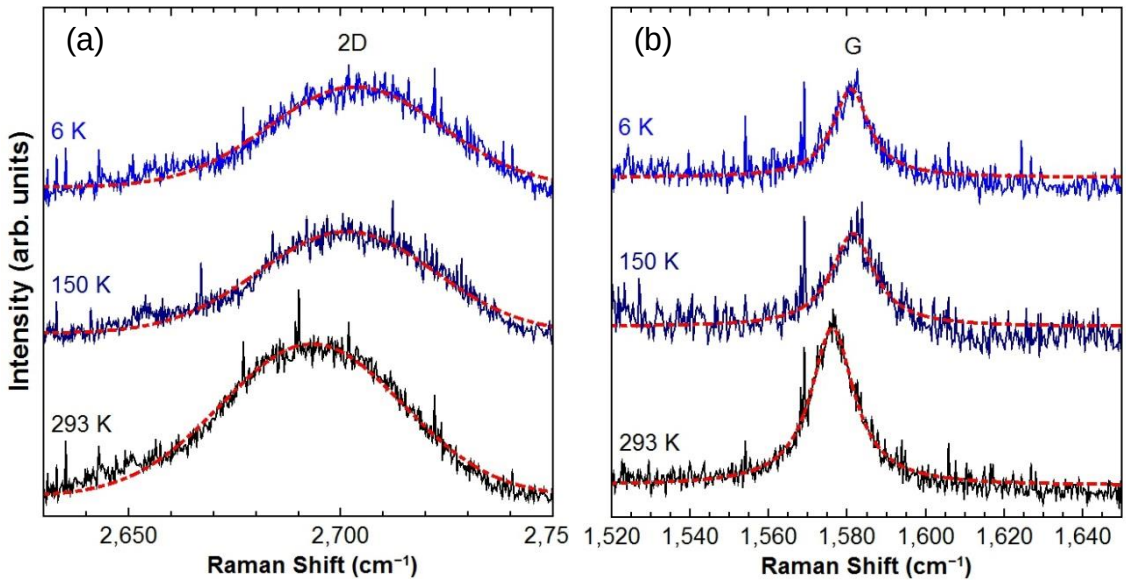

Figure 5-24: 2D (a) and G (b) peaks of the bilayer graphene sample as temperature is changed from 296 K down to 6 K. The red dashed lines show the Gaussian functions which were fit over the 2D peaks, and the Lorentzian functions which were fit over the G peaks.

The 2D peak intensity is now comparable to or greater than the 2D peak intensity compared to the monolayer case. The peaks all show an increase in Raman shift energy with decreasing temperature without a distinct splitting or broadening of the G and 2D peaks, and in the 2D case, sub-peak dispersion. This is consistent with the bilayer sample increasing in biaxial strain in the same manner as seen in section 5.1. The general decrease in the intensity with temperature of both peaks is attributed to the accuracy of the laser on the sample being reduced by vibrations and temperature fluctuations when the experiment is running, which is exacerbated as sample size decreases.

5.2.2 Temperature dependence of peak position

The peak position of the G peak was again obtained by fitting with a Lorentzian function (5.1). The 2D peak was not fit with four Lorentzian functions for each sub peak and combined, but fitted with a single Gaussian function,

$$y = Aw\sqrt{\frac{2}{\pi}}e^{-2\left(\frac{x-x_0}{w}\right)^2}, \quad (5.6)$$

where the variables hold the same values as equation (5.1) which proved to be a superior fit for the peak shape. This proved sufficient as only the peak shift is used for strain dependence and the sub peaks remain consistent with respect to each other throughout the experiment. In order to create a two-axis correlation plot, a single position value of the 2D peak was required. The results in figure 5-25 come from two measurement runs of the contacted bilayer sample.

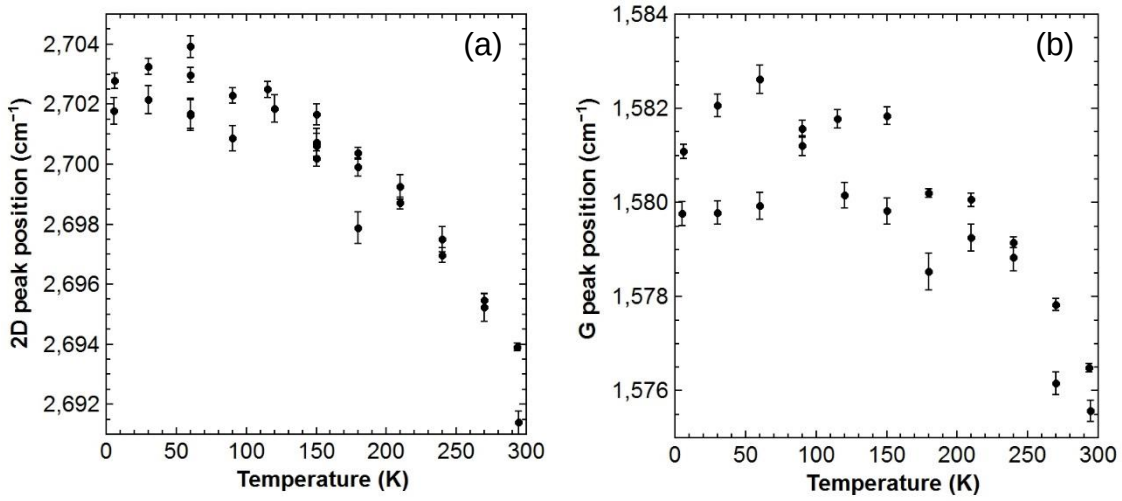

Figure 5-25: Contacted bilayer graphene 2D (a) and G (b) peak position with changing temperature.

There is a greater point scatter of the 2D and G peak position shift with temperature attributed to the lower signal to noise ratio of the measurements. The larger uncertainty bounds are also caused by this, and from fitting a Gaussian to an asymmetric peak in the 2D case. The dependence of the peak positions on temperature is comparable to the monolayer case. The peak dependences

display similar magnitudes of shift, 8-11 cm^{-1} for the 2D peak, and 4-6 cm^{-1} for the G peak, and follow a similar gradient dependence to the monolayer peak shift.

5.2.3 Correlation method

The correlation method used to separate the strain and doping peak shift contributions for monolayer graphene must be modified to be used for bilayer graphene. The gradient of the strain line, ε_{exp}, doping lines, n, and the position of the neutrality point must all be re-defined for bilayer graphene.

The new 2D/G ratio of the strain gradient of 2.4 ± 0.13 was calculated from the measured 2D and G peak shift with strain percentage, taken as the average of biaxial strain induced by flexible substrates and pressurised graphene bubble measurements.[15,44] This value is comparable to the monolayer strain gradient as the peak shift ratio is not expected to be significantly different. Taking the 2D peak value as a single peak in this case is valid as the 2D sub peaks are shown to have the same variation with strain as each other.

The 2D/G ratios of the doping gradient of $n_h = 0.62 \pm 0.09$ and $n_e = 0.4 \pm 0.25$ were derived from Raman-doping measurements taken from top-gated bilayer measurements.[95] This doping dependence is comparable to the monolayer case, and the variation in the measured gradients for strain and doping are due to the experimental uncertainty.

As in the monolayer case, the zero strain-doping neutrality point was taken from a suspended graphene flake measurement. The suspended bilayer 2D peak has been measured at 2621.4 ± 0.9 cm^{-1} using 632 nm wavelength laser, which must be shifted due to the 2D peak energy dispersion (section 2.3.1) to the equivalent 514.5 nm laser: 2669.2 cm^{-1}.[59,103] The G peak shift is also measured at

1567 ± 1 cm^{-1}.[103] The 2D doping shift and neutrality positions were measured with Gaussian function fitting to obtain their peak positions consistent with the methods used for sample data measurements.

The anharmonic phonon shift component in bilayers was taken to be similar to the monolayer case, the G peak phonon behaviour being the same for both cases. The strain and doping shifts of the contacted bilayer sample are then separated using these new values.

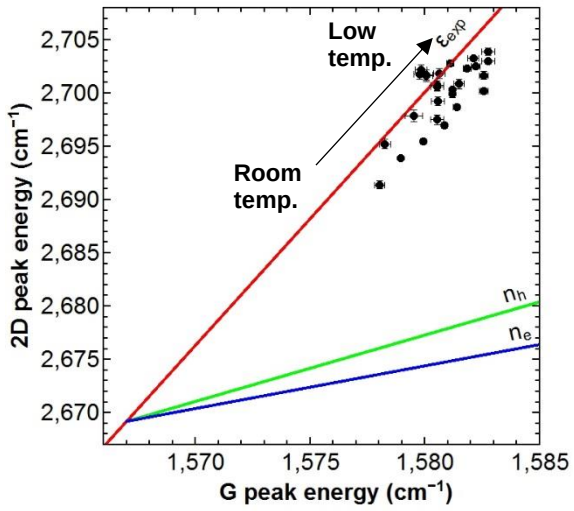

Figure 5-26: 2D – G peak correlation of the contacted bilayer graphene sample. ε_{exp} is the red zero-doping strain correlation, n_h is the green zero-strain hole-doping correlation, and n_e is the blue zero-strain electron doping correlation.

The bilayer sample shows the same temperature trend as the monolayer case, but with a much higher starting position along the strain line, and very little doping. In figure 5-26, there is a starting compressive strain that is much larger than the starting strains of the monolayer samples. The compressive strain then increases with cooling as expected. The data suggests a very low, constant doping with temperature because the points fall very close to the strain line. This room temperature strain offset is persistent through all bilayer results, therefore the most likely cause of this is that the measured strain-doping neutrality point is not

truly free from strain and doping contributions. There is no mechanism for bilayer graphene to be consistently strained by a SiO_2 substrate in ambient conditions where monolayer graphene would not also be similarly strained. Despite this, the strain gradient with temperature will still be correct, while the absolute value of strain will be incorrect, which will still allow for the correct value of TEC to be calculated.

5.2.4 Strain and TEC

The G peak Grüneisen parameter for bilayer graphene is similar to the monolayer case, measured within experimental uncertainty of each other, with a bilayer G peak strain-shift ratio of 57.2 cm^{-1}/%. The strain dependence is then fitted:

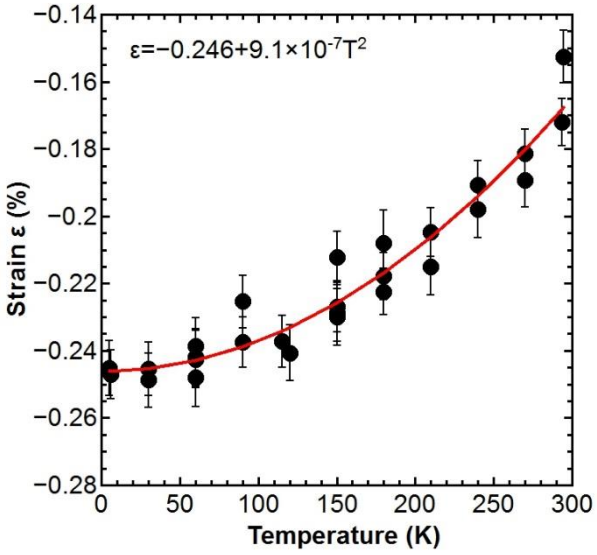

Figure 5-27: T^2 fit (blue) of the contacted bilayer strain of figure 5-26.

The strain in figure 5-27 exhibits the same dependence and gradient as monolayer graphene. As expected from the correlation analysis, the sample appears to start at a much higher compressive (negative) strain at room

temperature. The TEC dependence is then calculated across all samples, shown in figure 5-28.

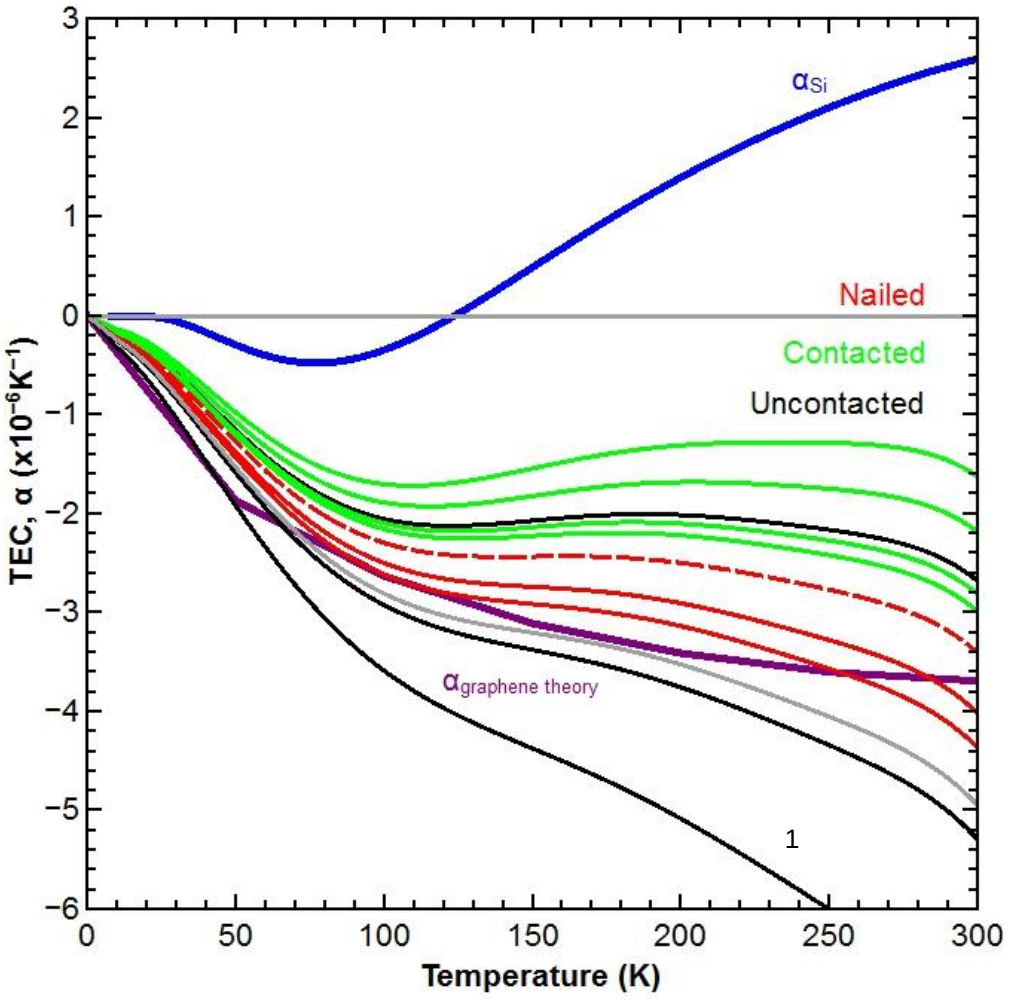

Figure 5-28: TEC dependence of all bilayer samples, showing all sample types: uncontacted (black), contacted (brown) and nailed (red). The contacted bilayer example is shown as a dashed line. The TEC of silicon is in blue and the monolayer graphene TEC is show again in purple.[20,93] An anomalous TEC result is marked as "1", and its corrected position is plotted in grey.

This distribution of results is comparable to that of monolayer graphene with some notable differences. The first difference is that the distribution shows a much larger variation than the in the monolayer case. The second is that the distribution tends slightly lower than the monolayer TEC distribution, with some samples having a more negative TEC than the monolayer graphene theory. As with

monolayer graphene, the magnitude of the individual sample variation is much greater than the differences between the samples, therefore the theoretical result that bilayer graphene is expected to have a less negative TEC dependence is not resolved.

The most negative TEC result, the uncontacted measurement marked “1” in figure 5-28 is anomalous and is caused by an artefact of the TEC calculation as defined in the monolayer section. The lowest temperature measurement of uncontacted “1” is abnormally lower than the points around it. Therefore, when the fitting algorithm uses this point as its starting position, the final gradient is incorrectly exaggerated. By instead using the second lowest temperature measurement, a greater accuracy fit can be achieved. The differences are shown in figure 5-29, and the corrected plot is shown in figure 5-28 in grey. For all further calculations, the fit obtained from figure 5-29 (b) is used in place of the fit of figure 5-29 (a).

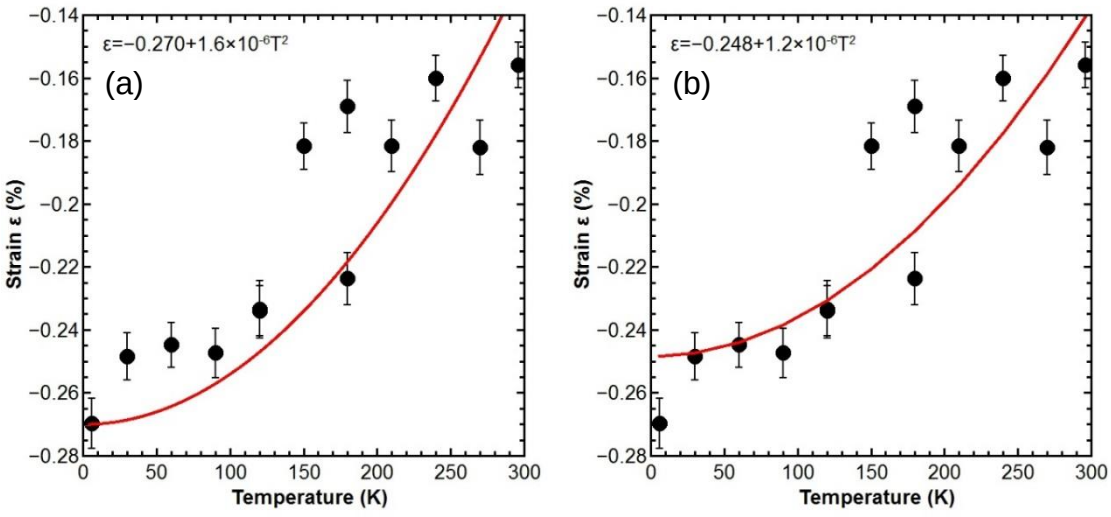

Figure 5-29: (a) Abnormal strain fit of uncontacted “1” from figure 5-28 and (b) modified strain fit.

5.3 Tri-layer graphene

The methods to extend monolayer strain analysis to bilayer graphene are also used to analyse tri-layer graphene. The same three types of sample contacts and measurements performed for monolayer and bilayer graphene were used. As with bilayer graphene, a contacted tri-layer sample, shown in figure 5-30, is used to demonstrate the differences in the analysis method required to obtain the strain variance.

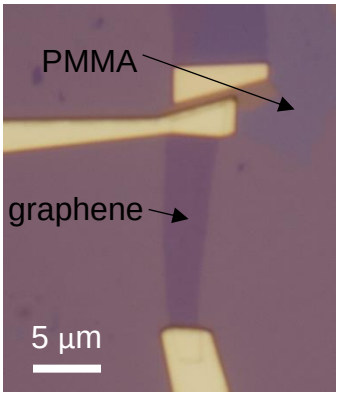

Figure 5-30: Tri-layer graphene sample with gold top contacts partially covering the upper and lower sections of the flake. Only the lower graphene sample was used due to the insoluble PMMA residues on the upper flake.

5.3.1 Raman spectroscopy

Measurement method 1 was again used, with steps of 30 K and a measurement delay of 20 minutes. The laser from section 3.7 was used at 3 mW power output, with an exposure time of 5 minutes per spectrum.

The G and 2D peaks from figure 5-31 show the same increase in Raman shift energy with decreasing temperature as monolayer and bilayer graphene, maintaining consistency with biaxial strain. The 2D peak shows a continued increase of FWHM with layer number, to ~53cm^{-1}, while the G peak FWHM of

~13cm^{-1} suggests a low doping level, as per the bilayer sample of section 4.2.1. The trend of increasing G peak intensity compared to 2D peak intensity with number of graphene layers continues as expected.[61] The behaviour of peak intensity being reduced below room temperature is observed again, an artefact of the experimental setup (section 5.2.1).

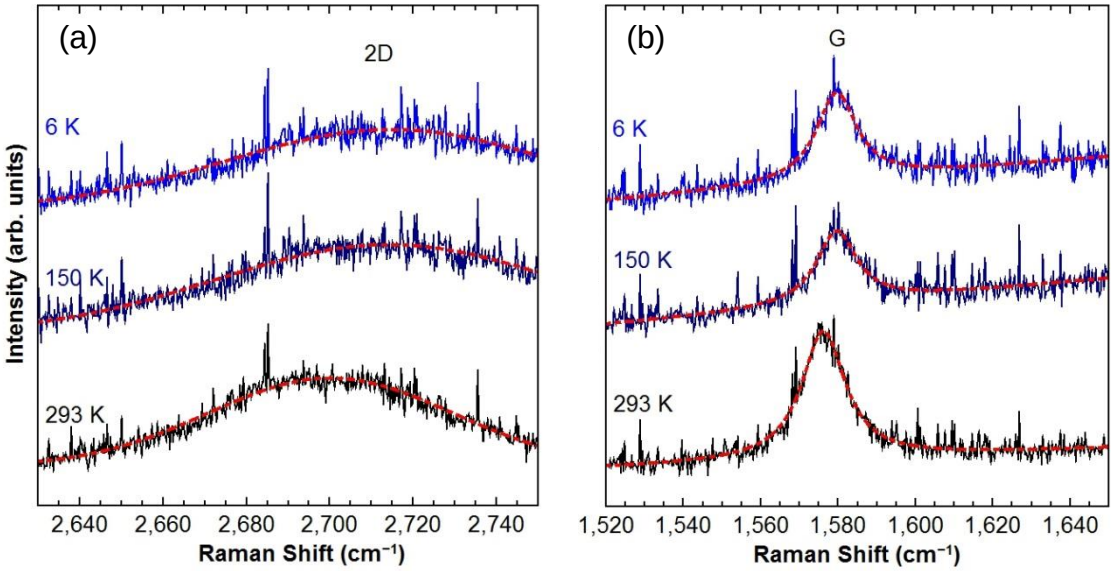

Figure 5-31: 2D (a) and G (b) peaks of the tri-layer graphene sample as temperature is changed from 296 K down to 6 K.

5.3.2 Temperature dependence of peak position

The G and 2D peaks were fitted with Lorentzian and Gaussian functions in the same manner as the bilayer samples in section 5.2.2, and compared to monolayer and bilayer samples as a function of temperature.

As expected, the temperature dependence of the tri-layer Raman peak positions in figure 5-32 follows the same increase in peak energy with decreasing temperature as the monolayer and bilayer cases, achieving similar magnitudes of shift of ~10.5 cm^{-1} for the 2D peak and ~5 cm^{-1} for the G peak.

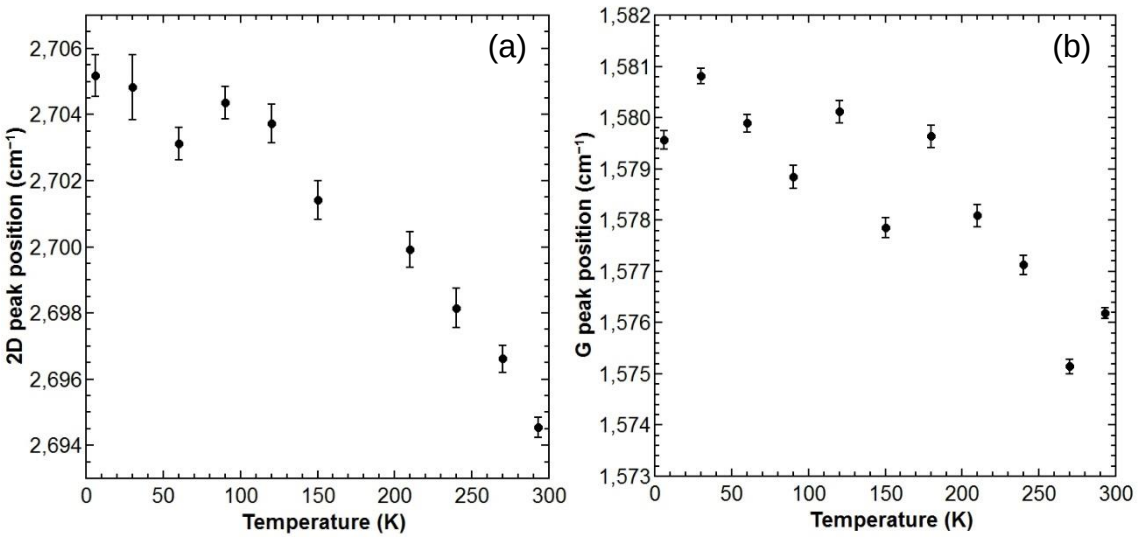

Figure 5-32: Contacted tri-layer graphene 2D (a) and G (b) peak position with changing temperature.

5.3.3 Correlation method

In the same manner as section 5.2.3, the strain line, doping line and neutrality point were re-calculated in order to adjust the correlation method to correctly separate strain and doping contributions for tri-layer graphene.

The tri-layer 2D/G ratio of the strain gradient was measured to be 2.51 ± 0.3, similar to the monolayer and bilayer strain gradient.[15] The 2D peak value was again taken as a single peak position from the Gaussian fit, as the 2D sub peaks have the same strain shift as each other. The previous bilayer doping 2D/G ratio of 0.62 ± 0.09 (from 5.2.3) was used for the tri-layer correlation. This is due to the absence of a Raman measurement of top-gated tri-layer graphene as with the monolayer and bilayer techniques. Therefore the bilayer doping shift was used as it is would be closest to the tri-layer doping shift. This is additionally justified as measurements of the monolayer and bilayer doping gradients are comparable within uncertainty, and uncertainties in the doping gradient do not contribute significantly to the uncertainty in strain.

The zero strain-doping neutrality point was taken from a suspended tri-layer graphene flake measurement.[103] The 2D peak has been measured as 2621 cm^{-1} using 632 nm wavelength laser, which is corrected for the 2D peak excitation dispersion (section 2.3.1) to 2669.2 cm^{-1} at 514.5 nm.[59,103] The G peak shift has been measured as 1567 cm^{-1}.[100] The measured 2D doping shift and neutrality position were also fitted with Gaussian functions to obtain peak positions consistent with the sample data of figure 5-31.

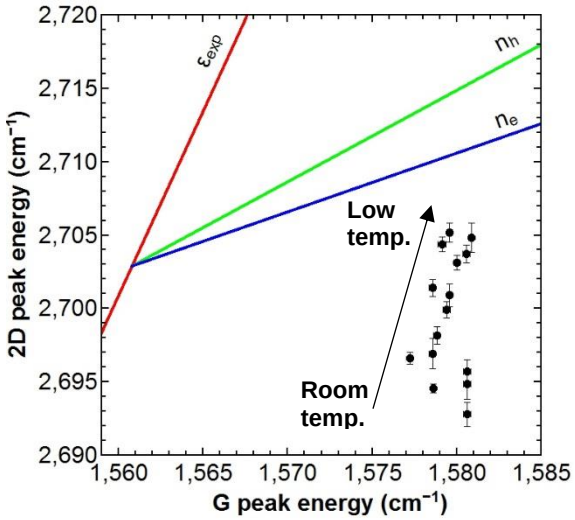

Figure 5-33: 2D – G peak correlation of the contacted tri-layer graphene sample. ε_{exp} is the red zero-doping strain correlation, n_h is the green bilayer hole-doping line, and n_e is the blue bilayer electron-doping line.

As expected, tri-layer graphene shows the same temperature trend as monolayer and bilayer (figure 5-33). However, tri-layer graphene shows a starting tensile strain at room temperatures across all samples. Additionally, the tri-layer G peak FWHM is consistent with low doping levels (section 2.3.4), but the correlation in figure 5-33 shows a significant doping as the data has a large doping vector component, n_h. The results show that monolayer, bilayer and tri-layer graphene all claim a different and inconsistent room temperature strain value. These inconsistencies are attributed to an incorrect measure of the neutrality point, and

reinforce the suggestion made in section 5.2.3 that this is also the case for bilayer graphene. This particular sample also shows a discernible doping dependence with temperature, indicated by the correlation line of figure 5-33 not aligning parallel to the strain line.

5.3.4 Strain and TEC

With a tri-layer G peak strain-shift ratio of 45.7 cm^{-1}/%, the strain dependence is then fitted as per mono and bilayer graphene, shown in figure 5-34.[15] As observed in the correlation plot, the tri-layer samples appear to have a tensile (positive) strain at all temperatures, caused by the neutrality point error. The strain increases towards a compressive (less tensile) strain as the temperature is reduced. Given that the TEC is only dependent on gradient, it can still be correctly calculated across tri-layer graphene samples.

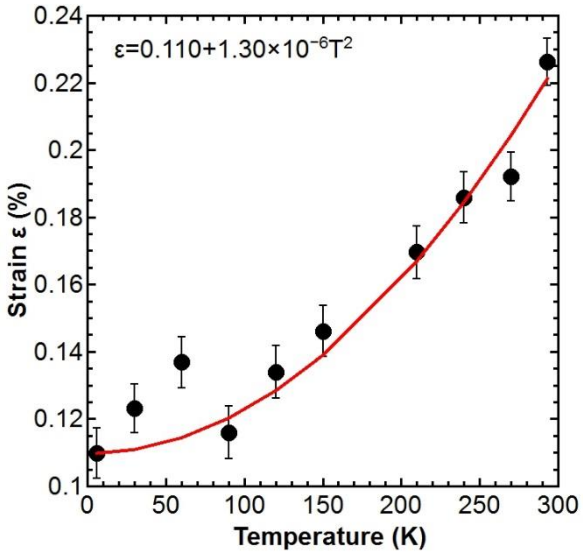

Figure 5-34: T^2 fit (blue) of the contacted tri-layer strain of figure 4-33.

The distribution of TECs in figure 5-35 is similar to monolayer and bilayer graphene: a scatter of results between a TEC of zero and the graphene monolayer theory. The tri-layer graphene TECs also show a similar scatter to

bilayer graphene samples, continuing greater individual sample variation than variation due to graphene thickness or contact type.

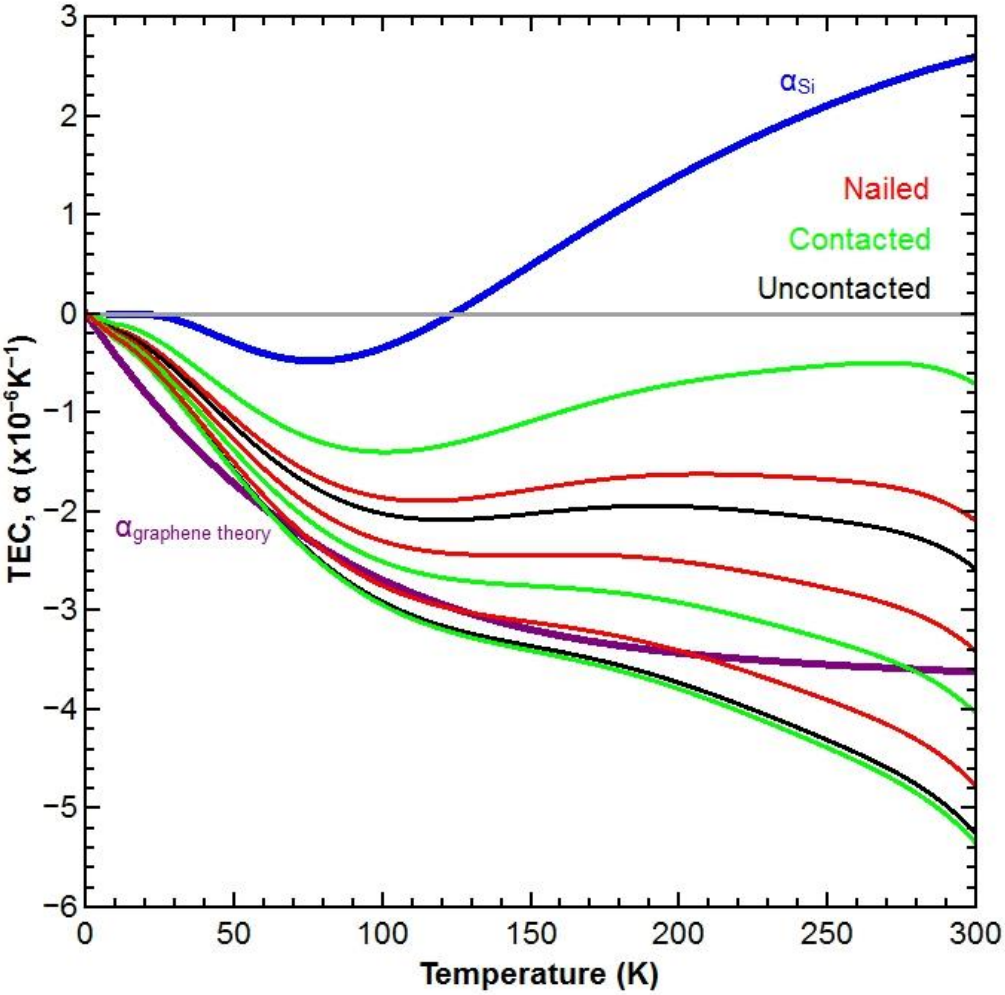

Figure 5-35: TEC dependence of all trlayer samples, showing all sample types: uncontacted (black), contacted (green) and nailed (red). The contacted tri-layer example is shown as a dashed line. The TEC of silicon is in blue and the monolayer graphene TEC is show again in purple.[20,93]

5.4 Comparison of thermal expansion coefficient with number of layers

The average TEC dependences for monolayer, bilayer and tri-layer graphene are compared to each other and the theoretical TEC in figure 5-36.

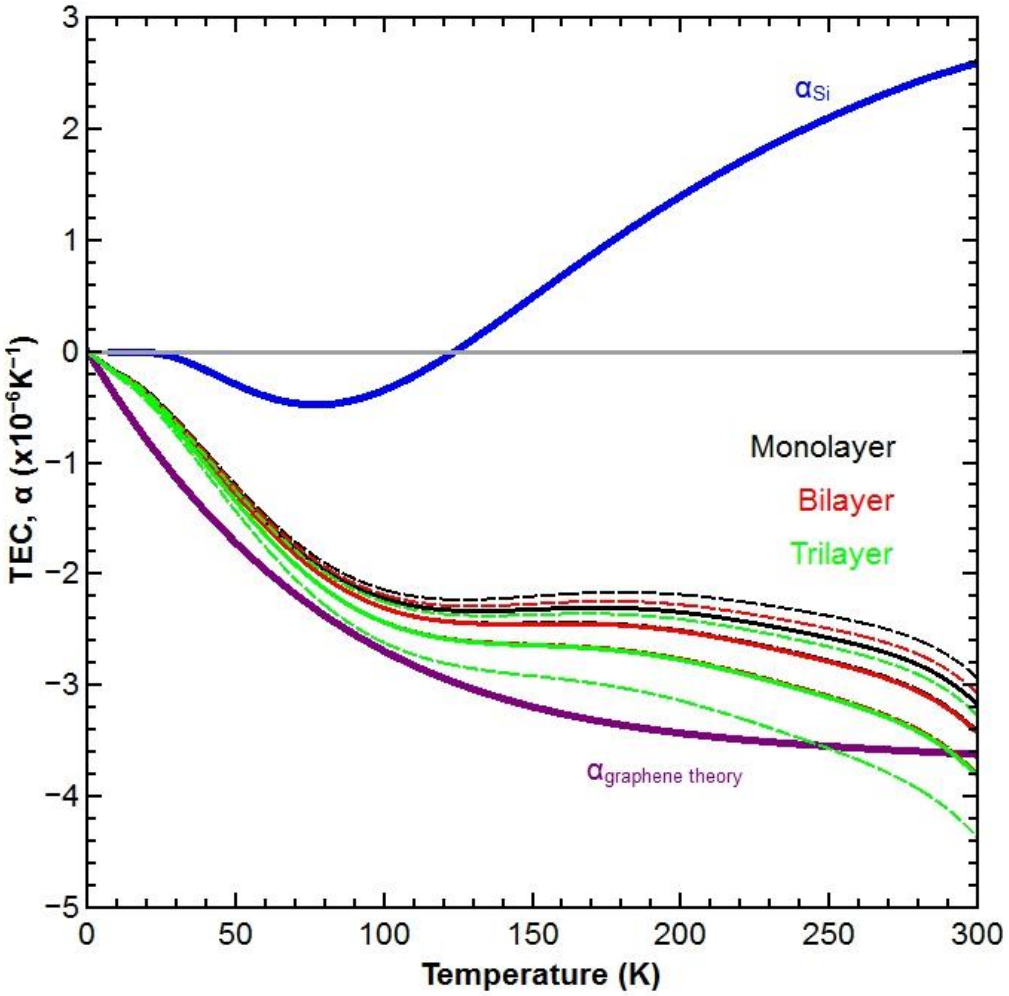

Figure 5-36: Average of TECs for each flake thickness, monolayer (black), bilayer (red) and tri-layer (green). The dashed lines mark the uncertainty bounds. The TEC of silicon is in blue and the monolayer graphene TEC is show again in purple.[20,93]

While the graphene TEC dependence with temperature appears to trend more negative with increasing graphene thickness, the significant overlap of the uncertainty bounds means this conclusion cannot be made with confidence. A decreasing dependence would also be contrary to the prediction of graphene TEC with layer number in section 3.2, of a less negative TEC with increasing layer number.[94]

As far as the precision of this study can determine, the TEC of all three graphene thicknesses are of similar magnitude with a 300 K value between $–3.2x10^{–6}$ $K^{–1}$ and $–3.8x10^{–6}$ $K^{–1}$. While this is less negative than the theoretical monolayer TEC, this is to be expected in samples that do not transfer 100% of the TEC mismatch into strain, skewing the average. Therefore, these results are considered to generally agree with the theoretical TEC value, and in disagreement with previous measurements of graphene TEC, which find much larger magnitude, negative TECs.[16-19]

5.5 Doping

The correlation method of separating strain and doping shifts allows for a parallel analysis of the doping concentrations and dependences of the samples along with strain. This section examines the results given by this correlation doping analysis. These results were highly inconclusive so were then compared to alternate means of calculating graphene doping from optical measurements, using the G peak FWHM and 2D and G peak area ratio dependencies.

5.5.1 Correlation doping

In order to determine the doping-only shift of the Raman peaks, the correlation shift from section 5.1.4 is performed the other way around. The points are shifted along the correlation strain gradient to reach the n_h doping line. The Raman measurements of top gated graphene devices from section 2.3.4 are then used to relate these doping shifts to a concentration, n.[68,70,95] This was used to calculate doping values for the monolayer and bilayer graphene devices, assuming hole doping as described section 5.1.3. A fit of the measured peak shift with doping for monolayer graphene, from figure 2-19, was taken to be

$$\Delta\omega_{G_{mono}} = 1.425n - 0.0274n^2, \qquad (5.7)$$

where ω_G is the position of the G peak in cm^{-1}, and n is the hole concentration in 10^{12} cm^{-2}.[47,70] A fit of bilayer peak shift dependence was performed on an equivalent measurement by Das *et al.*:[95]

$$\Delta\omega_{G_{bi}} = 0.38n - 0.11n^2. \qquad (5.8)$$

The tri-layer device doping was not calculated as the requisite peak dependence is not in the literature.

According to the correlation shifts, the 12 monolayer and 7 bilayer graphene devices displayed a range of doping levels at room temperature between 1.4x10^{12} cm^{-2} and 6.3x10^{12} cm^{-2}, where values below 1.4x10^{12} cm^{-2} cannot be measured using this method.[35] One monolayer and one bilayer sample exhibited doping values below this lower limit. The average doping concentration is (4.7 ± 0.5)x10^{12} cm^{-2} and (3.9 ± 0.4)x10^{12} cm^{-2} for monolayer and bilayer graphene respectively. The two outlying samples were counted as being equal to the lower limit of 1.4x10^{12} cm^{-2} for this calculation. This range of values is

consistent for graphene devices manufactured according to the methods of chapter 4. There is no variation that correlates across the different device designs from section 4.7. The monolayer and bilayer graphene doping results being comparable is unexpected as bilayer graphene is predicted to exhibit half the doping concentration under the same conditions as monolayer graphene.[95] This would indicate that the calibration measurement has a finite doping, causing a zero-error in the bilayer correlation method of section 5.2.3.[103]

There is also a dependence on doping with temperature exhibited in 5 of the 19 samples, with these samples exhibiting a decrease in doping as the temperature is reduced while the rest show no dependence. This sample subset covers all three styles of contact configuration. This dependence has a Δn of 2.4–4.6x10^{12} cm^{-2} between the highest and lowest temperature in the samples that exhibit it. The average Δn is (2.9 ± 0.3)x10^{12} cm^{-2}, giving a significant contrast between the incidences of doping dependence and no dependence. In order to determine the specific cause of the doping shift, a range of new device designs may have to be considered in order to deliberately induce the phenomenon.

For a confirmation of the doping assumption made in section 5.2.3, the difference in strain between electron and hole doping was investigated. Since the optical determination of doping (positive or negative) was not possible, the calculation was performed twice on the same data set, one assuming hole doping, the other electron doping. This allowed the error caused by assuming the wrong doping type to be determined.

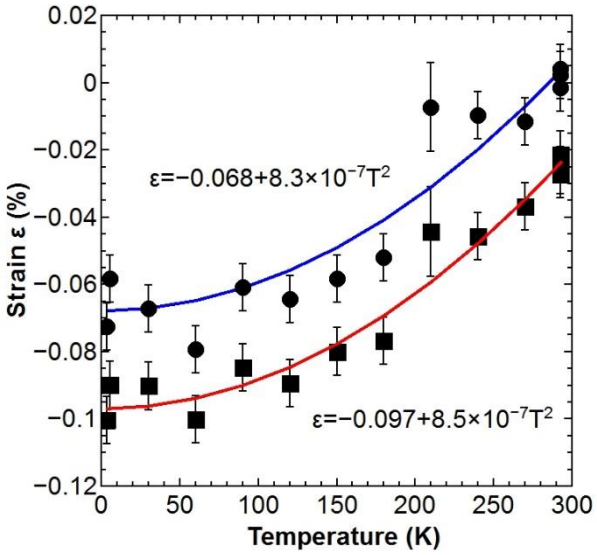

Figure 5-37: Comparison of strain dependence assuming hole (circles) or electron (squares) doping mechanisms, using the "uncontacted" sample data from figure 5-10 (a). The hole (electron) fit equation is displayed above (below) the data set.

Figure 5-37 demonstrates that assuming the incorrect doping mechanism only results in an offset in strain magnitude. Every data point is shifted by 0.025-0.03 % between the electron and hole doping scenarios. This does not result in a significant difference between the fit gradients of the two doping types and both are within the uncertainty range of each other, being $\pm 0.5 \times 10^{-7}$ % K^{-1} and $\pm 0.3 \times 10^{-7}$ % K^{-1} for the hole and electron doping fits respectively. Therefore, even if the doping assumption made in section 5.1.3 was incorrect, the resultant error in TEC will be insignificant compared to the peak position and fit errors.

5.5.2 G peak FWHM doping

As described in section 2.3.4, lower doping levels in graphene cause a broadening of the Raman G peak. This was used as an alternate measure of the doping due to the lack of doping consistency of graphene samples when using the peak shift correlation method. The hole-concentration dependence of the G

peak FWHM of monolayer graphene from figure 2-21 was fit with a third order polynomial:[70]

$$n = 200 - 44.7w_{G_{mono}} + 3.36w_{G_{mono}}^2 \pm 0.0840w_{G_{mono}}^3, \qquad (5.9)$$

which is valid for a doping concentration between 0 cm^{-2} and 15x10^{12} cm^{-2}, where n is the doping concentration in units of 10^{12} cm^{-2} and w is the FWHM in cm^{-1}. Bilayer graphene was similarly fit from a study by Das *et al.*[95] A second order polynomial was sufficient to sufficiently fit the data set in this case:

$$n = 25.6 - 3.02w_{G_{bi}} + 0.0886w_{G_{bi}}^2, \qquad (5.10)$$

and is valid in the range between 0 cm^{-2} and 9x10^{12} cm^{-2}. The monolayer and bilayer doping results from this method are consistently higher than from the correlation calculation, spanning the whole discernible range of doping values from ~0 cm^{-2} to 15x10^{12} cm^{-2} for monolayers, and between ~0 cm^{-2} and 9x10^{12} cm^{-2} for bilayers. The average values are 12x10^{12} cm^{-2} for monolayers, and 6x10^{12} cm^{-2} for bilayers. In this method, there is a lower limit to FWHM values, for example, values of 7-8 cm^{-1} in figure 2-21 can have any doping value ≥ 15x10^{12} cm^{-2}. Therefore, for the average calculations, FWHM values in this range were taken as the minimum value of 15x10^{12} cm^{-2}, and likewise the bilayer minimum of 9x10^{12} cm^{-2}. There is now a factor of two difference for bilayer graphene, which agrees with the expectations from section 3.2, supporting the conclusion of a zero-error in the correlation method. There is a large uncertainty in the FWHM-doping of ± 5x10^{12} cm^{-2} due to the large point scatter in the calibration fits. The doping difference between the FWHM and correlation doping methods is large enough to be significant despite the large uncertainties involved.

Additionally, neither the G nor 2D peak FWHM has any significant or consistent temperature dependence within uncertainty bounds. This could mean that the dependence seen by the correlation method is an error in the method, or that the FWHM uncertainty is too great to observe the slight dependence claimed in the correlation doping.

5.5.3 Peak ratio doping

To resolve the differences in findings between the correlation and FWHM analysis methods, a peak ratio comparison between the Raman 2D and G peaks was performed using the ratio between the graphene monolayer 2D and G peak areas (A_{2D}/A_G) as a function of doping as measured by Basko *et al*.[75] An exponential decay function provided the best fit, given by R^2 values:

$$n = 54.3e^{-\frac{A}{1.915}}, \qquad (5.11)$$

where A is the area ratio A_{2D}/A_G. In this case, the doping concentrations in the monolayer samples ranged from $0.8\text{x}10^{12}$ cm^{-2} to $11\text{x}10^{12}$ cm^{-2}. The lowest doping concentration has a similar value to both the correlation and FWHM methods, and the highest doping concentration lies between that of the other two methods. The average sample doping was $(3.8 \pm 0.8)\text{x}10^{12}$ cm^{-1}, suggesting that the magnitude of the FWHM results are not reliable. This may be justified as there is a large variance observed in previous FWHM measurements at the same doping levels, such as in figure 2-21.[61,70]

Similar to the correlation method, 4 of the 11 monolayer samples exhibit a dependence on doping concentration with temperature of the order $1\text{x}10^{12}$ cm^{-1}. However, this behaviour is not observed on the same samples as with the correlation method, have a significantly lower magnitude of doping change, and

display both increasing and decreasing dependences with temperature. It could be the case that this temperature dependence is a statistical fluctuation close to the uncertainty range. Given the similar magnitude of the dependence to the uncertainty, more precise electronic measurements are required to determine both if the phenomenon exists and its cause.

5.5.4 Doping conclusion

There are no clear discernible doping concentration values or trends across these three analysis techniques. This is likely due to the large uncertainty ranges allowing agreement within these ranges while providing values with a factor of three difference between each other. This highlights the necessity of using non-optical measurement techniques to reliably determine doping concentrations.

5.6 Graphene on h-BN

A preliminary study into the effects that different substrates have on the strain and thermal expansion properties of graphene systems has been performed. As mentioned previously in sections 2.4 and 3.3, hexagonal boron-nitride (h-BN) has the same 2D lattice structure as graphene, and even few layer h-BN can significantly flatten SiO_2 surfaces. h-BN has been shown to induce strain in graphene through forced lattice matching, and could also be expected to affect the transverse phonons and TEC of graphene.[96] Two monolayer and one bilayer graphene flakes on h-BN substrates were measured (figure 5-38), which were manufactured as described in chapter 4.

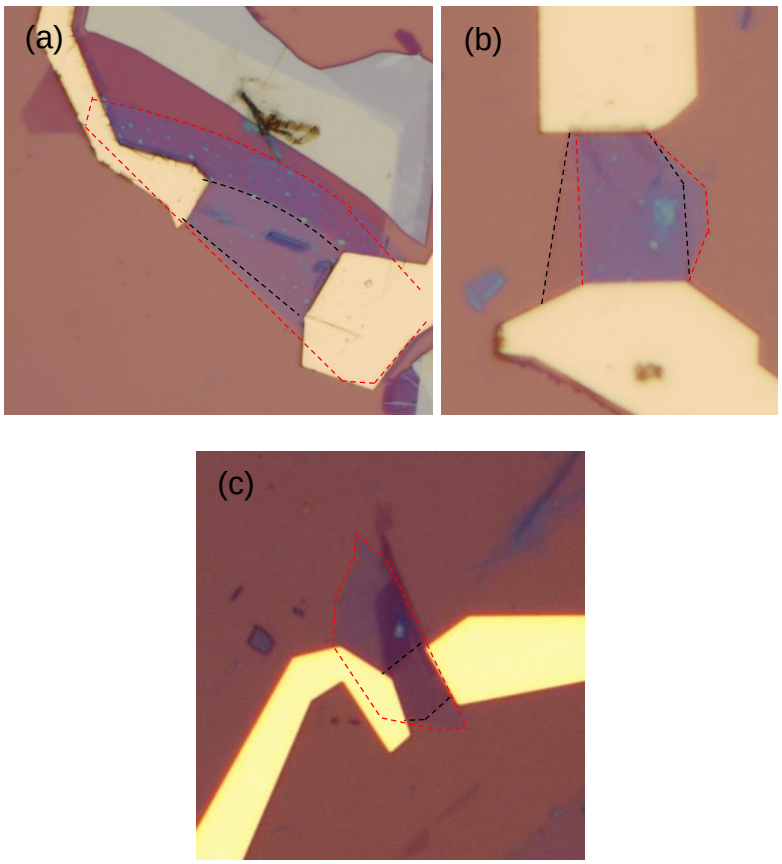

Figure 5-38: (a) and (b) monolayer graphene on h-BN. (c) bilayer graphene on h-BN. The graphene areas are outlined in black, and the h-BN areas are outlined in red.

The same measurement method as applied to previous graphene samples on Si/SiO_2 was used: method 1, described in section 5.1.1, with 3 mW of laser power and 30 K temperature steps. The strain was calculated using the correlation method of section 2.3.6, with the corresponding monolayer (section 5.1.3) and bilayer (section 5.2.3) dependences. The strain-doping separation is sown in figure 5-39.

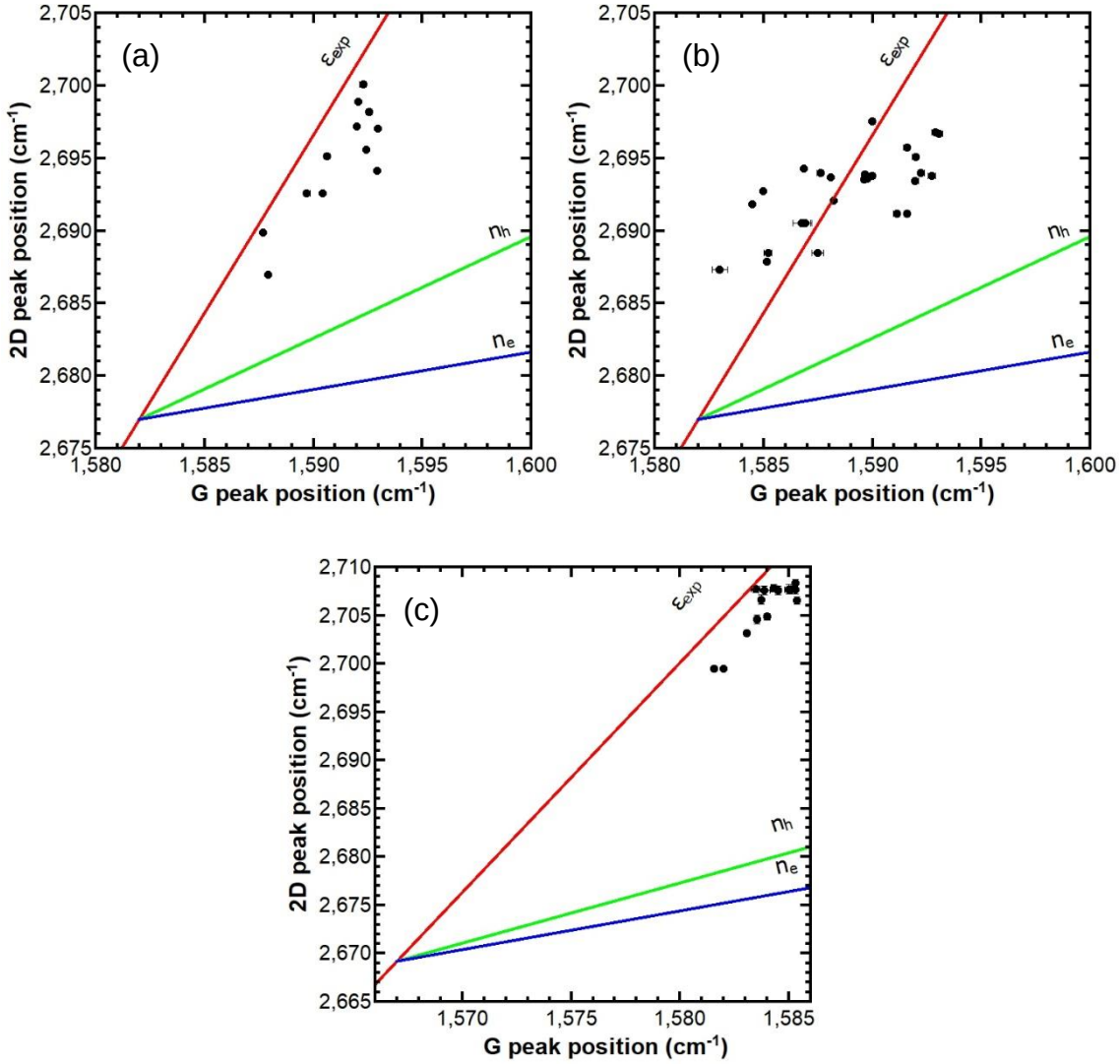

Figure 5-39: (a) and (b) correlation of Raman peak positions of monolayer graphene on h-BN, as labelled in figure 5-38. (c) correlation of Raman peak positions of bilayer graphene on h-BN. Strain-doping gradients and zero positions as used in 5.1.4 for monolayers and 5.2.3 for the bilayer.

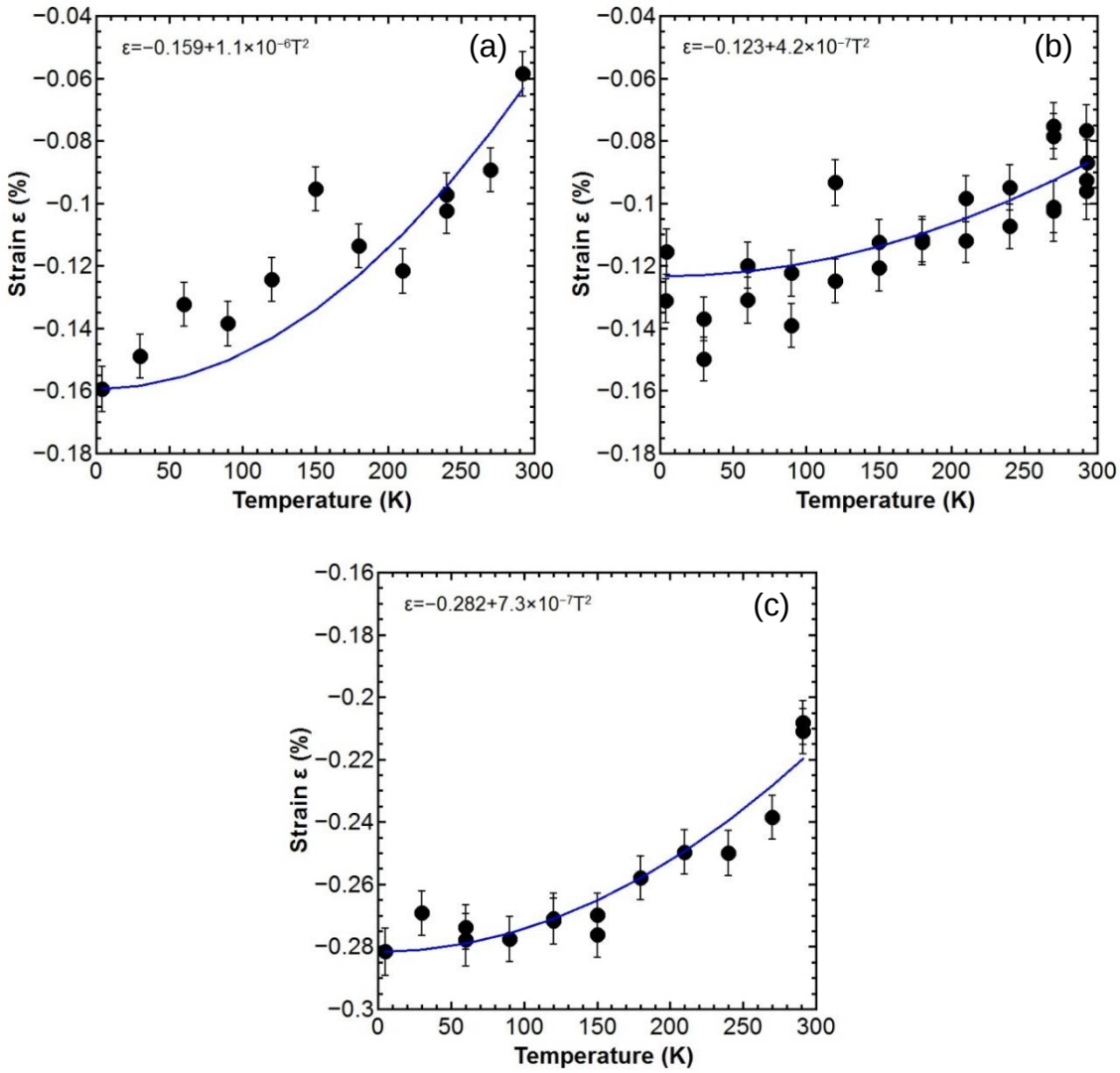

Figure 5-40: (a) and (b) strain dependence of monolayer graphene on h-BN, as labelled in figure 5-38. (c) Strain dependence of bilayer graphene on h-BN. The blue lines show the fit equations.

All h-BN substrate samples in figure 5-40 exhibit strain dependences with temperature similar to samples on SiO_2 surfaces. While the doping levels observed lie within the ranges of doping observed of graphene samples on SiO2 surfaces, there is a consistent offset in the room temperature strain between equivalent samples on h-BN and SiO_2 of 0.6-0.8 % in the compressive (negative) strain direction. This shift behaviour is similar to other observations of a –0.12 % offset, but is inconsistent with a lattice matching strain between graphene and h-BN, discussed in section 3.3.[50,96,104] The lattice mismatch of 1.7 % is far greater

than the strain difference observed. For a lattice mismatch, the strain would also be expected to increase in the tensile direction (positive) given the larger h-BN lattice, and only be compressive in the strain boundary regions (section 3.3).[96] Additionally, the 2D peak of h-BN supported samples was not observed to have an increased FWHM over SiO_2 supported samples. The average 2D FWHM of monolayer graphene on SiO_2 is 27.1 ± 0.9 cm^{-1}, and on h-BN substrates it is 25.2 ± 0.4 cm^{-1}. There is no 2D FWHM disagreement between the bilayer graphene samples on h-BN and SiO_2. This would indicate h-BN and SiO_2 induce the same strain uniformity, or even greater uniformity in the monolayer case and that these samples either do not exhibit the predicted lattice matching from section 3.3, or that the Moiré patterning is not discernible with the imaging resolution used. This runs counter to the prediction of lattice mismatching causing strain variations. It is possible that these graphene on h-BN samples are not in proper contact with each other. There are visible contaminants in the graphene-h-BN stacked region in figure 5-38 (a) and (b), which may be preventing the formation of lattice-matching strains.

The TEC of the h-BN substrate was assumed to follow that of the underlying silicon instead of being independent. This was confirmed when comparing the two cases by calculating the resultant graphene TECs.[105] The case where the h-BN has an independent TEC to the substrate is shown in figure 5-41: the calculated graphene TEC resulted in a negative TEC up to three times larger than predicted by the theory. There is no difference between h-BN and Si/SiO_2 that can explain this increase in negative TEC. It is also opposite to the predictions of section 3.3 regarding the effect of flat substrates on graphene phonons. The h-BN being subject to the silicon TEC was considered more likely as this gives a graphene TEC comparable to theory and previous results, shown in figure 5-42.

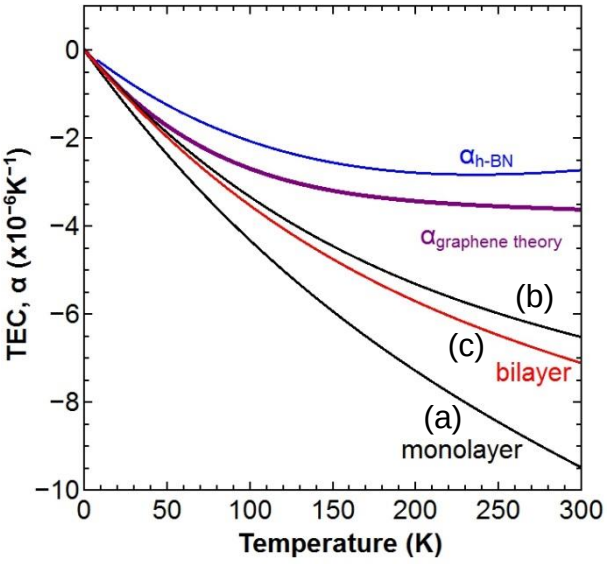

Figure 5-41: TEC dependence of h-BN substrate samples using an independent h-BN TEC (blue).[105] The monolayer and bilayer samples are labelled as in figure 4-39. The monolayer graphene TEC is show again in purple.[20]

Again, the individual sample variation is the greatest factor determining the TEC trend across these samples. Alternatively, sample (b) and (c) may be demonstrating the TEC quenching predicted of ultra-flat substrates in section 3.3. However, given that the range of TECs observed in SiO_2 substrates significantly overlaps the TEC range of the h-BN substrates, this conclusion cannot be made without further repeats of these sample types.

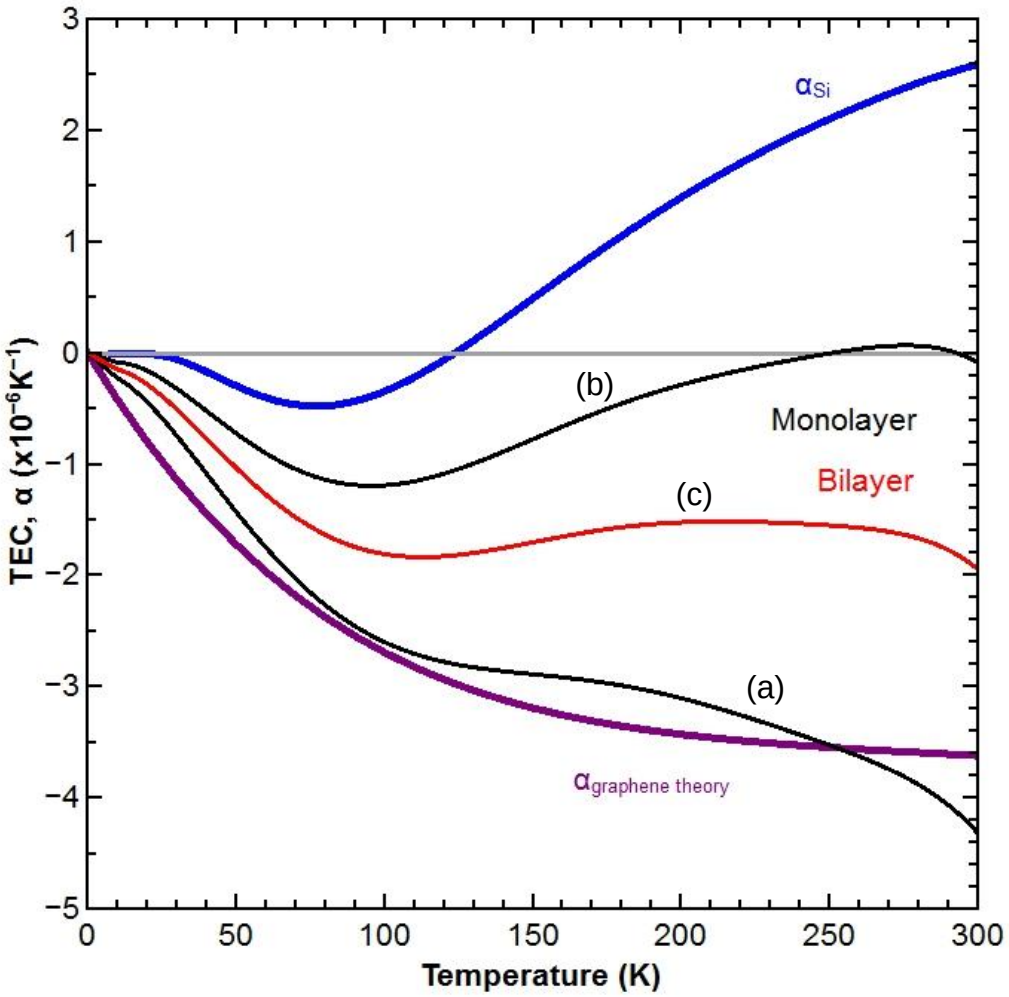

Figure 5-42: TEC dependence of all h-BN substrate samples, with the monolayer and bilayer samples labelled as previous. The TEC of silicon is in blue and the monolayer graphene TEC is show again in purple.[20,93]

5.7 Conclusion

The monolayer, bilayer and tri-layer graphene all exhibited Raman peak shift behaviour with temperature consistent with thermal strain after accounting for doping and temperature effects. The strain magnitudes were within the bounds predicted in section 3.1.3 for graphene with some imperfect surface contact or crumpling. As graphene samples exhibit strain behaviour consistent with both

strain reducing mechanisms, it was not conclusive which of these two phenomena caused the strain difference between the theory and experiment.

The TEC dependence with temperature was derived from the strain measurements, which covered the whole temperature range from room temperature to the 6 K minimum stable temperature (section 4.6.3). This was in excellent agreement with the predictions of Mounet *et al.* in comparison to other experimental measures. The first measures of bilayer and tri-layer graphene TECs were performed over the same temperature range. The multilayer TECs were shown to be similar to that of monolayer graphene to within the uncertainty of the study.

An attempt to optically measure the doping concentration dependence with temperature was made. The calculated values proved to vary considerably between both the samples and the methods of doping calculation.

Graphene samples with a h-BN substrate exhibited strain and TEC dependences similar to that of the SiO_2 substrate graphene, spanning a similar range of $\Delta\varepsilon$ and TEC dependences. The h-BN samples did exhibit a larger starting compressive strain than SiO_2. The reduced sample size prevented a definitive conclusion to be made to the comparative effects of SiO_2 and h-BN substrates. A larger sample size will allow an averaged TEC dependence to be determined that may lie outside of the range of graphene on SiO_2.

6 Conclusions

This Chapter covers a general summary of the findings in this thesis. This includes the main findings of thermal strain and TEC measurements on graphene of monolayer to tri-layer thicknesses and three different device designs. It then proceeds to describe the findings of the preliminary studies into doping concentration dependence and the effects of alternative substrate materials. This chapter concludes with a discussion of the potential future avenues by which progress in this study may be furthered.

6.1 Strain

The results of this study have shown that thermal strains consistently occur in mono, bi and tri-layered graphene on silicon substrates with SiO_2 surfaces. The strains in the samples were observed to move in a compressive direction as the temperature was reduced, to a maximum change of ~0.1 % across the whole temperature range. This change in strain was consistent with the prediction that the difference in thermal expansion between graphene and silicon would be the upper limit to the observed strain and TEC from chapter 3. The observed strains were biaxial in nature as no temperature-dependent peak broadening was observed, which would have indicated a uniaxial component to the strain. Additionally, temperature hysteresis was not observed between the cooling and warming measurement methods from section 5.1.1.

In contrast to the monolayer graphene results, a significant non-zero starting strain was observed in bi and tri-layered samples. This was considered to be

caused by a calibration offset in the correlation method rather than a physical effect, because of the lack of trend across all graphene thicknesses for room temperature starting strains. A measurement of the Raman peaks of bi and tri-layered graphene would need to be performed that completely controls for all external strain and doping contributions to provide a correct zero correlation position.

The effects of contacts on the induced thermal strains were investigated due to the evidence of slipping or crumpling of strained graphene observed in previous studies.[12,48] It was predicted that any such structures would increase the strain threshold for these relaxation effects in section 3.1.2. However, no evidence of sudden slipping was observed in any sample design style, demonstrating no difference between uncontacted graphene and contacted graphene. It was therefore concluded that the strains induced in this study did not reach the slipping or crumpling threshold in all cases. Therefore, both uncontacted and contacted graphene devices have the same strain mechanisms at temperatures below room temperature. In order to determine the efficacy of contact-pinning graphene, a greater temperature range would need to be investigated to induce a greater strain shift, such as from room temperature to temperatures greater than 500 K.

These results highlight the fact that graphene measurements at a different temperature from their manufacture will necessarily be strained compared to the initial temperature. A fully substrate-supported graphene flake will not produce a potential field according to equation (2.19), as $u_{ii} - u_{jj} = 0$ for biaxial strain. Increasing the strain to contacted graphene, suspended flakes, or semi-contacting substrate would be necessary to give rise to the non-zero electrical pseudo-potentials described in section 2.2.

6.2 Thermal expansion coefficient

The strain measurements performed in this study allowed an investigation into the thermal expansion coefficients (TECs) of monolayer to tri-layer graphene. A significant sample variance was observed in these measured TECs, which showed no correlation with contact design type. This suggested a range of adhesion between the graphene and SiO_2 caused during exfoliation, which gave the graphene some room to expand without strain. This was not surprising due to the amorphous nature of the SiO_2 surfaces.

The averaged TECs of the monolayer graphene samples were therefore used, which demonstrated a good agreement with the theoretical TEC predictions by Mounet *et al.*, and with the measurements of Singh *et al*.[16,20] The averaged result from monolayer graphene does have a lower magnitude of TEC than predicted by this theory. The TEC was measured at $(-3.2 \pm 0.2)\times10^{-6}$ K^{-1} at 300 K, compared to the theory of -3.6×10^{-6} K^{-1} at 300 K. This was expected from the predictions in section 3.1.1: that the theoretical expansion will be the maximum measureable value, and any imperfect surface contact effects only cause a reduced strain. Therefore an average across all samples will pull the TEC range to a lower magnitude than theoretically predicted.

Bi and tri-layer graphene demonstrated a comparable TEC range to that of monolayer graphene, $(-3.4 \pm 0.4)\times10^{-6}$ K^{-1} and $(-3.8 \pm 0.6)\times10^{-6}$ K^{-1} at 300 K respectively. The prediction, that the less negative Grüneisen parameter of bi and tri-layer graphene (section 3.2) would result in a TEC dependence with a lower magnitude than that of monolayer graphene, could not be verified due to the overlap in uncertainties between all three graphene thicknesses investigated.

This confirmatory measure of thicker graphene demonstrates the largely similar structural properties of mono, bi and tri-layer graphene.

6.3 Doping concentration

This study has highlighted the difficulties involved with determining doping concentrations in graphene from optical measurements. The analysis techniques used did not allow for a conclusive measure of doping concentrations in the graphene samples. This was attributed to individual sample variation and the calibration measurements used in section 2.3.4 causing large uncertainty ranges in the calculated values. While the doping concentrations calculated do fall within the expected range of doping values for graphene fabricated through mechanical exfoliation, these difficulties prevented a more detailed analysis.

A shift in doping concentration with temperature was observed in some devices, where a decrease in temperature caused a decrease in doping concentration. The devices that demonstrated this behaviour showed no correlation with fabrication design since every sample design style had both an example of this shift and no shift. In the samples that the doping shift was present it was statistically significant, changing by up to a factor of three across the temperature range investigated. If this shift in doping concentration with temperature is verified, these results would suggest that graphene devices may change doping concentration between measurement and use. A low-temperature measurement of the Fermi level of a graphene device may therefore be inappropriate if the device is then used at room temperature.

6.4 h-BN substrate

The preliminary investigation into the effects of using h-BN as a substrate for graphene devices found a similar graphene strain and TEC behaviour to that of graphene on SiO_2 substrates. This could indicate that the interface properties between graphene on h-BN on SiO_2 are not substantially different to that between graphene and SiO_2. Alternatively the range in strain and TEC dependences observed could instead be caused by contaminants introduced during the fabrication process and are independent of substrate surface. However, the number of h-BN samples investigated was not enough to conclusively prove any difference from SiO_2 substrates.

There may have been one example of graphene on h-BN, figure 5-42 (b), which demonstrates the presence of TEC quenching predicted in section 3.3. As mentioned previously, this cannot yet be determined as significant or an outlier, given the wide range of TEC dependences observed from the SiO_2 substrate samples in figures 5-17, 5-28, and 5-35. Measurements on further repeats of the h-BN substrate sample design are required to the same extent as on the SiO_2 substrate designs in order to make any reliable conclusions.

6.5 Future work

The next stage for the study of thermal strain in graphene devices is to increase the strain difference induced in the graphene samples. Increasing the temperature range of the experiment would allow for a greater integral range between the graphene and substrate TEC. An experimental apparatus that allows for an investigated temperature range above 600 K would allow for a greater

strain. Given graphene sample fabrication at room temperature resulted in starting strains around zero in monolayers, increasing the ΔT above ~300 K will cause a greater Δε than this study. This arrangement has the additional advantage for the induced strains as the TECs of graphene and SiO_2 have a greater difference in the temperature range above room temperature than below, which converges to zero at 0 K (figure 3-5). These increases in induced strain may allow for a greater investigation into the pinning effects of metal contacts by reaching the strain threshold for slipping or crumpling and create a difference in strain behaviour between uncontacted and contacted samples.

An alternative means of increasing strain would be to change the substrate material to one with a larger TEC difference to graphene than that of SiO_2. This TEC difference needs to be balanced against substrate hardness in order to successfully transfer the strain to the graphene deformation, and not a combined deformation of graphene and the substrate.

In order to induce strain configurations other than biaxial strain, different device designs and substrate geometries are required for the temperature range used in this study. Suspended graphene flakes could be used to construct a complex 2D strain field. By using the shrinking or expanding of suspended metal bars attached to a graphene flake, a strain distribution can be induced in order to induce a potential field, informed by equation (2.19) from chapter 2.

The intentional creation of pseudo-magnetism could therefore be possible through a correctly designed strain field.[41-43] This would open up the research possibilities of investigating electronic effects under high, variable pseudo-magnetic fields as large as 300 T using achievable strains without the cost of large magnetic fields.[42]

6.6 Conclusion

The total findings of this study on the effects of temperature variation on graphene devices and the implications of the findings were also speculated upon for future experiments involving these effects were summarised here. Starting with the strain and TEC findings from experiments involving mono, bi, and tri-layer graphene on SiO_2 substrates, which were found to be in good agreement with each other and monolayer graphene theory. This chapter then proceeded to summarise the findings of additional research avenues: the optical measurements of doping concentrations and a preliminary study into the effects of using h-BN as an alternative substrate surface. It was concluded with the further experiments that could be performed to further investigate the phenomena observed during this work.

Bibliography

[1] Wallace R., The Band Theory of Graphite, *Physical Review* **71**, 9, 622 (1947)

[2] Meyer J. *et al.*, The structure of suspended graphene sheets, *Nature* **446**, 60 (2007)

[3] Castro Neto A. *et al.*, The electronic properties of graphene, *Rev. Mod. Phys.* **81**, 1, 109 (2009)

[4] Mermin N., Crystalline order in two dimensions, *Phys. Rev.* **176**, 250 (1968)

[5] Novoselov K. *et al.*, Two-dimensional atomic crystals, *PNAS* **102**, 30, 10451 (2005)

[6] Abergel D. S. L. *et al.*, Properties of graphene: a theoretical perspective, *Advances in Physics* **59**, 4, 261 (2010)

[7] Beenakker C. and van Houten H., *In Semiconductor Heterostructures and Nanos-tructures*, Ehrenreich H. and Turnbull D. editors, volume 44 of *Solid State Physics*, 1 – 228, Academic Press (1991)

[8] Papageorgiou D. G. *et al.*, Mechanical properties of graphene and graphene-based nanocomposites, *Prog. Mater. Sci.* **90**, 75 (2017)

[9] Cao T. *et al.*, Valley-selective circular dichroism of monolayer molybdenum disulphide, *Nat. Commun.* **3**, 887 (2012)

[10] Rycerz A. *et al.*, Valley filter and valley valve in graphene, *Nat. Phys.* **3**, 172 (2007)

[11] Xiao D. *et al.*, Valley-Contrasting Physics in Graphene: Magnetic Moment and Topological Transport, *Phys. Rev. Lett.* **99**, 236809 (2007)

[12] Tsoukleri G. *et al.*, Subjecting a Graphene Monolayer to Tension and Compression, *Small* **5**, 21, 2397 (2009)

[13] Mohiuddin T. M. G. *et al.*, Uniaxial strain in graphene by Raman spectroscopy: G peak splitting, Grüneisen parameters, and sample orientation, *Phys. Rev. B* **79**, 205433 (2009)

[14] Frank O. *et al.*, Compression Behaviour of Single-Layer Graphenes, *ACS Nano* **4**, 6, 3131 (2010)

[15] Androulidakis C. *et al.*, Graphene flakes under controlled biaxial deformation, *Sci. Rep.* **5**, 18219 (2015)

[16] Singh V. *et al.*, Probing thermal expansion of graphene and modal dispersion at low-temperature using graphene nanoelectromechanical systems resonators, *Nanotechnology* **21**, 165204 (2010)

[17] Linas S. *et al.*, Interplay between Raman shift and thermal expansion in graphene: Temperature-dependent measurements and analysis of substrate corrections, *Phys Rev B* **91**, 075426 (2015)

[18] Storch I. R. *et al.*, Young's modulus and thermal expansion of tensioned graphene membranes, *Phys. Rev. B* **98**, 085408 (2018)

[19] Bao W. *et al.*, Controlled ripple texturing of suspended graphene and ultrathin graphite membranes, *Nat. Nanotechnol.* **4**, 562 (2009)

[20] Mounet N. and Marzari N., First-principles determination of the structural, vibrational and thermodynamic properties of diamond, graphite and derivatives, *Phys. Rev. B* **71**, 205214 (2005)

[21] Zakharchenko K. V. *et al.*, Finite Temperature Lattice Properties of Graphene beyond the Quasiharmonic Approximation, *PRL* **102**, 046808 (2009)

[22] Pozzo M. *at al.*, Thermal Expansion of Supported and Freestanding Graphene: Lattice Constant versus Interatomic Distance, *PRL* **106**, 135501 (2011)

[23] Herrero C. P. and Ramírez R., Thermal properties of graphene under tensile stress, *Phys. Rev. B* **97**, 195433 (2018)

[24] Moradi Z. *et al.*, Temperature-dependent thermal expansion of graphene, *Physical A* **512**, 981 (2018)

[25] Geim A., Graphene: Status and Prospects, *Science* **324**, 1530 (2009)

[26] Geim A. and Novoselov K., The rise of graphene, *Nat. Mater.* **6**, 183 (2007)

[27] Peierls R., Quelques properties typiques des corpses solides., *Ann. I. H. Poincare* **5**, 177 (1935)

[28] Landau L., Zur Theorie der phasenumwandlungen II, *Phys. Z. Sowjetunion* **11**, 26 (1937)

[29] Bowick M. and Travesset A., Statistical Mechanics of Membranes and Surfaces, *World Scientific*, Singapore (2004)

[30] Venables J. *et al.*, Nucleation and growth of thin films, *Rep. Prog. Phys.* **47**, 399 (1984)

[31] Novoselov K., Electric Field Effect in Atomically Thin Carbon Films, *Science* **306**, 666 (2004)

[32] Hernandez Y. *et al.*, High-yield production of graphene by liquid-phase exfoliation of graphite, *Nat. Nanotechnol.* **3**, 563 (2008)

[33] Bonaccorso F. *et al.*, Production and processing of graphene and 2d crystals, *Materials Today* **15**, 12, 564 (2012)

[34] Delhaes P., *Graphite and Precursors*, World of Carbon, CRC Press (2000)

[35] Lee C. *et al.*, Measurement of the Elastic Properties and Intrinsic Strength of Monolayer Graphene, *Science* **321**, 385 (2008)

[36] Memarian F. *et al.,* Graphene Young's modulus: Molecular mechanics and DFT treatments, *Superlattices and Microstructures* **85**, 348 (2015)

[37] Peres N. M. R., The transport properties of graphene, J. Phys.: Condens. Matter. **21**, 323201 (2009)

[38] Katsnelson M. I. *et al.*, Chiral tunnelling and the Klein paradox in graphene, *Nat. Phys.* **2**, 620 (2006)

[39] Bala Kumar S. and Guo J., Chiral tunnelling in trilayer graphene, *Appl. Phys. Lett.* **100**, 163102 (2012)

[40] Landau L. D., Lifshitz E. M., (1986) *Theory of Elasticity*, 3rd ed., Butterworth-Heinemann, Oxford.

[41] Guinea F. *et al.*, Energy gaps and zero-field quantum Hall effect in graphene by strain engineering, *Nat. Phys.* **6**, 30 (2010)

[42] Levy N. *et al.*, Strain-Induced Pseudo-Magnetic Fields Greater Than 300 Tesla in Graphene Nanobubbles, *Science* **329**, 544 (2010)

[43] Yan H. *et al.*, Observation of Landau-level-like quantization at 77 K along a strained-induced graphene ridge, *Phys. Rev. B* **85**, 035422 (2012)

[44] Zabel J. *et al.*, Raman Spectroscopy of Graphene and Bilayer under Biaxial Strain: Bubbles and Balloons, *Nano Lett.* **12**, 617 (2012)

[45] Metten D. *et al.*, All-Optical Blisster Test of Suspended Graphene Using Micro-Raman Spectroscopy, *Phys. Rev. Appl.* **2**, 054008 (2014)

[46] Chen C. *et al.*, Raman spectroscopy of substrate-induced compression and substrate doping in thermally cycled graphene, *Phys. Rev. B* **85**, 035431 (2012)

[47] Verhagen T. G. A *et al.*, Temperature-induced strain and doping in monolayer and bilayer isotopically labelled graphene, *Phys. Rev. B* **92**, 125437 (2015)

[48] Yoon D. *et al.*, Negative Thermal Expansion Coefficient of Graphene Measured by Raman Spectroscopy, *Nano Lett.* **11**, 3227 (2011)

[49] Downs C. (2015) *A route to strain-engineering in electron transport in graphene*, PhD Thesis, University of Exeter

[50] De Sanctis A. *et al.*, Strain-Engineering of Twist-Angle in Graphene/hBN Superlattice Devices, *Nano Lett.* **18**, 7919 (2018)

[51] Sun Y. *et al.*, Probing Local Strain at MX_2–Metal Boundaries with Surface Plasmon-Enhanced Raman Scattering, *Nano Lett.* **14**, 5329 (2014)

[52] Shioya H. *et al.*, Straining Graphene Using Thin Film Shrinkage Methods, *Nano Lett.* **14**, 3, 1158 (2014)

[53] Choi S. *et al.*, Effects of strain on electronic properties of graphene, *Phys. Rev. B* **81**, 081407 (2010)

[54] Chen C *et al.*, Raman Spectroscopy of Ripple Formation in Suspended Graphene, *Nano Lett.* **9**, 12, 4172 (2009)

[55] Calizo I. *et al.*, Temperature Dependence of the Raman Spectra of Graphene and Graphene Multilayers, *Nano Lett.* **7**, 9, 2645 (2007)

[56] Gardiner D. J.*, Practical Raman spectroscopy*, Springer-Verlag (1989)

[57] Venezuela P. *et al.*, Theory of double-resonant Raman spectra in graphene: intensity and line shape of defect-induced and two-phonon bands, *Phys. Rev. B* **84**, 035433 (2011)

[58] Mafra D. L. *et al.*, Determination of LA and TO phonon dispersion relations of graphene near the Dirac point by double resonance Raman scattering, *Phys. Rev. B* **76**, 233407 (2007)

[59] Malard L. M. *et al.*, Probing the electronic structure of bilayer graphene by Raman scattering, *Phys. Rev. B* **76**, 201401(R) (2007)

[60] Zhao H. *et al.*, Growth and Raman Spectra of Single-Crystal Trilayer Graphene with Different Stacking Orientations, *ACS Nano* **8**, 10, 10766 (2014)

[61] Ferrari A. C., Raman spectroscopy of graphene and graphite: Disorder, electron-phonon coupling, doping and nonadiabatic effects, *Solid Stat Commun.* **143**, 47 (2007)

[62] May P. *et al.*, Signature of the two-dimensional phonon dispersion in graphene probed by double-resonant Raman scattering, *PRB* **87**, 075402 (2013)

[63] Malard L. M. *et al.*, Raman spectroscopy in graphene, *Physics Reports*, **473**, 51 (2009)

[64] Ni Z *et al.*, Raman Spectroscopy and Imaging of Graphene, *Nano Res.*, **1**, 273-291 (2008)

[65] Frank O. *et al.*, Raman 2D-Band Splitting in Graphene: Theory and Experiment, *ACS Nano* **5**, 3, 2231 (2011)

[66] Yoon D. *et al.*, Strain-Dependent Splitting of the Double-Resonance Scattering Band in Graphene, *PRL* **106**, 155502 (2011)

[67] Huang M. Y. *et al.*, Phonon Softening and Crystallographic Orientation of Strained Graphene Studied by Raman Spectroscopy, *Proc. Natl. Acad. Sci. U.S.A.* **106**, 7304 (2009)

[68] Pisana S. *et al.*, Breakdown of the adiabatic Born-Oppenheimer approximation in graphene, *Nat. Mater.* **6**, 198 (2007)

[69] Lazzeri M. and Mauri F, Nonadiabatic Kohn Anomaly in a Doped Graphene Monolayer, *PRL* **97**, 266407 (2006)

[70] Das A. *et al.*, Monitoring dopants by Raman scattering in an electrochemically top-gated graphene transistor, *Nat. Nanotechnol.* **3,** 210 (2008)

[71] Bonini N *et al.*, Phonon anharmonicities in Graphite and Graphene, *Phys. Rev. Lett.* **99**, 176802 (2007)

[72] Froehlicher G. and Berciaud S., Raman spectroscopy of electrochemically gated graphene transistors: Geometrical capacitance, electron-phonon, electron-electron, and electron-defect scattering, *Phys. Rev. B.* **91**, 205413 (2015)

[73] Yan J. *et al.*, Electric Field Effect Tuning of Electron-Phonon Coupling in Graphene, *PRL* **98**, 166802 (2007)

[74] Heisenberg W., Über den anschaulichen Inhalt der quantentheoretischen Kinematik und Mechanik, *Zeitschrift für Physik **43***, 3–4, 172 (1927)

[75] Basko D. M., Electron-electron interactions and doping dependence of the two-phonon Raman intensity in graphene, *Phys. Rev. B* **80**, 165413 (2009)

[76] Apostolov A. T. *et al.*, Temperature and layer number dependence of the G and 2D phonon energy and damping in graphene, *J. Phys.: Condens. Matter* **24**, 235401 (2012)

[77] Mueller N. S. *et al.*, Evaluating arbitrary strain configurations and doping in graphene with Raman spectroscopy, *2D Mater.* **5**, 015016 (2018)

[78] Lee J. E. *et al.*, Optical separation of mechanical strain from charge doping in graphene, *Nat. Commun.* **3**, 1024 (2012)

[79] Metten D. *et al.*, Probing built-in strain in freestanding graphene monolayers by Raman spectroscopy, *Phys. Status Solidi B* **250**, 12, 2681 (2013)

[80] Metten D. *et al.*, Doping- and interference-free measurement of I_{2D}/I_G in suspended monolayer graphene blisters, *Phys. Status Solidi B* **252**, 11, 2390 (2015)

[81] Solozhenko V. L. and Peun T., Compression and thermal expansion of hexagonal graphite-like boron nitride up to 7 GPa and 1800 K, *J. Phys. Chem Solids* **58**, 9, 1321 (1997)

[82] Riberio R. M. and Peres N. M. R., Stability of boron nitride bilayers: Ground-state energies, interlayer distances, and tight-binding description, *Phys Rev B.* **83**, 235312 (2011)

[83] Dean C. R. *et al.*, Boron nitride substrates for high-quality graphene electronics, *Nat. Nanotechnol.* **5**, 722 (2010)

[84] Nekrashevich S. S. and Gritsenko V. A., Electronic Structure of Silicon Dioxide (A Review), *Phys. Solid State* **56**, 2, 207 (2014)

[85] Binning G. *et al.*, Atomic Force Microscope; *PRL* **56**, 9, 930 (1986)

[86] Zhong Q. *et al.*, Fractured polymer/silica fiber surface studied by tapping mode atomic force microscopy, *Surf. Sci. Lett.* **290**, L688 (1993)

[87] Goldstein J. I. *et al.* (1981) *Scanning Electron Microscopy and X-Ray Microanalysis*, New York, NY: Plenum Press

[88] De Broglie L., Recherches sur la théorie des quanta, *Ann. Phys.* **3**, 22 (1925)

[89] Ishigami M. *et al.*, Atomic Structure of Graphene on SiO_2, *Nano Lett.* **7**, 6, 1643 (2007)

[90] Geringer V. *et al.*, Intrinsic and extrinsic corrugation of monolayer graphene deposited on SiO_2, *PRL*, **102**, 076102 (2009)

[91] Harris J. W. and Stocker H., (1998) *Handbook of Mathematics and Computational Science*, New York: Springer-Verlag, 92-93

[92] Ohmi Y., Effect of uniaxial strain on the electronic transport in single layer graphene, *International Meeting for Future of Electron Devices,* Osaka, 126 (2011)

[93] Middelmann T. *et al.*, Thermal expansion coefficient of single-crystal silicon from 7 K to 293 K, *PRB*, **92**, 174113 (2015)

[94] de Andres P. L. *et al.*, Bending modes, anharmonic effects, and thermal expansion coefficient in single-layer and multilayer graphene, *Phys. Rev. B* **86**, 144103 (2012)

[95] Das A. *et al.*, Phonon renormalization in doped bilayer graphene, *Phys. Rev. B* **79**, 155417 (2009)

[96] Woods C. R. *et al.*, Commensurate-incommensurate transition in graphene on hexagonal boron nitride, *Nat. Phys.* **10**, 451 (2014)

[97] Demtröder W. (1971) *Laser Spectroscopy Basic Concepts and Instrumentation*, Vol. 1, Springer, Berlin, Heidelberg

[98] Glassbrenner C. J. and Slack G. A., Thermal Conductivity of Silicon and Germanium from 3°K to the Melting Point, *Phys. Rev.* **134**, A1058 (1964)

[99] Ferrari A. C. *et al.*, Raman spectrum of graphene and graphene layers, *PRL*, **97**, 187401 (2006)

[100] Zhenhua N. *et al.*, Raman spectroscopy and imaging of graphene, *Nano Res.*, **1**, 273 (2008)

[101] Ferrari A. C., Basko D. M., Raman spectroscopy as a versatile tool for studying the properties of graphene, *Nat. Nanotechnol.*, **8**, 235 (2013)

[63] Malard L. M. *et al.*, Raman spectroscopy in graphene, *Physics Reports*, **473**, 51 (2009)

[102] Calizo I. *et al.*, Variable temperature Raman microscopy as a nanometrology tool for graphene layers and graphene-based devices, *Appl. Phys. Lett.*, **91**, 071913 (2007)

[103] Huang C. *et al.*, Probing 2D sub-bands of bi-layer graphene, *RSC Adv.*, **4**, 51067 (2014)

[104] Neumann C. *et al.*, Raman spectroscopy as a probe of nanometre-scale strain variations in graphene, *Nat. Commun.* **6**, 8429 (2015)

[105] Yates B. *et al.*, The anisotropic thermal expansion of boron nitride, *Philos. Mag.* **32**, 4, 847 (1975)